UNIVERSIDADE DE SÃO PAULO
INSTITUTO DE ASTRONOMIA, GEOFÍSICA E CIÊNCIAS
ATMOSFÉRICAS

JORGE ROSAS SANTANA

Clouds and their effects on solar radiation at São Paulo
(*Nuvens e seus efeitos na radiação solar em São Paulo*)

São Paulo
2018

JORGE ROSAS SANTANA

Clouds and their effects on solar radiation at São Paulo
(*Nuvens e seus efeitos na radiação solar em São Paulo*)

Dissertação apresentada ao Instituto de Astronomia, Geofísica e Ciências Atmosféricas da Universidade de São Paulo para obtenção do título de Mestre em Ciências.

Área de concentração: Meteorologia
Orientador: Prof. Dra. Marcia Akemi Yamasoe

Aos meus pais

Agradecimentos

Queria agradecer primeiramente aos meus pais por me incentivar e motivar no mundo da meteorologia. Ao sistema de educação de Cuba (público e para todos) por contribuir com minha formação como meteorologista.

Agradecimento especial à minha estimada orientadora Dra Marcia Akemi Yamasoe, por todo apoio e profissionalismo durante a pesquisa, em ensinar novos conhecimentos que enriqueceram esta pesquisa e minha formação.

A CAPES pela concessão da bolsa de mestrado.

Aos doutores Eduardo Landulfo, Fabio Lopes por fornecer os dados do Lidar e sky câmera.

Ao Dr. Bernard Mayer por fornecer o código LibRadtran. À AERONET, centro de processamento de CLOUDSAT e EarthCARE Research Product Monitor de JAXA pelos dados de aerossóis e de propriedade de nuvens de satélite usados.

Aos doutores Edmilson Freitas e Elisa Sena por contribuírem positivamente ao trabalho no exame de qualificação.

Ao Dr. Boris Barja Gonzalez, meu primeiro orientador, por todo seu apoio, desde o começo, no mundo da pesquisa. Ao Dr Michel Mesquita por me ajudar com minha permanência no Brasil.

Ao Eduardo Fernandes por ajudar com a manutenção dos equipamentos de medição de radiação solar utilizados nesta pesquisa. Aos observadores meteorológicos da estação meteorológica do IAG, pela sua excelente contribuição com as observações de nuvens por quase seis décadas.

Aos trabalhadores da seção de informática do DCA do IAG.

Aos professores Dr. Rene Estevan Arredondo e Dr. Juan Carlos Antuña com minha formação na área de transferência radiativa.

A minha querida Camila, por sempre estar do meu lado, nos bons e maus momentos, me trazer felicidade e motivação para seguir em frente, independente dos problemas que poderiam surgir.

Aos meus queridos amigos Luis, Talita, Veronika, Sameh, Isaque Luan, João Basso, João Hackerott, Paola, Alberto Bié, Andrea e Miriam por compartilharem estes maravilhosos dois anos de mestrado. Aos meus

companheiros cubanos, Darsys & Raidiel, Janet & Jose, Yusvelis, Maciel, Damian & Jenifer e Dayana por me apoiarem no começo do mestrado.

Resumo

Rosas J. *Nuvens e seus efeitos na radiação solar em São Paulo, 2018. Dissertação (Mestrado). Instituto de Astronomia, Geofísica e Ciências Atmosféricas, Universidade de São Paulo, São Paulo, 2018.*

Na Região Metropolitana de São Paulo, foram estudadas as nuvens e seus efeitos na radiação solar. Para tanto, foram usadas observações visuais de nuvens, medições desde a superfície efetuadas por diferentes radiômetros, produtos dos satélites de órbita polar CALIPSO e CloudSat e o modelo de transferência radiativa 1-D *LibRadtran*.

Foi desenvolvida uma climatologia para o ciclo diurno da fração de cobertura de nuvens (1958-2016) usando dados de observações visuais. O ciclo diurno da cobertura de nuvens foi dominado por nuvens baixas, especialmente as estratiformes. Observaram-se diferenças entre o ciclo diurno das nuvens baixas cumuliformes e estratiformes. Além disso, houve uma tendência de aumento da fração de cobertura de nuvens baixas (1,6 %/década), especificamente das estratiformes (3,1 %/década), e das nuvens cirriformes (0,8%/década). Por outro lado, observou-se tendência de diminuição da fração de cobertura de nuvens médias (-2,4%/década).

A variabilidade sazonal e diurna do perfil vertical de nuvens foi analisada, com as nuvens atingindo maiores altitudes à noite e no verão. No inverno, as nuvens baixas predominaram.

A profundidade óptica efetiva da nuvem (ECOD), usando a transmitância total em 415 *nm,* e os efeitos instantâneos das nuvens sobre a radiação solar, de medições de irradiância solar global, foram estimados em sinergia com cálculos feitos com o LibRadtran. ECOD apresentou variabilidade diurna e sazonal com máximo na primavera (34,4) e no período da tarde (34,2) e mínimo pela manhã, próximo ao nascer do sol (25,5) e no inverno (26,9) para nuvens baixas. O efeito radiativo de onda curta apresentou dependência com relação à obstrução do disco solar pelas nuvens, o tipo de nuvem e fração de cobertura. A atenuação máxima foi observada para nuvens baixas com o céu totalmente nublado, com valor médio de redução de 72 % da irradiância global, comparada com condições de céu claro. Medianas de redução de nuvens médias e altas foram de 57 % e 33 %, respectivamente. Foram observados

efeitos de incrementos da radiação solar (***enhancement***) *de* cerca de 10 % com duração de até 20 minutos, devido ao espalhamento pelas laterais das nuvens, em presença de todos os tipos de nuvens analisados, quando o disco solar não estava obstruído. O máximo de ***enhancement*** chegou até 50 % na presença de nuvens baixas.

Palavras-chave: Nuvens, COD, MFRSR, CALIPSO-CloudSat, LibRadtran.

Abstract

Rosas J. Clouds and their effects on solar radiation in São Paulo, *2018. Dissertation (Master)-Instituto de Astronomia, Geofísica e Ciências Atmosféricas, Universidade de São Paulo, São Paulo, 2018.*

Clouds and their instantaneous effects on downward solar radiation were studied at the Metropolitan Area of São Paulo. For this purpose, visual observations of clouds, ground-based measurements performed by different radiometers, products from the polar orbiting satellites CALIPSO and CloudSat and 1-D Radiative Transfer Model (RTM) LibRadtran were used.

Daytime climatology of cloud cover fraction (1958-2016) using data of hourly visual observations was carried out. The diurnal cycle of cloud cover fraction was dominated by low clouds especially by stratiform clouds. Remarkable differences in the diurnal cycles of low cumuliform and stratiform clouds were also observed. During the time period, positive trends for low cloud cover (1.6 %/decade), especially stratiform (3.1 %/decade), and cirriform cloud (0.8 %/decade) were observed, while a decreasing trend of mid-level cloud cover (-2.4%/decade) was found.

Seasonal and diurnal variability of vertical profile of cloud was observed, with cloud extending to higher altitudes at night and with maximum frequency of occurrence observed in summer. In winter, low clouds prevailed.

Effective cloud optical depth (ECOD), using the total transmittance at 415 nm, and instantaneous cloud effects on solar radiation at the surface, using global irradiance measurements, were estimated in synergy with *LibRadtran* computations. ECOD presented seasonal and diurnal variability, with maximum of mean in spring (34.4) and in the afternoon (34.2), and minimum at sunrise (25.5) and winter (26.9) for low clouds. The shortwave effects of clouds depended on solar disk condition, cloud type and cloud cover. Maximum of shortwave radiative attenuation was observed for low clouds in total overcast conditions with a median reduction of 72 % of global irradiance compared to clear sky. Median reduction of mid and high clouds was 57 % and 33 %, respectively. Enhancement effects with duration as long as 20 minutes, caused by lateral scattering, were observed in the presence of all analyzed cloud types,

when the solar disk was not blocked by clouds, increasing global solar irradiance around 10% at the surface. Maximum enhancement could reach 50 % for low clouds.

Figures Index

Tables Index

Acronyms and abbreviations

AERONET   AErosol RObotic NEtwork

AOD   Aerosol Optical Depth

CALIPSO   Cloud-Aerosol Lidar and Infrared Pathfinder Satellite Observations

CB   Cloud base height

CEF   Shortwave Cloud Efficiency

CloudSat   Cloud Satellite

COD   Cloud Optical Depth

CRE   Shortwave Cloud Radiative Effect

CSZA   Cosine of solar zenith angle

D   Diffuse Irradiance

ECOD   Effective cloud optical depth

g   Asymmetry Parameter

G   Global Irradiance

IWC   Ice Water Content

LWC   Liquid Water Content

MASP   Metropolitan Area of São Paulo

MFRSR   Multifilter Rotating Shadowband Radiometer

NCRE   Shortwave Normalized Cloud Radiative Effect

NIR   Near Infrared

r_e   Effective radius

R   Hemispherical Reflectance

RTE	Radiative Transfer Equation
S	Direct Sun Radiance
SS	Direct Sun Irradiance
SS$_0$	Direct Sun Irradiance at Top of the Atmosphere
SSA	Single Scattering Albedo
SZA	Solar zenith angle
T	Total hemispheric transmittance
T$_{dir}$	Transmittance of direct beam radiation
TOA	Top of the Atmosphere
VIS	Visible
WMO	World Meteorological Organization

Contents

1. Introduction

Clouds are the main component of the radiative transfer at the atmosphere. They absorb and emit terrestrial radiation, warming the earth surface and the atmospheric layers underneath (positive effect) and cooling the atmospheric layers aloft. These processes also contribute to the formation and development of clouds (Heymsfield et al., 2017; Wood, 2012).

In the shortwave spectrum, clouds have an elevated albedo, producing a cooling radiative effect (negative effect) on beneath layers and the surface. The magnitude and signal of the radiative effect depends on the properties of the clouds. The main shortwave effect of low clouds at surface is cooling, but there are cases with short durations, when they do not block the solar disk, that warming effects or enhancement of solar radiation at the surface can occur (Mateos et al., 2013; Tzoumanikas et al., 2016). Cirrus clouds play a different role compared to other clouds, they warm the atmosphere more effectively, because they are optically thin and located at higher altitudes (Stephens, 2005).

Clouds are also important to the hydrological cycle of the earth, bringing water to the surface by precipitation and transporting water vapor to higher layers of the troposphere. The condensation process releases a large amount of latent heat, contributing to the transport of energy in the atmosphere (Boucher et al., 2013). All these processes related to clouds affect large-scale circulations and wave disturbances. Hence, cloud systems are important issues for the climate and weather prediction numerical models.

Clouds can respond to the global warming due to the increase of CO_2 concentration, a process known as cloud feedback. Therefore they can contribute to mitigate or reinforce the warming effect (Lee, 2016). Theoretically, the global warming can strengthen due to cloud positive feedback: increasing the tops of high clouds by expansion of the troposphere and the expansion of the Hadley cell, producing the migration of storm tracks poleward. The latter can increase low clouds near poles, where solar radiation at the surface is reduced, decreasing the shortwave radiative effect (Boucher et al., 2013). Cloud cover fraction of low, mid and high clouds is expected to decrease specially in subtropical areas, but that is still unclear (Boucher et al., 2013).

Owing to cloud positive feedback, global observations and simulations indicate that cloud properties such as cloud amount are changing over the time. Eastman and Warren, (2013) reported the decrease of mid and high level clouds in mid latitudes with a global decrease of cloud amount of about 0.4 % per decade. Recently, Norris et al. (2016) showed agreement between satellite records and climate simulations of the reduction of cloud cover globally. They observed an increase of the height of higher clouds in all latitudes and the expansion of the subtropical dry zones as a consequence of the increase of greenhouse gas concentration and a recovery from the volcanic eruptions.

From the above mentioned reasons, understanding the role of clouds in the climate system is needed. Studies focused on the possible changes of the diurnal cycle and regional cloud amount are also crucial (Eastman and Warren, 2014). Global circulation models have large bias in cloud frequency occurrence of cloud types and their respective diurnal cycles. In addition, there is a need of measurements of cloud properties and studies of their radiative impacts in climate-sensitive areas (Burleyson et al., 2015).

Nowadays, with the inclusion of active sensors as radar and lidar on satellites, these techniques become strong tools for studying the vertical profiles of clouds. This is important to understand the impact of clouds on the radiation budget of the earth (Joiner et al., 2010) and the impact of the vertical distribution of latent heat released by them on the global circulation and precipitation. The A-train constellation formed by Cloud Satellite (CloudSat) and Cloud-Aerosol Lidar and Infrared Pathfinder Satellite Observations (CALIPSO), among other satellites, have contributed to the improving of retrieving cloud properties and their associated radiative forcing. In addition, the observations of clouds from the surface still represent a useful dataset with some advantages over satellite records. First, a long period of records, duration and temporal resolution allows for a better study of trends and diurnal cycles (Eastman and Warren, 2014). Besides, according to the authors, ground based observations are still the best detector of low clouds.

Studying the clouds over urban and industrialized areas is a focus of high interest, because changes of their properties can be induced by the increase of

aerosol concentrations, as a consequence of air pollution and by aircraft emissions. Furthermore, cloud properties can change due to the modification of land use, which, in turn, can alter the hydrological cycle. Cloud albedo can increase and cloud can last longer in the atmosphere, contributing to the higher shortwave cooling effect. However, cloud cover can be reduced, by the increase of aerosols with high absorption efficiency of solar radiation, reducing the shortwave cooling effect. There are contrasting results about how aerosols affect the evolving clouds (Boucher et al., 2013), therefore it is still a topic where many studies are needed.

An important example of region with higher urbanization and widely extended area is the megacity of São Paulo, considered as the top ten of larger cities around the world. It is an important source of aerosols generated by emission of cars and also influenced by long range transport of biomass burning plumes in spring (de Almeida Castanho et al., 2008). The precipitation regime is changing, with extreme events being more frequent. Especially since the end of the 1950s, a significant increase of rainy days and total daily rainfall have been observed (Obregón et al., 2014; Silva Dias et al., 2013). Silva Dias et al. (2013) also mentioned that the intensification of the urban heat island and cloud microphysics modification due to pollution are factors to take into account for explaining the positive trend observed in the wet season in the last eighty years. The study of clouds in the region is an issue to be addressed due to the possible influence of urbanization on their properties (Yamasoe et al., 2017).

At São Paulo, few works related to clouds and their impacts on solar radiation have been carried out. They are focused on the specific topics:

Moura et al. (2016) studied total cloud cover variability at São Paulo from visual observations during 1961-2013. The work is limited to the mean total cloud cover in terms of the diurnal and annual cycles. They compared mean diurnal and annual cloud cover from visual observations with cloud parameters retrieved from satellite and found good agreement.

Landulfo et al. (2009) showed the ability to obtain optical properties of thick cirrus clouds in the region from ground-based LIDAR at 532 nm and 355 nm. They discussed the frequency of occurrence of cirrus as computed for valid

days of measurements when low clouds did not affect the LIDAR beam. Due to the restricted field of view of the system, the measurements lead to unrealistic results of frequency of cirrus clouds, for instance, maxima observed in winter.

Recently, Yamasoe et al. (2017) studied the climatological radiative effect of low, multilayer and high level clouds based on 24 h mean of downward solar irradiation data at the surface. They analyzed the seasonal cycle of cloud cover and how the solar radiative effect changed with the sky fraction covered with clouds with distinct base height. Considerable differences in cloud effects between January and July were observed, due to the high dependence on the cosine of the solar zenith angle (CSZA). The work is limited, since the authors based their analysis on the cloud fraction only, without discrimination of cloud genera, and did not compute the instantaneous cloud radiative effect on solar radiation, which implies the knowledge of other cloud parameters, such as cloud optical depth. Thus, trying to complement previous studies on the effect of clouds on solar radiation at São Paulo region, the aims of this work are presented next.

1.1. Aims

This project aims the characterization of clouds in the Metropolitan area of Sao Paulo (MASP) and the estimation of their effects on solar radiation reaching the surface. The specific objectives are:

1. Understand how the physical and optical properties vary according to cloud types.
2. Analyze long term variability of cloud cover fraction.
3. Estimate the shortwave radiative effects of clouds using the radiative transfer library LibRadtran.

The objectives will be carried out with the next tasks:

- Analysis of clouds and their properties using products generated by the polar orbiting satellites CloudSat and CALIPSO.
- Retrieve optical properties of clouds from ground-based measurements of radiative fluxes.

- Long term clouds climatology using visual observations of cloud cover fraction, according to cloud genera and base height.
- Shortwave cloud radiative effects and efficiency computed from cloud properties obtained from ground-based measurements and the LibRadtran.

2. Review of literature

2.1. About clouds

2.1.1. Cloud types

The World Meteorological Organization (WMO) defines 10 types of clouds 'genera' according to the height level where they form and to their appearance, as presented in Table 1. These 10 genera make a total of 100 combinations of species and varieties, describing the shape, internal structure, transparency and arrangement of clouds (https://cloudatlas.wmo.int/). Prefixes and suffices from 'Latin' indicate the character of clouds - stratus: flat; cumulus: heap; cirrus: feathers, wispy; nimbus: rain; alto: mid-level.

Table 1: The 10 types of cloud genera as classified by WMO, according to the height level.

Level	Height	Acronym	Name
High	Above 6000 m	Ci	Cirrus
		Cc	Cirrostratus
		Cs	Cirrocumulus
Mid	2000-8000 m	As	Altostratus
		Ac	Altocumulus
		Ns	Nimbostratus
Low	Below 2000 m	Cu	Cumulus
		Sc	Stratocumulus
		St	Stratus
		Cb	Cumulonimbus

Stratocumulus (*Sc*), the combination of Latin *stratus* and *cumulus*, is a low cloud type as a result of grouping convective elements forming a layer. It is the most frequent cloud coverage around the world. Annually about 23 % of the sky over the ocean, with maximum of 60 % in the colder regions of sea anticyclone systems (Wood, 2012), are covered by Sc clouds. Over the land, the mean fraction of the sky covered by *Sc* is around 12 % (Warren et al., 2007). The seasonal cycles of *Sc* in the southern hemisphere are stronger than in the northern hemisphere and the month of maximum cloud cover is variable and depends on the region. Although the influence of the seasonality is unclear in the tropical regions, at the North Atlantic and Pacific Oceans, the maximum *Sc* cloud cover is observed in winter, in the western sides and, in summertime, in the eastern sides (Wood, 2012). The *Sc* has maximum coverage in the

morning with the higher amplitude in the eastern ocean (Eastman and Warren, 2014).

Cirrus clouds are the thinner clouds usually semitransparent to solar radiation unless the sun is near the horizon. Cirrus can be dense enough to produce shadows in the case of *cirrus spissatus*. Cirrus (Ci) and cirrostratus (Cs) are primarily composed by ice crystals. *Cirrocumulus* (Cc) is highly or totally composed of supercooled water droplets. They are inconsistent, grainy and very thin with thickness less than 200 m (Holton and Curry, 2003). *Cirrus* clouds (Ci, Cc, Cs) grouped into a single class is the most important cloud by spatial coverage over land with 22 %, while over the sea, the mean cloud cover is only 12 % (Warren et al., 2007). The higher frequency of cirrus clouds is observed in the tropics near the Inter-Tropical Convergence Zone (ITCZ) especially over the land with maximum of 70 % in the West Central Pacific (Heymsfield et al., 2017).

*Nimbostratu*s (*Ns*) are classified as mid-level clouds, but sometimes can be observed at low levels. They produce moderately steady precipitation often during hours. They cover only about 5 % around the globe in land and ocean and can be in companion of convective clouds as *cumulonimbus* (Cb). *Ns* is more frequent, with greater spatial coverage in mid-latitudes and polar regions (https://atmos.washington.edu/CloudMap). Values of mean cloud coverage can be as high as 24 % in polar regions.

The *altocumulus* clouds (Ac) look similar to *Sc*, but with base at mid-level altitude and predominantly composed by water and supercooled water droplets. Even though they produce gray shading, they are relative thin with maximum thickness up to 1 km (Holton and Curry, 2003). They are the most important mid-level clouds with a mean coverage of 17 % (Warren et al., 2007).

Altostratus clouds (*As*) are dominated by ice particles giving a diffuse and fibrous look. They are deeper than *Ac* with depth values higher than 2 km, with top usually compared to cirrus clouds. Despite the presence of *As* implies larger spatial coverage, they are less frequent than *Ac*, leading to global mean cloud cover of 5 % (Warren et al., 2007).

Cumulus (*Cu*) belongs to the convective clouds at the first stage. When convection is strong enough they can develop into *Cumulonimbus clouds* (*Cb*). Before becoming *Cb*, *Cu* can pass through a variety of steps from *cumulus fractus* up to *cumulus congestus*. Cu has less spatial coverage as compared to low *stratiform* clouds as stratus (*St*) and *Sc*. They have a global mean cloud cover in ocean (13 %) higher than over land (5 %) (Warren et al., 2007). Concerning the diurnal cycle, *Cu* presents maximum of spatial coverage near midday over the land, with the highest amplitude over land due to the lower thermal inertia as compared to the ocean (Eastman and Warren, 2014).

Cb is the less frequent cloud genus with mean cloud cover of 5 %, with few differences between ocean (6 %) and land (4 %) (Warren et al., 2007). Notable contrast is found between the diurnal cycles in ocean and land. Over land, the maximum is observed near sunset with higher amplitude, while over the ocean it is observed near sunrise (Eastman and Warren, 2014).

2.1.2. Cloud formation

Clouds can form when the air becomes supersaturated with respect to ice or water, i. e. the vapor pressure of the air parcel is higher than the saturated vapor pressure over the flat surface of the water or saturated vapor pressure over a flat surface of ice. The presence of aerosols, acting as cloud condensation nuclei (CCN) or ice nuclei (IN), contributes to break the energy generated by surface tension of the drop, decreasing the equilibrium vapor pressure over the droplet and favoring the formation and growth of cloud particles under low values of supersaturation. The level of supersaturation affects the size of particles activated, i.e. with the increase of supersaturation, more smaller particles are activated (Yau and Rogers, 1989). The supersaturation increases with the updrafts of clouds, therefore with higher updrafts more smaller drops are expected to be activated (Stith et al., 2002). Aerosol chemical composition and size also influence the activation of cloud droplets, the bigger, more hygroscopic, is the aerosol the lower supersaturation needed to activate cloud droplets (Yau and Rogers, 1989).

The air becomes supersaturated by means of two processes: the decrease of temperature under constant pressure or advection of humid air to

the region contributing to the increase of the water vapor concentration. Additionally, moist air can be forced to lifting and, in this ascension, the temperature decreases by adiabatic expansion, vapor pressure rises and air becomes saturated.

Ice nucleation, i.e., formation of ice by freezing, can be heterogeneous or homogenous. The homogenous nucleation is a spontaneous freezing of super cooled droplets or a pure solution of aerosol particles (Heymsfield et al., 2017). It occurs at temperature lower than -38 °C and higher supersaturation on ice (above 140 %). The heterogeneous nucleation is the most frequent mechanism of ice formation but still not well understood because it can occur under several conditions (Heymsfield et al., 2017). Basically, heterogeneous nucleation takes place when temperature is below 0 °C and the air saturated with respect to ice. It needs an IN immersed or in contact to super cooled water droplets or for deposition of water vapor onto it. The size of supercooled drops influences the temperature at which nucleation occurs, the larger the drops the higher the temperature for the ice nucleation (Yau and Rogers, 1989).

There is a variety of mechanisms in the atmosphere leading to the formation of different cloud types. Convection is the main driver of cloud formation. By this mechanism, the air is transported to the higher layers of the atmosphere. When convection is deeper, updrafts are strong enough to develop deep convective clouds. The own process of convective activity can lead to the formation of adjacent clouds such as *Ns*, *Sc*, and *Cu*, as well as mid and high level clouds (Houze, 2014).

Low stratiform clouds, mid and high clouds can develop convective instability driven by the longwave radiative cooling. The emission of longwave radiation by the cloud layer increases the cooling at cloud top, while absorption increases and the warming near the cloud base. These temperature differences enhance the convective circulation previously formed by buoyancy and wind, allowing the increase of cloud lifetime (Houze, 2014).

Low stratiform clouds of the boundary layer are coupled to the moist source at the surface. *Stratus* clouds can form when they separate from the fog layer at the surface that deepens due to mixing and radiative cooling at the top.

At sunrise, with solar radiation, the layers of clouds warm and hence tend to disappear (Houze, 2014). *Sc* also forms under stable conditions of the lower troposphere, when the layer of clouds is initially formed and the radiative cooling increases the inversion layer of temperature above cloud top. This process starts the convection that enhances as a result of the heating by condensation in updraft and cooling by evaporation in downdraft. When solar heating is present, the convection and layer of temperature inversion tend to disappear and hence the own cloud (Wood, 2012).

Ns are formed by motions of near stable air that deepens enough to form particles of rain or snowflakes. They are related to synoptic systems with organized storms as fronts, tropical cyclones and mesoscale convective systems (Houze, 2014).

Cirrus clouds form primarily in the upper troposphere where temperatures are lower than -30 °C, about 8 km. Below -38 °C there is no activation of liquid water drops, because water vapor can only be saturated or supersaturated with respect to ice. Then, cirrus can form by lifting of moist air or liquid or mixed phase clouds previously formed below. Mixed phase clouds are formed by strong updrafts (Heymsfield et al., 2017).

Lifting can occur on large scales, along a frontal boundary or by small scale vertical circulation developed around a core of jet stream. Cirrus can form under heterogeneous or homogenous nucleation and, depending on the mechanism, differences in ice sizes and concentrations are found (Heymsfield et al., 2017). Radiative cooling at cloud top and radiative warming near cloud base due to longwave emission and absorption, respectively, lead to the development of cloud top and turbulence that contributes to maintain and enhance the cirrus layer (Heymsfield et al., 2017).

Cirrus ice crystals have not simple idealized hexagonal shapes, instead a variety of geometries (*habit*) are found. For radiative purposes ice habits are classified as: solid column and hollow column, plate, dendrite, aggregate, bullet rosettes (Figure 1) (Key et al., 2002).
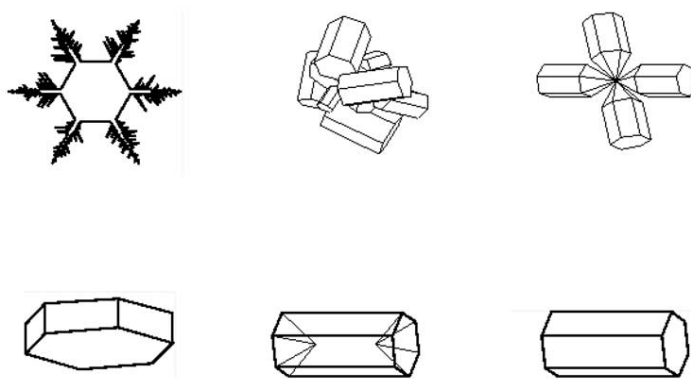
Figure 1: Examples of idealized shapes of the particle habits. Clockwise from top left: dendrite, aggregate, bullet rosette, solid column, hollow column, and plate (from Key et al., 2002).

An association between ice cloud habit with temperature and humidity has been previously reported. For stronger cloud updrafts , hexagonal and 3-D crystals are expected, whereas for weaker velocities the plates are common (Heymsfield et al., 2017). For temperature ranges between -20 °C and -40 °C with low supersaturation, plates are present. Below -40 °C there is an increase of columnar shapes. In the same range of temperature but with supersaturation above 25 % bullet rosettes, long columns containing poly-crystals are observed (Heymsfield et al., 2017). With cooler conditions above -60 °C, needle and columnar forms are frequent. Stith et al. (2002) suggested aggregates as the mean habit of ice particle in the upper regions of tropical convective clouds and the increase with altitude of particle sizes due to aggregation effects.

2.2. Aerosol effects on clouds

Tropospheric aerosols can affect the clouds by cloud-aerosol interactions known as Twomey effect (Twomey, 1977) and due to the rapid adjustments as a consequence of the aerosol direct radiative effect on the surface energy budget, the atmospheric thermodynamic profile and on the clouds (Boucher et al., 2013).

Due to the Twomey effect, the shortwave cloud radiative effects are more affected than longwave radiative effects (Alizadeh-Choobari and Gharaylou, 2017). With higher concentrations of aerosols, the number of condensation nuclei or ice nucleation particles can rise, reducing precipitation and increasing cloud cover and cloud lifetime (Albrecht, 1989). Global cloud albedo can

increase by means of the longer lifetime, higher top of clouds (Pincus and Baker, 1994), and by smaller cloud droplets. Under a constant water content, the increase of aerosol concentration can produce the decrease of cloud droplets size and hence the increase of cloud albedo (Boucher et al., 2013). This increase is more significant for low concentration of droplets (Andrejczuk et al., 2014; Pincus and Baker, 1994). However, in some cases, with higher number of larger aerosols (about 0.5 µm) the albedo can decrease (Andrejczuk et al., 2014). Higher concentrations of aerosols increase the liquid water content and the optical depth of cloud due to more condensation (Alizadeh-Choobari and Gharaylou, 2017). High correlation between decreasing of precipitation and load of aerosol dust has been reported around the world (Hui et al., 2008). Alizadeh-Choobari and Gharaylou, (2017) reported lower cloud base under pollution conditions due to the drier boundary layer as compared to clean boundary layer.

Theoretically, absorption of solar radiation by aerosols induces a diabatic heating and hence an increase of temperature, reducing the relative humidity and delaying the saturation of the layer. The static stability of clouds can be affected and the evaporation of cloud droplets occurs due to the heating, decreasing cloud cover. This decrease allows for an extra warming of the surface by solar radiation (Perlwitz and Miller, 2010). However it is not a simple dynamic process, because when the layer is heating by absorption of radiation by aerosols, the specific humidity increases. Thus the warmer layer produces a moisture convergence. That can overcome the possible reduction of cloud cover, increasing the cover of low clouds especially in summertime and over land (Perlwitz and Miller, 2010). Those processes depend on a variety of factors as atmospheric circulation and the influence of absorbing aerosols in the specific humidity (Perlwitz and Miller, 2010).

2.3. Sao Paulo weather

Due to the geographical and topographic conditions, the weather in São Paulo is strongly influenced by the synoptic systems and the local circulation of breeze. In the austral summer, December to February, wet conditions prevail, with local circulation and synoptic systems driving convective activity and hence

favoring cloud formation. The South Atlantic Convergence Zone (SACZ) affects the region in summer with notable increase of cloud cover and flood events. The SACZ can persist longer than 10 days, and usually more than 8 events occur every year (Carvalho et al., 2004).

Since the Metropolitan Area of São Paulo (MASP) is located over a plateau and about 50 km from the coast, the parallel orientation of the mountain range, with mountain-valley circulation, contributes to the advance of sea breeze inland. The sea breeze front can remain stationary over MASP by the influence of heat urban island circulations (Freitas, 2003). The sea breeze front passage occurs after midday, increasing the convection development in the afternoon. This local condition is favored in summer due to the increase of surface temperature and water vapor.

Silva Dias et al. (2013) discussed that, in the wet season, local factors such as the increase of air pollution and the growth of Sao Paulo city might have influenced the positive trend of rainfall in the last eight decades.

In winter, the region is affected by the passage of cold fronts and migratory high pressure systems and, under this condition, imposing the presence of cold dry air. Despite the fact that the highest frequency of cold fronts occurs in August, in this season cold fronts are less rainy and move faster, increasing cloud cover only near the coast (Morais et al., 2010). In spring, the maximum number of cold fronts is observed with frequency around 8 days.

2.4. Shortwave radiative transfer

The sun emits energy in the form of electromagnetic waves, especially those with wavelength below 4 µm. The sun electromagnetic spectrum is divided in ultraviolet (UV) for wavelengths between 0.1 and 0.4 µm, visible (VIS) above 0.4 µm up to around 0.7 um and near infrared (NIR) between 0.78 µm and 3.5 µm (Yamasoe and Corrêa, 2016).

Radiation can be quantified by energy per unit of time, the so called radiant power. Considering a unit of surface area, a pencil of radiation beam (given by infinitesimal solid angle) with an orientation defined by the cosine of

the zenith angle (μ) (relative to the vertical axis) also referred as CZA, and azimuth angle (ϕ) (angle along the horizontal axis) is named as radiance. Thus, radiance is radiant power per unit area orthogonal to the pencil of radiation, per unit of solid angle. The integration of all pencils of radiation in the given solid angle (in general, in one hemisphere) is the irradiance, considering a horizontal surface. Radiance is expressed in $Wm^{-2}sr^{-1}$ and irradiance in Wm^{-2}.

Through the atmosphere, solar radiation undergoes extinction processes by means of absorption and scattering. If the solar beam suffers any extinction due to the scattering, the scattered component is named diffuse irradiance or radiance; otherwise it is called as direct sun radiance or irradiance.

Scattering is a process of deviation of radiance due to interaction of the electromagnetic field of radiation and the electromagnetic field generated by particles. The scattering does not involve the transformation of energy and it is sensitive to the relationship between the size of the scattering particle and the wavelength of radiation. For particle much smaller than the wavelength of radiation, the scattering is symmetric and spectrally sensitive (Rayleigh scattering). When the particle size is comparable to the wavelength of the incident radiation, anisotropy in the scattered field is observed, theoretically explained by Mie Theory (Liou, 2002). In the *Mie* scattering, there is less spectral dependence and the forward scattering is more pronounced.

Molecular absorption is a consequence of the interaction of the electrical dipole of the molecule with electromagnetic radiation. Therefore, it depends on the geometric distribution of electrical charges of the molecule and the wavelength where vibrational and or rotational modes of the molecule are activated. Because of that, absorption of gases is highly wavelength dependent (Liou, 2002). For particles, the absorption depends on the imaginary part of the refractive index and on the relationship of the particle size to the wavelength of the incident radiation and, opposite to gases, it is spectrally continuous (Liou, 2002).

All these processes can be quantified by the shortwave radiative transfer equation (RTE). Considering a plane parallel atmosphere for spectral diffuse

radiance I_λ at any layer with height (z) and orientation (±μ, ϕ), the RTE is shown in equation 1 (Yamasoe and Corrêa, 2016), where $\cos\Theta_0$ represents the solar beam direction and $\cos\Theta'$ represents all possible incident directions of diffuse radiation. Note the dependence on single scattering albedo (ω, also known as SSA), phase function (p) and extinction coefficient (β_e) which are the optical properties characterizing the atmospheric layer. The second term on the right represents diffuse radiance generated by single scattering process (only one scattering of the solar direct beam), while the third term indicates scattering of diffuse radiance already available at that atmospheric layer (multiple scattering) to the observer direction (±μ, ϕ).

$$\pm\mu\frac{dI_\lambda(z,\pm\mu,\phi)}{\beta_{e\lambda}(z)dz} = I_\lambda(z,\pm\mu,\phi) - \frac{\omega_\lambda(z)}{4\pi}S_\lambda(z)p_\lambda(z,\cos\Theta_0) -$$

$$-\frac{\omega_\lambda(z)}{4\pi}\int_0^{2\pi}\int_{-1}^1 I_\lambda(z,\pm\mu',\phi')\,p_\lambda(z,\cos\Theta')\,du'\,d\phi' \tag{1}$$

The extinction coefficient is the sum of absorption (β_a) and scattering (β_s) coefficients and can be computed from a volume containing particles or molecules (equation 2), where $n(z)$ is the density number in any determined z and $\sigma_{e,s,a}(z)$ denotes the cross section due to extinction, scattering or absorption. The $\sigma_{e,s,a}(z)$ is calculated from the extinction, scattering or absorption efficiency ($Q_{e,s,a}(z)$) and the geometrical cross-section (A). $Q_{e,s,a}$ quantifies the extinction, scattering or absorption per cross sectional area unit, and is calculated from *Mie Theory* for aerosols and clouds. For gases, Rayleigh scattering theory is used to compute efficiencies (Liou, 2002). For absorption due to gases, equation 4 is used, where k is the mass absorption coefficient and ρ_a the density of the gas.

$$\beta_{e,s,a_\lambda}(z) = \sigma_{e,s,a_\lambda}(z)n(z) \tag{2}$$

$$\sigma_{e,s,a_\lambda}(z) = Q_{e,s,a_\lambda}(z)\,A \tag{3}$$

$$\beta_{a_\lambda}(z) = k_\lambda\rho_a(z) \tag{4}$$

$$\tau_\lambda = \int_\infty^{z'}\beta_{e\lambda}(z)dz \tag{5}$$

$$\omega_\lambda(z) = \frac{\beta_{s_\lambda}(z)}{\beta_{e_\lambda}(z)} \tag{6}$$

$$p_\lambda(\cos\Theta) = \sum_{i=0}^{2N-1} (2i+1)\, X_i\, \left(P_i(\cos\Theta)\right) \tag{7}$$

$$p_{HG_\lambda}(\cos\Theta, g_\lambda) = \frac{1 - g_\lambda^2}{(1 + g_\lambda^2 - 2g_\lambda \cos\Theta)^{\frac{3}{2}}} \tag{7.b}$$

$$g_\lambda = \frac{1}{2} \int_{-1}^{1} p(\cos\Theta)\, \cos\Theta\; d(\cos\Theta) \tag{8}$$

When β_{e_λ} is integrated along z from TOA up to the z' level, the optical depth of the medium is obtained (equation 5). This equation can be used for computing the optical depth of each atmospheric component if the β_{e_λ} due to this component is known.

The single scattering albedo is a ratio that represents the fractional part of the extinction process related to the scattering (equation 6), i. e. if ω is 1 the extinction is only due to scattering, otherwise if ω is 0 the extinction is only a consequence of absorption. The phase function (p) gives the probability of redistribution of scattered radiation. It can be computed with high accuracy using Legendre polynomials (P_i), according to equation 7 (Yamasoe and Corrêa, 2016). Legendre coefficients of each expansion are X_i and the number of terms N. The higher the size of particle the more complex the computation of p. Due to the computational cost, phase function can be computed by analytic functions such as the Henyey-Greenstein approximation, given in the equation 7b. The main input variable of Henyey-Greenstein approximation is the asymmetry parameter (g), the first coefficient X_0 (equation 8). It represents the degree of anisotropy of the phase function e .g. for Rayleigh scattering g=0 and for total forward scattering g=1 (Yamasoe and Corrêa, 2016).

The direct component of RTE (equation 9) quantifies the radiative transfer of the solar beam through a medium characterized by an extinction coefficient $\beta_{e\lambda}$. It is also known as the Beer-Lambert-Bouguer law (equation 10). The $S_{0\lambda}$ is the radiance at TOA at the standard distance of 1 unit astronomical distance between the Earth and the Sun, U is the correction factor of Earth-Sun distance and μ_0 the cosine of zenith angle in the direction of the solar beam. Equation 10 is widely used for retrieving optical properties of aerosols, water

vapor and even thin clouds using direct sun measurements (Liou, 2002; Min 2004)

The total optical depth is the sum of optical depths of every component. In equation 11, τ_{ray} is the optical depth by *Rayleigh* scattering of gas molecules. Optical depth due to absorption by gases (τ_{abs}) is the sum of optical depths of absorbing gases such as ozone, water vapor, carbon dioxide etc. In the case of semitransparent clouds blocking the solar beam, the optical depth of clouds is τ_{cld} or COD. Usually, in the presence of thick clouds, the solar direct beam is completely attenuated, with only the diffuse component reaching the surface.

The monochromatic transmittance (T_{dir_λ}) is defined by the ratio between direct radiance at any z level $S_\lambda(z)$ and $S_{0\lambda}$ (equation 12). The term μ_0^{-1} is also known as the relative optical air mass of the layer (m), but only in the plane-parallel approximation.

$$-\mu_0 \frac{dS_\lambda(z)}{\beta_{e_\lambda}(z)dz} = S_\lambda \tag{9}$$

$$S_\lambda(z) = S_{0\lambda}U \exp\frac{-\tau}{\mu_0} = S_{0\lambda}U \exp(-m\tau) \tag{10}$$

$$\tau_\lambda = \tau_{ray_\lambda} + \tau_{abs_\lambda} + \tau_{aer_\lambda} + \tau_{cld_\lambda} \tag{11}$$

$$T_{dir_\lambda}(z) = \frac{S_\lambda(z)}{S_{0\lambda}U} = \exp\frac{-\tau_\lambda}{\mu_0} \tag{12}$$

Using equations 13 and 14, the monochromatic downwelling and upwelling diffuse irradiance are computed, respectively. The spectral direct solar irradiance is SS_λ is computed integrating all the radiances in the solid angle of the solar disk (Ω_{sun}) (equation 15). The global irradiance (G) at any height is the sum of downwelling diffuse and direct sun irradiance orthogonal to the surface (equation 16). Thus, the hemispherical reflectance (R) is defined as the ratio of upwelling irradiance and G at the same height level (equation 17). The total transmittance T at any level is calculated from equation 18 as the ratio of G of the level and the global irradiance at TOA ($G(\infty)$). Note, $G(\infty)$ is

computed from direct sun irradiance at TOA in 1 astronomical unit ($SS_{\lambda 0}$) corrected by the distance factor (U) and by μ_0 or CSZA (equation 19).

$$D \downarrow_\lambda (z) = \int_0^{2\pi} \int_1^0 I (z, -\mu, \phi) \mu d\mu \, d\phi \tag{13}$$

$$D \uparrow_\lambda (z) = \int_0^{2\pi} \int_{-1}^0 I (z, \mu, \phi) \mu d\mu \, d\phi \tag{14}$$

$$SS_\lambda(z) = \int_{\Omega_{sun}} S_\lambda(z, \mu, \phi) \, d\Omega(\mu, \phi) \tag{15}$$

$$G_\lambda(z) = SS_\lambda(z) \mu_0 + D \downarrow_\lambda (z) \tag{16}$$

$$R_\lambda(z) = \frac{D\uparrow_\lambda(z)}{G_\lambda(z)} \tag{17}$$

$$T_\lambda(z) = \frac{G_\lambda(z)}{G_\lambda(\infty)} \tag{18}$$

$$G_\lambda(\infty) = SS_{\lambda 0} U \mu_0 \tag{19}$$

Hereinafter the downwelling broadband diffuse irradiance is defined as D and direct sun irradiance as SS when they are integrated over λ. For specific wavelength a subscript will be employed.

2.4.1. Cloud optical and radiative properties

Effective radius (r_e) and liquid/ice water content (LWC/IWC) are the cloud properties better related to the cloud optical properties (ω, g and COD). The r_e for liquid clouds is computed as the ratio of the integrated third and second moments of size distributions (equation 20). It represents the mean radius weighted by the cross sectional area of drops. LWC is the sum of the mass of all drops in the distribution (equation 21). For this parameter, the knowledge of the number distribution $N(r)$ and the density of liquid water (ρ) is necessary (Yamasoe and Corrêa, 2016).

In the shortwave spectrum, cloud optical properties are insensitive to the shape of cloud drop size distribution and mainly depend on r_e, LWC or IWC and wavelength (Hu and Stamnes, 1993). The ω and g only depend on r_e and wavelength (Rawlins and Foot, 1989). Spectral optical properties of clouds in

the homogenous plane parallel conditions are frequently characterized by r_e and COD.

$$r_e = \frac{\int_0^\infty \pi r^3 N(r)\,dr}{\int_0^\infty \pi r^2 N(r)\,dr} \qquad (20)$$

$$LWC = \frac{4\pi}{3}\rho \int_0^\infty r^3 N(r)\,dr \qquad (21)$$

Because the size of cloud drops is larger than the wavelength of solar radiation, The Mie Theory is considered for computing cloud optical properties taking into account the refractive index and radius of particle. For liquid clouds $\beta_{e,s,a}$ is calculated by integrating the $Q_{e,s,a}$ over drop size distribution $(n(r))$ (equation 22).The Q depends on wavelength (λ), refractive index (*ni*) and radius (r) of given cloud particle.

$$\beta_{e,s,a_\lambda} = \int_0^\infty \pi r^2 Q_{e,s,a_\lambda}(r,ni)n(r)dr \qquad (22)$$

Since Q_e tends to a constant value of 2, for larger size of cloud drops as compared to the wavelength of solar radiation, it is possible to derive a simple relationship between β_e, r_e and LWC (equation 23):

$$\beta_e \approx \frac{3\,LWC}{2r_e} \qquad (23)$$

Scattering and absorption properties of ice particles cannot be computed using the Mie Theory because of the non-spherical characteristics of ice particles, instead ray tracing technique is employed (Yang et al., 2000). For ice clouds r_e is obtained using the maximum dimension (L) of ice particle (equation 24), where V and A are the equivalent volume and the projected area assuming a spherical particle (Yang et al., 2000). The IWC can be retrieved from the distribution number of particles in function of L, $N(L)$, by equation 25, assuming the density of ice (ρ_{ice}) as 0.9167 g.cm^{-3} (Key et al., 2002).

$$r_e^{ice} = \frac{\int_0^\infty V(L)N(L)dL}{\int_0^\infty A(L)N(L)dL} \qquad (24)$$

$$IWC = \rho_{ice} \int_0^\infty V(L)N(L)dL \qquad (25)$$

In the Figure 2 the spectral optical properties estimated using the parameterization developed for liquid clouds (Hu and Stamnes, 1993) and for rough-aggregated "habit" of ice clouds of Key et al. (2002) are shown. For liquid clouds, optical properties are presented for r_e values of 5 μm, 10 μm and 15 μm. In the case of ice clouds they are computed for r_e equal to 30 μm, 51.2 μm and 70 μm. Differences of *g* between clouds are observed, with higher values for liquid clouds in the spectral range from 0.2 μm up to 1.5 μm (Figure 2.a). Thus, for the same cloud optical depth, for liquid clouds more forward scattering and hence a higher transmission of solar radiation is expected as compared to ice rough-aggregated (near 3D ice) (LeBlanc et al., 2015). However, for plates and columnar ice particles, *g* can be higher than for liquid clouds (Key et al., 2002).
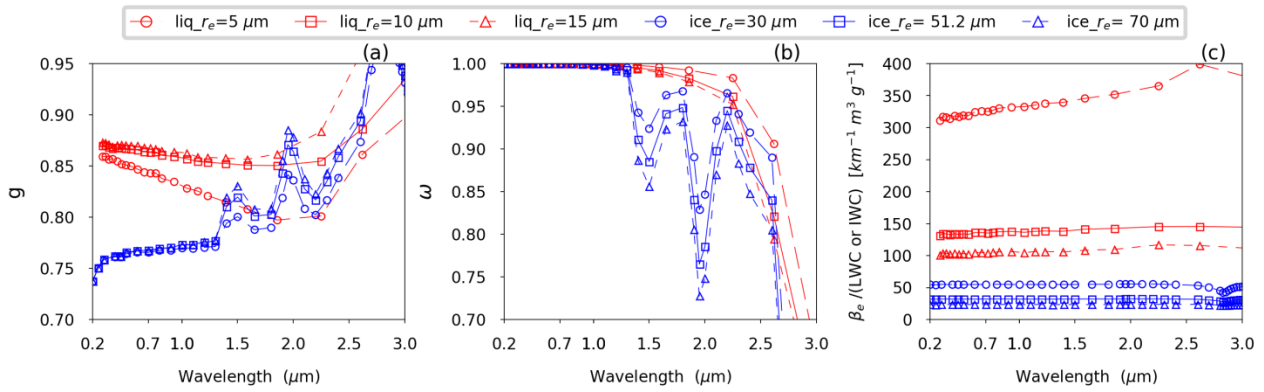
Figure 2: Asymmetry parameter (g) (a), single scattering albedo (**ω**) and the ratio between the extinction coefficient and LWC or IWC (β_e/LWC or IWC) for liquid and ice clouds. For liquid clouds, Hu and Stamnes (1993) parameterization is employed and for ice clouds, the parameterization of Key et al. (2002) for rough-aggregate habit is used. The optical properties are computed for r_e values of 5,10 and 15 μm for liquid clouds and for 30, 51.2 and 70 μm for ice clouds.

Asymmetry parameter *g* is sensitive to r_e (Figure 2.a), while ω near 1 confirms that for clouds, scattering dominates in wavelengths below 1.1 μm. The absorption of radiation by clouds (ω below 1) is observed for wavelength higher than 1.1 μm (Figure 2.b) (Marshak et al., 2000). In the solar spectrum, the extinction coefficient is almost spectrally constant, especially for larger r_e (Figure 2.c). β_e decreases with r_e and strongly depends on LWC or IWC.

Although Q_e converges to 2 for large size parameter ($^{2\pi L}/_{\lambda}$) also for ice clouds (Yang et al., 2000), the optical properties of ice clouds depend on the particle habit. Differences are significant for *g* in the visible spectrum. Larger ice

plates have strong forward scattering with values of g around 0.94. Solid how columns and bullet rosettes have maximum values of g near 0.86 while for aggregate, the maximum hardly reaches 0.8. Thus, in the *VIS*, the *R* of cloud is higher (0.65 for COD of 6) for aggregates and solid columns and lower (0.52 for COD of 6) for ice plates (Key et al., 2002).

The *R* of clouds is more sensitive to r_e than *T*, especially in spectral regions where the single scattering albedo of clouds is less than 1 (Rawlins and Foot, 1989). That is because variations of r_e lead to g and ω or *SSA* responses in the same direction. i. e., the increase (decrease) of r_e increases (decreases) the absorption efficiency and forward scattering, contributing to the decrease (increase) of R. Because of that, retrieving r_e by measurements of solar radiation reflected by clouds onboard satellites is more effective (McBride et al., 2011). At the surface, the opposite behavior of SSA and g causes the less sensitivity of T to r_e. In the NIR, larger r_e results in lower SSA values, reducing T. The increase of the forward scattering, for larger r_e, results in the increase of T. Thus, T measured at the surface in the presence of clouds is more sensitive to COD than to r_e (Min and Harrison, 1996). For wavelengths below 1.1 µm, the higher the r_e leads to the increase of radiance at zenith due to the direct impact of the forward scattering. By contrast, for wavelength about 1.4 µm, as the absorption process becomes more important, the transmitted radiance at zenith decreases (McBride et al., 2011).

The first works studying cloud and solar radiation interactions focused on the bulk radiative properties of clouds, i.e reflectivity known as cloud albedo, absorptivity (the amount of solar radiation absorbed by the cloud layer) and transmissivity.

One of the first results in the scientific literature about the cloud effects on solar radiation appeared in the 40's of the last century (Neiburger, 1949).The author computed bulk radiative properties of clouds using downwelling and upwelling shortwave radiation measurements below, inside and above the coastal stratus clouds in the United States. He showed that the cloud effects depended on cloud thickness and confirmed, by measurements that the cloud albedo is the most important property. In addition, low cloud absorption was

observed. In that epoch, they argued the need of increasing observations of cloud microphysical properties.

Paltridge (1974) combined radiative and microphysical measurements made in stratocumulus clouds. He observed the increase of LWC at high layers of clouds near the cloud top, with the strong albedo relationship with LWC, therefore the highest albedo was observed near the cloud top.

Manton (1980) showed the increase of cloud albedo with drops number, which is higher for thin clouds. Differences were also observed between maritime and continental clouds, with the continental reflecting 5 % more than maritime clouds. He also showed the decrease (increase) of reflectivity with r_e (LWC). The higher reflectivity near cloud top was strongly related with the increase of density in this part of the cloud. In addition, the reflectivity (transmissivity) increased (decreased) for lower CSZA especially lower than 0.5.

Ackerman and Stephens (1987) argued that the scattering properties of clouds do not depend on droplet size distribution. The cloud absorption efficiency decreases as an inverse function of r_e for thin clouds. For deeper clouds they showed an opposite behavior, with increasing absorption efficiency for higher r_e.

2.4.2. Retrieving COD and r_e from ground based measurements

Ground-based measurements are useful sources of data to study the radiative processes in the atmosphere and for validation of satellite measurements. Around the world, there are still few sites, especially in the southern hemisphere. A variety of methods for computing cloud optical properties from passive ground-based measurements has been developed in the last two decades.

Two approaches for retrieving COD from passive ground-based instruments are reported in the literature: using broadband or narrowband G,

the so called effective cloud optical depth (ECOD) and COD retrieved locally by using zenith radiance measurements. The former works well for clouds with total overcast conditions and using 1D radiative transfer model, because the one to one relationship can be observed between irradiance and COD. In the case of broken cloud fields, each element of the sky contributes differently to the irradiance (Marshak et al., 2004), even with *enhancement* effects, due to 3D effects of clouds.

Retrieving COD locally has the disadvantage of no one to one relationship between zenith radiance and COD. Therefore, using combinations of spectral radiance measurements is needed (Brückner et al., 2014; Chiu et al., 2010; Marshak et al., 2004). In the following, examples of methods found in the literature are described.

Leontyeva and Stamnes (1994) proposed the COD estimation from transmitted irradiance using a broadband pyranometer. They projected a simple model assuming plane parallel homogenous clouds, without considering the cloud type or cloud base height. The possible influence of water vapor is not well represented. They suggested the use of this methodology, but employing a more accurate model and measurements in the *UV* and *VIS* to avoid the influence of water vapor absorption in the infrared.

Barnard and Long (2004) proposed a simple method for the estimation of COD using a relationship of COD to G with cases of clouds with total overcast conditions. They did not consider in depth the atmospheric conditions for the retrieval; therefore it is less accurate than methods employing spectral measurements. They also suggested avoiding the use of the method when high accuracy is needed.

Min and Harrison, (1996) retrieved COD of warm clouds in total overcast conditions using T_{415} and surface albedo computed from a Multi-Filter Rotating Shadowband Radiometer (MFRSR). They also retrieved r_e from vertical liquid water path measured by zenith-viewing microwave radiometer (MWR). The retrieval employed a 1-D radiative transfer model based on the discrete ordinate method. The advantage of using measurements at channel centered at 415 nm instead of other spectral regions is argued: the lower surface albedo, the less

sensitivity of *SSA* and *g* to r_e and because the absorption of radiation by ozone in the *Chappuis-band* can be avoided. COD is retrieved by nonlinear square method considering cloud properties as stationary in fixed time intervals, by minimizing the sum of errors in transmittance. The poor ability to distinguish higher optical depths from satellite measurements at the top of the atmosphere and the lower uncertainties of retrieving COD from ground-based measurements were demonstrated.

The best accuracy, close to 5 %, of COD retrieved for thin clouds from MFRSR was obtained by Min (2004). The method used direct sun irradiance obtained from MFRSR measurements. A correction for the forward scattering to avoid underestimation due to the increase of the diffuse contribution in the direct orientation was developed. The method employed the Bouguer-Lambert-Beer Law (see equations 10-11) and aerosols can be discriminated from clouds, using the spectral relationship between the optical depth at 415 nm and 860 nm, with the Ångström exponent (equation 37). It is only applied to thin clouds, when the direct sun irradiance can be measured.

On the other hand, Marshak et al. (2000) proposed a method for locally retrieving COD of low broken clouds above green vegetation, using the spectral contrast of albedo in VIS and NIR for vegetated surface in the presence of low liquid clouds. COD of clouds is almost constant in the shortwave spectral range. Therefore in the presence of clouds, radiance at zenith is strongly influenced by multiple scattering between surface and cloud base. They used the spectral radiance at 650 nm and 870 nm normalized to the radiance at the top of the atmosphere. By analogy with the normalized difference vegetation index (NDVI), they defined the Normalized Difference Cloud Index (NDCI). The NDCI index minimizes the *enhancement* effect of zenith radiance due to broken low cloud fields and shows a good agreement with COD for horizontal resolution higher than 0.4 km. In addition, the method does not take into account the cloud fraction, that can lead to poor retrievals.

Based on the relationship of COD with spectral radiance previously explained, Chiu et al. (2010) proposed a method to compute COD applied to AERONET measurements, in conditions when aerosol properties cannot be

retrieved, called the cloud mode. They used zenith radiance between 440 nm and 870 nm to take the advantage of more spectral contrast of surface albedo. This method is effective for low broken cloud fields and it is very sensitive to aerosol properties, but the authors did not show the errors due aerosols, arguing that COD retrievals frequently are higher than 15. The total error of the retrieval is about 17 %, with 4 % due to the r_e error of 25 %.

McBride et al. (2011) developed a method to retrieve *COD* and r_e from zenith transmitted radiance at 515 nm and the slope of transmitted radiance at 1565 nm and 1634 nm normalized to radiance transmitted at 1565 nm. The method takes advantage of the variability of spectral absorption efficiency of clouds in the NIR to obtain the best accuracy for retrieving r_e. That resulted in higher sensitivity of the normalized transmittance at NIR to r_e.

Differences in the shortwave spectral absorption due to the cloud phase was taken into account by Le Blanc et al. (2015). They derived 15 parameters to obtain *COD*, r_e and cloud phase from spectral transmittance given the cloud type. But only 2 parameters are derived in the spectral range of *VIS*, with the rest in the NIR.

Brückner et al. (2014) retrieved *COD* and r_e from 3 ratios of transmissivity using six spectral ranges (450nm, 680 nm, 1050nm, 1250 nm, 1670 nm, 1560 nm) of zenith radiances. The method is applied to homogenous and heterogeneous liquid water clouds and cirrus clouds using a 1-D radiative transfer model. Using combinations of these transmissivity ratios, problems related to the retrievals of COD lower than 5 were reduced. Errors of retrievals were near 5 % for low clouds and 10 % for ice clouds, increasing for thicker clouds.

2.4.3. Computing the shortwave radiative effects of clouds

The shortwave cloud radiative effect (CRE) is a variable that quantifies the amount of net solar irradiance, or G, affected by the influence of clouds at a horizontal surface. It can be computed using the $D \uparrow_{cld}$ and G (Salgueiro et al., 2016) in equation 26 or only using G (Tzoumanikas et al., 2016) in equation 26. In the equations 26 and 28, the subscript *clear* represents computations under

clear sky conditions; usually a radiative transfer model is employed to obtain this value. The subscript *cld* corresponds to the irradiances measured in cloudy conditions. Sometimes $D\uparrow_{cld}$ is not measured directly, therefore the use of surface albedo (α), is needed as shown in equation 27. By the equation 28, CRE can be computed not including the surface albedo. The CRE is given in W m^{-2} and negative values indicate a cooling effect, due to extinction of irradiance by clouds. Positive values confirm the *enhancement* effect or the increase of solar radiation at the surface due to 3D scattering effects by clouds.

$$CRE = G_{cld} - D\uparrow_{cld} - G_{clear} + D\uparrow_{clear} \tag{26}$$

$$D\uparrow_{cld} = \alpha\,G_{cld} \tag{27}$$

$$CRE_G = G_{cld} - G_{clear} \tag{28}$$

The CRE decreases with CSZA and increases with cloud cover (Tzoumanikas et al., 2016). Other variables are used instead of CRE in order to minimize the CSZA effect: the normalized cloud radiative effect (NCRE) (Salgueiro et al., 2016) (equation 29) and cloud modification factor (CMF) (equation 30). They are variables computed as the ratio of G in all sky conditions to G in clear sky ones, and they almost totally eliminate the solar zenith angle effect.

$$NCRE = \frac{CRE_G}{G_{clear}} \tag{29}$$

$$CMF = \frac{G_{cld}}{G_{clear}} \tag{30}$$

2.4.4. Cloud radiative efficiency (CEF)

To quantify how the cloud radiative effect changes per COD unit, the cloud radiative efficiency (CEF) is defined. The CEF is computed from the relationship between the cloud radiative effect and COD. In the case of cloud with COD below 3 a linear relationship between CRE and COD for any CSZA are observed, but for higher values of COD an exponential relationship is expected and CEF is computed from linear relationship between CRE and ln(COD) for ranges of CSZA (Mateos et al., 2014).

In equations 31-33, CEF can be estimated according to Mateos et al., (2014) where b is the slope of the relation for different values of CSZA. CEF computed from CRE has unit of Wm^{-2} (COD-unit)-1 (Mateos et al., 2014), while NCRE is in (COD-unit)$^{-1}$ or % (COD-unit)$^{-1}$ if NCRE is given in percent values (Salgueiro et al., 2016).

$$CRE = a + \text{b} \ln(COD) \tag{31}$$

$$b = \frac{\Delta CRE}{\Delta COD} COD \tag{32}$$

$$CEF = \frac{\Delta CRE}{\Delta COD} = \frac{b}{COD} \tag{33}$$

CEF is sensitive to CSZA and COD when it is computed from CRE (Mateos et al., 2014), it increases with CSZA and decreases with COD. Mateos et al. (2014) showed a maximum efficiency of -160 W/m^2 per COD unit at high CSZA and low COD and minimum of -0.3 W/m^2 per COD unit when CSZA is lower with moderate-large COD. They retrieved COD using broadband pyranometer measurements with less accuracy, showing a strong relationship between COD and CRE for a fixed CSZA. In contrast, (Salgueiro et al., 2016) achieved the best accuracy when CEF was computed based on the linear relationship between NCRE and ln(COD).

2.4.5. The *enhancement* effect of clouds on the solar radiation

In the presence of clouds, if the solar disk is not obstructed, the direct solar irradiance is not attenuated and the diffuse irradiance can increase. Due to this effect, called *enhancement*, the solar G measured at the surface can be higher than the solar G measured under clear sky conditions keeping all other variables identical.

The increment of diffuse irradiance is whether can be a consequence of the multiple reflection of the direct solar irradiance in the border of clouds or the increase of forward scattering by the cloud (Tzoumanikas et al., 2016). In special cases, G can overcome an equivalent G at the top of the atmosphere.

According to Almeida et al. (2014) these events are called as *overirradiance events*.

Tzoumanikas et al (2016) argued that the necessary conditions for cloud solar *enhancement* events are: the presence of cumulus clouds, very dense but not blocking the solar disk, with a minimum value of 50 % and maximum of 90 % cloud cover. These events can last from few seconds to minutes and, in extreme cases, the measured downward irradiance can be higher than 1500 W/m^2 (Tzoumanikas et al., 2016). They observed maximum enhancement of 200 W/m^2, occurring in the presence of high and mid-level clouds, values comparable to low clouds. The position of the solar disk relative to the clouds is a crucial condition for strong enhancement: solar disk near clouds or low CSZA with clouds present near zenith (Tzoumanikas et al., 2016). Marín et al. (2017) showed that the *enhancement* can be observed at any time of the day CSZA and the maximum is observed between 40-50 % of cloud cover. They reported a median of NCRE of 0.18 and percentile 75 of 0.3 at Valencia, Spain. Enhancement effects at São Paulo were reported before, with the presence of *overirradiance* events with time resolution shorter than 1 minute, which were related to broken cumulus (Almeida et al., 2014).

2.4.6. The shortwave attenuation effect of clouds

The shortwave cooling effect of clouds at the surface is determined when values of *CRE* or *NCRE* are negative. It represents the reduction of solar radiation at the surface by clouds, as compared to clear sky at the same time.

Tzoumanikas et al (2016) observed maximum of CRE near -900 W/m^2 computed with surface albedo. They reported in Greece, strong cooling effects due to *Sc* and *Cb* near -800 W/m^2 with *CSZA* around 0.86. *Cu* has cooling effects as high as Sc, but a high variability of CRE was reported with many cases below -200 W/m^2. In the tropical Western Pacific region, Burleyson et al. (2015) reported the strongest cooling for *Cb* with *NCRE* values between -0.81 and -0.84, for low clouds between -0.37 and -0.48, cirrus and mid clouds presented mean values of *NCRE* comparable to boundary layer low clouds with mean between -0.17 and -0.57 and -0.32 and -0.44, respectively.

At São Paulo, Yamasoe et al. (2017) reported higher cooling effects computed using 24 h mean irradiance in summer of -170 Wm^{-2} and in winter of -50 Wm^{-2}. They computed mean values of CMF of 0.3 and 0.8 for low and high clouds respectively.

3. Instruments and methods

3.1. Satellite data

3.1.1. Description of satellites

The A-train satellite afternoon constellation is a group of polar orbiting satellites sharing the same orbit one after another. The time lapse between the first and the last satellite is only around 15 minutes. Inside this constellation *CALIPSO* and *CloudSat*, launched in 2006, make measurements with intervals of 15 seconds. The constellation is known as the afternoon due to its overpass over the equator at 13:30 local time. Near São Paulo, the overpass occurs in the afternoon around 14:00 LT and near 01:00 LT at night.

CloudSat (acronym of Cloud Satellite) allows estimating the vertical structure of clouds and precipitation. The main instrument onboard is the microwave radar with nadir view called Cloud Profiling Radar (CPR) that measures backscattering from cloud particles at 94 GHz (3.2 mm). The footprint at sea level has a resolution of 1.7 km and 1.3 km along and across track, respectively. The vertical resolution of bins is about 240 m and the minimum detectable radar reflectivity factor is approximately −30 dBZ. Because of the wavelength of 3.2 mm, CPR of CloudSat is less sensitive to smaller cloud drops (subvisual cirrus or shallow water droplets), but it can penetrate optically thick clouds. Moreover, no valid measurements near the surface, specially under 1 km, can be made, due to the backscattering contamination from the surface (Marchand et al., 2008). The CPR only detects 30 % of clouds under 1 km and fails in 40 % for retrieving cloud properties due to the limitations of CPR (Christensen et al., 2013). Since April of 2011, measurements by the satellite are made only during daytime, because of a battery anomaly.

CALIPSO (acronym of the Cloud-Aerosol Lidar and Infrared Pathfinder Satellite Observations) satellite has aboard the Cloud-Aerosol Lidar with Orthogonal Polarization (CALIOP). From CALIOP measurements, backscattering coefficients at 532 nm and 1064 nm and depolarization ratio at 532 nm are retrieved. The main vertical and horizontal resolutions are 30 m and 333 m, respectively up to 8.2 km, and from 8.2 km until 20 km the vertical and

horizontal resolutions are 60 m and 1 km respectively (Winker et al., 2009). With CALIPSO, smaller cloud drop such as from sub visual cirrus or semitransparent clouds of boundary layer, can be detected. Hence, the synergy of radar and lidar is very powerful because the constraints of each instrument on detecting clouds are minimized.

3.1.2. CloudSat and CALIPSO products

In this research, microphysical variables for liquid clouds are obtained from *2B-CWC-RO* products of CloudSat. The data can be downloaded in the following website: http://www.cloudsat.cira.colostate.edu/). In addition, because of this product also has profiles for liquid clouds available, cloud properties such as cloud thickness can be estimated for low clouds.

For ice clouds, properties are obtained from *CSCA-Micro* of *JAXA* products (*http://www.eorc.jaxa.jp/EARTHCARE/research_product/ecare_monito.html*). Cloud particle definition from *CA-Ctype* was used to estimate the frequency of *habit* for layer and for clouds. Cloud mask of lidar/radar from *CSCA-Cmask* was employed to compute the geometric properties cloud base for liquid and ice clouds and thickness for ice clouds. Cloud frequency by height level was also obtained for each season and according to distance from the coastal line. The coastal line distance was estimated as the minimum distance of the measurement point to the coast. The computations of frequency of occurrence are valid if at least 100 measurements were found in every layer, or every bin selected of coastal distance.

The time period of *2B-CWC-RO* spans from December 2007 to June 2016 with a total of 436 overpasses. Quality control was made neglecting measurements under precipitation and uncertainties above 20 %. In addition, a total of 382 overpasses were found in *JAXA* products in the full period between July 2006 and August 2015. In the following, the methodology of retrieving each product is briefly described.

3.1.2.1. CloudSat

Liquid water content (LWC), ice water content (IWC), effective radius (r_e) are included in the Cloud Water Content using Radar Only product (2B-CWC-RO) from CloudSat products. The retrieval algorithm uses at first a cloud mask from 2B-GEOPROF product to detect the layer with presence of clouds (Mace, 2007). Later, it employs 2B-CLD-CLASS product where cloud types are defined and allows for checking if a level previously classified as cloudy is undetermined or invalid which indicates troubles in the vertical profile of clouds (Austin, 2007). The algorithm assumes the entire profile with ice or water clouds.

Finally, microphysics properties are retrieved using a forward scattering model using a priori information of size distribution of drops. The model considers lognormal size distribution depending on three parameters. In addition, the radar reflectivity, LWC/IWC and r_e are related with the same three parameters. Thus, the final retrieval is made by iteration from a priori information up to the convergence of the solution (Austin, 2007). The algorithm underestimates r_e and *LWC/IWC* in the presence of precipitation, dBZ>-15, because it does not consider the size distribution of precipitating drops (Austin, 2007). Christensen et al. (2013) showed the high uncertainty in the retrieval for mixed-phase profile due to the erroneous selection of refractive index. 2B-CWC-RO has a horizontal resolution of 1.1 km with 125 vertical levels of 240 m each.

3.1.2.2. CloudSat-CALIPSO (JAXA products)

Recently, a synergy between *CALIPSO-CloudSat* was publicized by the EarthCARE Research Product Monitor of Japan Aerospace Exploration Agency (JAXA), where between others, microphysics properties of ice clouds, a new cloud mask and cloud type particle or habit of ice clouds are available. Products of JAXA Radar/Lidar Cloud Mask Product (CSCA-Cmask), Lidar Cloud Particle Type Product (CA-Ctype) and Radar/Lidar and Cloud Microphysics Property Product (CSCA-Micro) were employed in this research.

CSCA-Cmask includes a new cloud mask from merged *CALIPSO-CloudSat* cloud masks. This new cloud mask developed by Hagihara et al. (2010) incorporated and improved cloud mask from *CALIPSO* and cloud mask from 2B-GEOPROF of *CloudSat*. They applied two criteria for defining a cloudy

bin: the first considering a threshold of total attenuated backscattering coefficient at 532 nm, the second one, a continuity test. The continuity test is based on grouping bins along track into a two dimensional space and a new bin is considered cloudy if at least half of pixels in the space are considered cloudy by the first criterion.

The improved cloud mask from *CALIPSO* better classifies the clouds as compared to the vertical feature mask (VFM) from original CALIPSO datasets; especially for low clouds over dust. The new *CALIPSO-CloudSat* cloud mask improves the *CloudSat* mask, especially for cloud tops below 720 m above the ground (Hagihara et al., 2010).

CA-Ctype includes phase and type of cloud particle. Yoshida et al. (2010) developed a method for discriminating cloud particle type based on the relationship between depolarization ratio and ratio of backscattering coefficient between two consecutive layers (X). It is based on the fact that liquid drops have values of depolarization ratio as higher as for the case of ice drops, but differences are found for X, because it is proportional to the first layer optical depth. Discrimination based on temperature is also considered. The following cloud particles types are considered: 3-D ice, 2-D plate, warm water and supercooled water.

Cloud microphysics properties such as r_e for ice clouds and *IWC* are included in *CSCA-Micro* product. The combinations of radar-lidar for retrieving microphysics properties are more accurate than only using Radar (Okamoto et al., 2010). Thus, r_e and *IWC* are retrieved by using lookup-tables where radar reflectivity (Ze), depolarization ratio and attenuated backscattering coefficient are the input variables. In the retrieval, specular reflection is taking into account improving the accuracy of the method for cases with presence of 2-D plates (Okamoto et al., 2010). The method is also applied for only radar or lidar cloud mask, but input variables that cannot be measured are inferred from relationships previously computed in the overlap radar-lidar layers in the same profile.

The A-train trajectory does not overpass the *campus USP* (23.56° S, 46.73° W). The nearest overpass occurs at a minimum distance of 25 km with

the maximum frequency of overpasses near 75 km. Therefore, data from overpasses distant at maximum 100 km from the ground site were selected.

3.2. Ground based measurements

At IAG meteorological station, far away 15 km to the Campus USP, visual observations are made along with variables of weather conditions measurements. Moreover, on the top of the Pelletron building (30 m height above ground surface) at the *Instituto de Fisica da Universidade de São Paulo* (IF-USP) in the Campus USP, three instruments are installed: sun-photometer from CIMEL, model CE318, Multifilter Rotating Shadowband Radiometer (MFRSR) from Yes Inc., and a broadband pyranometer from Kipp & Zonen, model CM21. Furthermore, nearby at Center for Lasers and Applications (CLA) of the Nuclear and Energy Research Institute, a total sky camera and Raman lidar are also running continuously.

3.2.1. Visual observations of clouds[1]

At IAG meteorological station (23,65° S, 46,61° W, 800 m a.s.l) with a since 1957, clouds are reported by human visual observations every hour from 7:00 Local Time (LT) up to 0:00 LT. A total of 12 cloud types are reported: fractocumulus (Fc) and fractostratus (Fs), along with 10 main cloud types defined by the World Meteorological Organization (WMO). In addition to cloud type, the cloud amount (cloud cover) at each height level (low, middle and high) is also reported (in tenths). This cloud amount is reported from a surface reference point; and the sum of the cloud amount reported at each level reaches a maximum of 10 tenths.

3.2.2. Pyranometer

The pyranometer measures G at the surface, integrated from 305 nm up to 2800 nm, with a time resolution of 1 minute. It is provided with a thermal detector where energy is absorbed and converted to voltage. Measured units

---

[1] *This section is part of Datasets and Methods of a paper submitted to the International Journal of Climatology, ID=JOC-18-0083, for possible publication.*

are converted to W m^{-2} using a calibration factor. It is calibrated about every two years at LIM (*Laboratório de Instrumentos Meteorológicos from Instituto de Pesquisas Espaciais - INPE*). Database of pyranometer measurements spans from January 2016 until September 2017.

3.2.3. Multifilter Rotating Shadowband Radiometer (MFRSR)

Aside the pyranometer, two MFRSRs, numbered 345 and 368, make, simultaneous measurements every 1 minute. The MFRSR measures G_λ, SS_λ, and $D\downarrow_\lambda$, at 5 narrowband channels centered at wavelengths: 415 nm, 670 nm, 940 nm, 870 nm, 1036 nm. It has an automatic band that blocks the sun allowing to measure $D\downarrow_\lambda$. The SS_λ is retrived from the difference between G_λ and $D\downarrow_\lambda$ using the CSZA as shown in the equation 17. In addition, the instrument has a broadband silicon detector which measures global and diffuse irradiance in the spectral range from 300 to 1100 nm.

The MFRSR 345 narrow band channels are calibrated every two years; thus, spectral corresponding values at the top of the atmosphere (TOA) are estimated. A total of 118523 measurements were made with this instrument, spanning only 6 months of data from September 2016 up to February 2017. Data from instrument 368 were employed for radiative computations and cloud properties retrievals, since it was running from June 2012 until September 2017.

There are some measurement gaps for MFRSR 368: December 2012, January 2014, from May to September 2014, November 2014, January 2015 and from April to July 2015. To calibrate MFRSR 368, coincident measurements with MFRSR 345 were used, as will be detailed in section 3.5.2.

3.2.4. AERONET sun-photometer

Sun-photometer CIMEL, model CE318, is an automatic sun/sky spectral radiometer with 1.2 ° field of view (FOV) which measures direct sun and sky radiance in spectral narrow bands. The instrument placed in the site of USP campus USP (23.56 °S, 46.73 °W) has 8 spectral bands centered at 340 nm, 380 nm, 440 nm, 500 nm, 675 nm, 870 nm, 940 nm, and 1020 nm. Direct sun measurements are carried out in the eight bands. AOD (except at 940 nm) and

precipitable water vapor (at 940 nm) are retrieved from inversion methods using spectral direct sun irradiances applying the Beer-Lambert-Bouguer law. It returns to NASA Goddard Space Flight Center facility every two years for calibration purposes.

Sky radiance measurements are employed for retrieving other properties of aerosols e.g. size distributions, asymmetry parameter and single scattering albedo (Dubovik and King, 2000). The surface albedo is also obtained by combination of sky radiance and TOA measurements made by satellites (Sinyuk et al., 2007). Spectral surface albedo is given at 440 nm, 670 nm, 870 nm and 1020 nm using Moderate Resolution Imaging Spectroradiometer (MODIS) data, at or near the channels the of sun-photometer.

COD is retrieved from radiance measurements made at zenith at 440 nm and 870 nm, in conditions where direct sun measurements are impossible to make due to obstruction of sun disk by clouds (Chiu et al., 2010). The methodology is better detailed in section 2.4.3. Since November of 2000 sun-photometer is working at the site retrieving aerosol properties. COD began to be retrieved in May 2016. Measurements of sun-photometer are made each 15 minutes, but in some cases around sunrise it is reduced to 5 minutes.

For AOD, there are 3 quality levels: level 1.0 which is not cloud screened, 1.5 for cloud screened and 2.0 for cloud screened and post calibration. In the case of COD, there are two levels: 1.0 and 1.5. For COD, at level 1.0, the retrieval is made by using climatological values of surface spectral reflectance and for COD level 1.5, the spectral surface reflectance is obtained from MODIS measurements. COD are retrieved every 15 min if clouds are present, while each measurement takes about 1.5 min.

For this research, the following variables from sun-photometry were used: spectral AOD, Ångström exponent, SSA, g, surface albedo, COD and precipitable water vapor. In addition, ancillary information on NO_2 and O_3 column integrated data was also employed. Data were downloaded from the site: https://aeronet.gsfc.nasa.gov/ .

3.2.5. Sky camera

At Center for Lasers and Applications (CLA) of the Nuclear and Energy Research Institute (IPEN) (Latitude: -23.56°: Longitude: -46.74°, 740 m above sea level), total sky camera J1006 is working since August 2016.

The camera is a weatherproof automatic system that captures cloud cover with a fisheye lens. It has a resolution of 4M pixel and includes a processor to perform digital images. Moreover, a powerful "Find clouds" software allows to classifying the clear sky, total hemispheric cloud cover, optically thick and thin clouds, direct sun detection and cloud cover of the free and above artificial horizon.

In this research, regular pictures each 5 min were used from August 2016 to September 2017. Images can be obtained in the website: http://gescon.ipen.br/leal/10-1.Measurements-2018.html .

3.2.6. Lidar

In the CLA of IPEN, since 2001, there is a multiwavelength Raman Lidar installed. The fundamental emission is made at 1064 nm and additional emissions at 532 and 355 nm are made using second and third harmonic generators. The detection and spectral selection is made in the following wavelengths: 1064 nm, 532 nm and 355 nm, 607 nm, 387 nm, 408 nm (da Silva et al., 2017).

In this research, backscattering coefficient profiles of measurements at 532 nm were employed for around two days for each month of clear sky conditions observed in 2015. A fixed value 60 of aerosol lidar ratio is assumed and the profile defined between 300 and 6000 m above ground. Aerosol extinction coefficient profiles from the system were employed.

3.3. Methodology of cloud climatology from visual observation[2]

Cloud amount reported from visual observations per height level does not represent the actual cloud cover for mid or high clouds when they are present

---

[2] *This section is part of Datasets and Methods of a paper submitted to the International Journal of Climatology, ID=JOC-18-0083, for possible publication*

with lower clouds. In order to infer the amount of clouds when they are hidden by lower clouds or mid and lower clouds, a random overlap assumption (Tian and Curry, 1989) is applied and shown in equation 34. The terms i and i-1 are the current level and the level below it, respectively, *N* is the cloud cover or cloud amount in the respective level. When high clouds are present with mid and low clouds, cloud cover of the underlying level is the sum of cloud cover of low and middle level clouds reported by the observer.

The real cloud cover N_i^R can be estimated with a maximum of 7/10 of the sky obscured by underlying level clouds. With the presence of a Cumulonimbus cloud (Cb) this equation is not employed due to the weakness of the relationship (Tian and Curry, 1989).

$$N_i^R = \frac{N_i}{(10 - N_{i-1})} \cdot 100 \qquad (34)$$

For this research, only daytime (7:00-18:00 LT) cloud data were analyzed due to restrictions to observe clouds at night. Observations from 1957 up to 2016 were considered, spanning a total of 59 years.

Cloud occurrence frequency (fq) for each cloud type is computed as the ratio between the number of cases of each cloud type reported at a given height level and the total number of cloud observations in that level. For mid and high clouds, the height level is observable and considered viable if there is at least 3 tenths of the sky free of clouds to make sure that clouds are observable. This condition is very important for high level clouds, because in several occasions, the presence of lower clouds does not allow to observe possible higher clouds, which consequently are not reported, producing underestimated frequency values.

Cloud amount when cloud is present (awp) is the mean of cloud cover computed when a cloud type is reported alone at a particular height level. Mean cloud amount (amt), is the mean cloud cover computed, and for each cloud type can be estimated from frequency and awp (equation 35). Values of awp are converted to percent values for better analysis.

$$amt(\%) = fq \cdot awp(\%) \qquad (35)$$

In addition to the frequency of occurrence, co-occurrence frequency (frequency of occurrence of one cloud type given another cloud type) is computed. This variable symbolizes the dependence of one cloud from other clouds. The most important cloud combinations by observed frequency were also specified.

Trend of cloud amount is represented as the slope of a linear fit of mean annual cloud amount as function of year, with statistical significance computed with the modified Mann-Kendall Test (Hamed and Rao, 1998) at a significance level of 5 %. Trend value is reported as *%/ decade.* Special emphasis is made for diurnal cycle and it is analyzed in depth, computing phase and amplitude. The phase was computed as the hour of maximum cloud cover and the amplitude as the difference between maximum and mean cloud cover computed for each day. Also, mean diurnal cycles for every 15 days along the year were computed.

3.4. Radiative transfer model (*uvspec from LibRadtran*)

LibRadtran is a library containing programs and routines of radiative transfer in shortwave and longwave spectra. The radiative transfer program *uvspec,* in the shortwave spectrum, with 1-D configuration of LibRadtran version 2.0, was employed in this study to compute downward solar irradiance reaching the surface. The discrete ordinate method (*disort*) with 6 streams was selected as the radiative transfer solver of the program (Stamnes et al., 1988).

The *REPTRAN* band parameterization (Gasteiger et al., 2014) with spectral resolutions of 15 cm^{-1} was the adopted molecular absorption parameterization. Trace gases, pressure and temperature profiles from the standard tropical atmosphere (Anderson et al., 1986), where the atmosphere is divided in 50 levels from surface up to 120 km, were chosen. O_3 and NO_2 were modified from the initial profile by using monthly mean values of total column concentrations. O_3 total column concentration given in Dobson units (DU) was obtained from Total Ozone Mapping Spectrometer (TOMS) (McPeters et al., 1998) and downloaded from: https://ozoneaq.gsfc.nasa.gov/. NO_2 total concentrations in molec/cm^2 (Boersma et al., 2004) were obtained from ESA Scanning Imaging Absorption Spectrometer for Atmospheric Chartography (SCIAMACHY), at:

. These values are reported as output of AERONET products. For computing broadband irradiance, the solar spectrum at the top of atmosphere (TOA) of (Gueymard, 2004) with spectral resolution of 1 nm was used. For computing in narrow spectral range a better resolution of 0.1 nm from Kurucz (1994) was employed.

The spectral range selected for computing broadband irradiances is within the spectral range of the pyranometer (305 nm up to 2800 nm). In narrow bands, computations for MFRSR 345 were performed at 400.3 nm - 421.3 nm and for MFRSR 368 at 404.3 nm-424.2 nm. Spectral response function was taking into account for MFRSRs. Height above sea level was set up as 860 m because of height of top of *Pelletron* building. For instantaneous or specific cases, the day of the year and CSZA were also changed.

Column integrated water vapor included in the model was retrieved from *precipitable water vapor* given by AERONET from direct sun measurements at 940 nm. This variable was included for computing clear sky irradiances. The output of the model can be modified to irradiance units. The total transmittance is calculated using equation 19.

3.4.1. Surface albedo

Surface albedo in the spectral range 280 nm-4000 nm was interpolated using the relationship between the mean spectral surface albedos from AERONET at the site and spectral reflectance of different typical surfaces of the region, selected from the database of surfaces given by Baldridge et al. (2009), e. g. asphalts, trees, concrete and grass.

For each surface type, in wavelengths where albedo is not reported by AERONET, the ratio between surface reflectance at one wavelength and surface reflectance in the nearest wavelength from AERONET was calculated. Thus, using the mean of spectral surface albedos given by AERONET and the mean of surface ratios at any wavelength, albedo at wavelengths not given by AERONET were retrieved. The distribution of estimated mean spectral surface albedo is shown in Figure 3. The surface is considered as *lambertian* in the model.

3.4.2. Aerosols

Vertical profiles of aerosol particles were built using extinction coefficient computed from backscattering coefficient at 532 nm measured by ground-based Lidar. For each clear sky day, morning and afternoon mean profiles of extinction coefficient were normalized with respect to the mean AOD computed by integrating the extinction coefficient in the column, hereinafter called AOD_{lidar}.

Owing to values of extinction coefficient were retrieved only above 300 m, it was essential to know what fraction of total AOD was below 300 m. In order to compute the contribution of AOD below 300 m, mean AOD from sun-photometer ($AOD_{AERONET}$) in the same time interval of LIDAR was subtracted from the mean AOD_{lidar} as long as $AOD_{AERONET}$ was higher than AOD_{lidar}. Then, a mean ratio between AOD from the lowest layer of LIDAR relative to AOD below 300 m was calculated. AOD below 300 m was included in the mean profile using the former ratio.
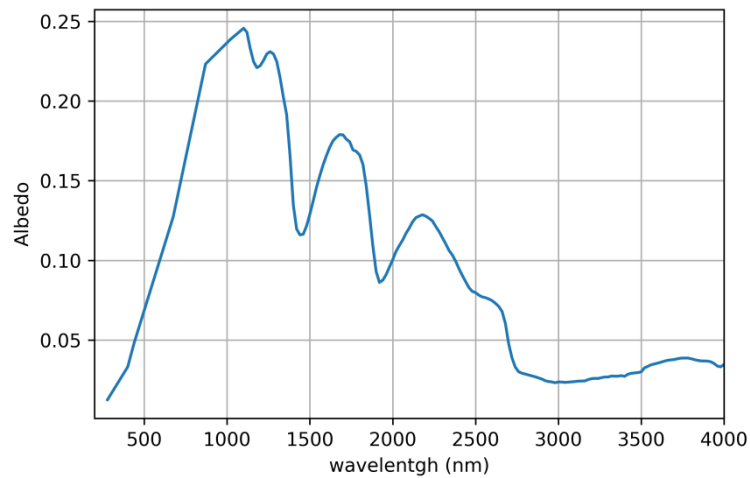
Figure 3: Mean spectral surface albedo used as input in the *uvspec* radiative transfer model.

Due to the lack of clear annual trend of stratospheric AOD in the last decade, a mean value of stratospheric AOD of 0.008 was taken into account in the computations (Vernier et al.,2011).

In figure 4.a, normalized extinction coefficient profiles from LIDAR, for each season and part of the day, are shown. Note the maximum near 300 m and the seasonal and diurnal differences. In the mornings, as expected,

aerosols are more concentrated near surface as compared to the afternoon, when loading of aerosol increases aloft. Remarkable increase is observed above 2 km due to the advection of biomass burning aerosols in spring (SON) (de Miranda et al., 2017). With the aim of including aerosols in the radiative transfer model, the normalized AOD profiles ($AOD_{NORM}(Z)$) below 8 km including AOD below 300 m were grouped in two seasons: typical: when profiles of the spring are not included, characterizing mean local contributions and spring (SON): mean profile for spring season, with advection of biomass burning plumes. Profiles were also classified as morning and afternoon.
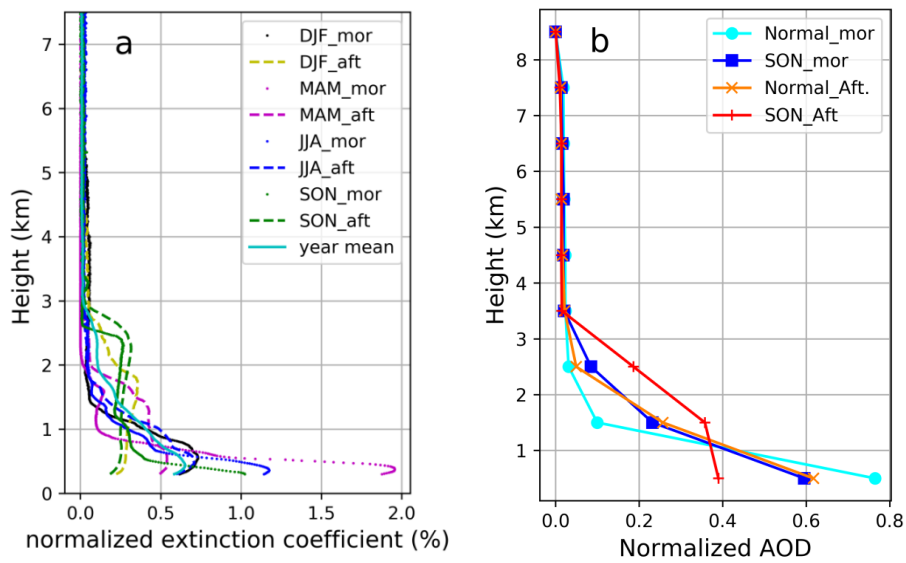
Figure 4: Mean profiles of normalized aerosol extinction coefficient for each season and time of the day (a) and the normalized profile of AOD built by synergy between LIDAR and sun-photometer for normal or typical conditions and for conditions with biomass burning plume advection in spring (SON) (b).

The spectral AOD profile included in the *uvspec* model was constructed using the profile of normalized AOD and values of AOD retrieved by AERONET (equation 36).

$$AOD\ (\lambda, Z) = AOD_{AERONET}(\lambda) \cdot AOD_{NORM}(Z) \qquad (36)$$

Narrowband irradiance around 415 nm was computed using AOD_{415}, estimated with AOD_{440} and the empirical formula of Ångström (equation 37), using the exponent (α) determined with the 380 nm and 440 nm AOD values retrieved by AERONET.

For broadband computations, AOD at 500 nm was employed and spectral dependence was included using the Ångström exponent α and Ångström's turbidity coefficient (β) (equation 37). This method has a good accuracy as reported by Serrano et al. (2014). SSA mean values of 0.85 and 0.90 were assumed (de Almeida Castanho et al., 2008), for local conditions and during spring time respectively.

$$AOD(\lambda) = \beta\lambda^{-\alpha} \tag{37}$$

Under cloudy conditions AOD is not retrieved by sun-photometry, therefore four methods for estimating AOD at MFRSR 415 nm channel and pyranometer were developed:

- Time interpolation of AOD throughout the day;
- Adjust climatological monthly diurnal cycle from at least one AOD retrieved on the same day;
- Adjust climatological monthly diurnal cycle of AOD from mean diurnal AOD computed as near as at least 2 days;
- Climatological monthly diurnal cycle of AOD.

Error in the estimation of AOD and contribution of error to COD retrieval by each method will be analyzed and discussed in section 4.3.2.1.

3.4.3. Clouds

Ice and liquid clouds were included in the model and assumed as homogenous layers. Cloud base and top, mean r_e and mean LWC/IWC are the input variables for clouds. These inputs were assumed from microphysical and geometric properties obtained from CALIPSO and CALIPSO-CloudSat as explained before. In table 2, the default configurations for each cloud type are summarized. Analysis of variability of cloud properties from satellite retrieval is carried out in section 4.1.

The parametrization used for liquid clouds is given by Hu and Stamnes (1993), where COD is obtained from r_e and LWC. They showed that the shape of the cloud droplet size distribution does not affect the results (r_e represents

well the drop size distribution of clouds). This parametrization is as accurate and faster in computation time than from Mie theory.

For ice clouds, the employed parametrization was from Key et al. (2002) where optical properties of seven shapes of ice particles (habits) are parametrized depending on r_e and IWC. According to the selected habit, differences can be as higher as 15 %, especially between *ice plate* and the other habits. The habit selected is the *Rough Aggregated as* an example of 3D ice. In section 4.1 the selection of this habit is discussed.

Table 2: Default cloud configuration assumed in the radiative transfer code.

Cloud	Top (km)	Base (km)	r_e (µm)	LWC/IWC (g/m^3)
Ice	10.05	9.09	51.2	0.01
Liq.	1.60	0.86	11.6	0.23

3.5. Methodology of the radiative computations and COD retrieval.

In the figure 5 the flow chart of the procedures for the retrieval of COD and radiative effects computations are shown. The main datasets are the global irradiance measured by the pyranometer and spectral diffuse and direct irradiances at 415 nm and 870 nm measured by the MFRSR. Three steps before the direct computations with LibRadtran are carried out. First, the 1 min instantaneous calibrated measurements of MFRSR and Pyranometer are time-collocated with precipitable water vapor and AOD from sun-photometer. The second step is the definition of cloud scenarios by the **Sky Definition** method, detailed in the next section. After the measurements are filtered, the mean aerosol profiles according to the season and hour, in combination with the coincident AOD from sun-photometer, are used as input in the radiative transfer model. In addition, the mean microphysical properties retrieved from the combination of CALIPSO-CloudSat, for ice and liquid clouds are inputted to the model used in the retrieval of ECOD.
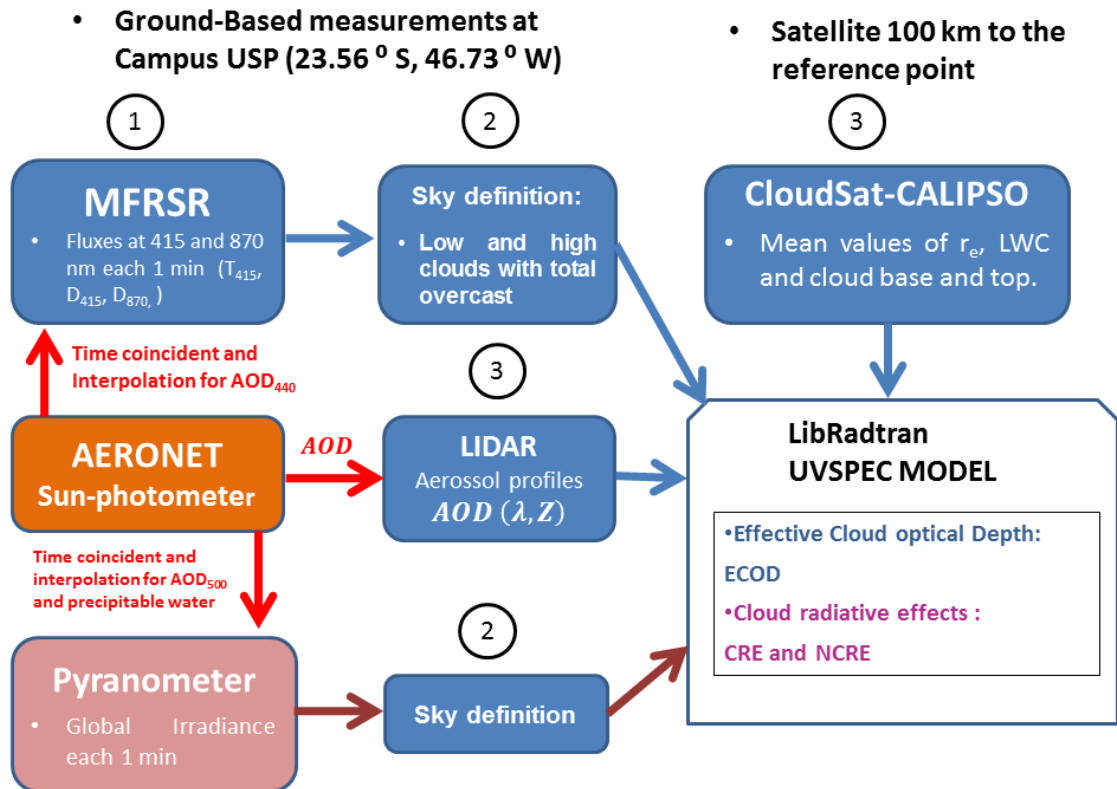
Figure 5: Flow chart of the main procedures carried out for the ECOD retrieval and computations of cloud radiative effects.

3.5.1. Sky definition

Ancillary information concerning cloud presence and obstruction of solar disk are needed to classify the measurements made by pyranometer or MFRSR. Because the time period of all sky-camera is limited (started in September 2016), before this date, algorithms to define the presence of clouds were required. Therefore three algorithms were developed for applying in absence of sky camera observations: using visual observations of clouds, spectral ratio of diffuse irradiance. In addition, algorithm of obstruction of solar disk by clouds was defined. If the three algorithms were coincident, the instantaneous measurements were classified. In the following the three algorithms are detailed.

3.5.1.1. Sky definition by visual observations

Time coincidence with visual observations in a time window of 20 minutes before and after the time of observation was a criterion selected to

classify the sky by visual observations above the measurement site. Despite the distance from the site is about 15 km in a straight line to the meteorological station where visual observations are made, we considered that the spatial variability in clouds between the two sites were not as high as to make significant differences in cases when clear sky or total cloud cover were reported.

Comparing with observations from the sky camera, with 6868 cases of total overcast conditions, 99.68 % of coincidence was found with visual observations from the meteorological station, when cloud cover greater or equal 9 tenths was observed. Below 8 tenths, a 100 % of coincidence were noted. Thus, visual observation can be a useful ancillary data in dates when sky camera observation was not available. For clear sky conditions, more than 95 % of data observed as clear sky by the sky camera were reported also at the meteorological station.

Classification of sky from visual observations is as follows:

- Clear sky, if the maximum of cloud cover is 20 % with no presence of high clouds.
- Low/mid/high cloud partially overcast: only low/mid/high clouds with cloud cover below 70 %.
- Low/mid/high clouds total overcast: only low/mid/high clouds with cloud cover of 100 %.

3.5.1.2. Direct sun criterion (solar disk obstruction)

In addition to cloud cover, information about obstruction of solar disk is needed. With MFRSR measurements direct sun irradiance can be derived. Then, comparisons of T_{dir} modeled for clear solar disk by *uvspec* and measured T_{dir} at 415 nm were also used to classify the conditions of the solar disk. Min, (2004) screened clouds by using direct sun irradiance when thin clouds were present by applying threshold of Ångström exponent for aerosols. But it is only limited to thin clouds and needs to compute spectral AOD with MFRSR which is beyond the scope of this research.

The solar disk was considered **obstructed** by cirrus clouds when modeled T_{dir} was 15% higher than the T_{dir} measured, otherwise it was considered as a clear disk. This threshold was selected after the analysis of *uvspec* error in computing T_{dir} at 415 nm for clear sky conditions (section 4.3.3).

The 15 % difference criterion works better for cirrus clouds with lower COD values, but in the case of low clouds, with the presence of interstices, it is not robust. Therefore to avoid misclassification in low clouds conditions, differences between T_{dir} modeled for clear sun disk and T_{dir} measured must be higher than 200 %. For mid-level clouds, 20 % of difference was considered. These thresholds were stablished analyzing cases observed by the sky camera.

3.5.1.3. Spectral diffuse ratio (DR)

The presence of clouds can modify the spectral distribution of diffuse radiance relative to ones of clear sky. The physical reason is that cloud drops are larger than molecules and aerosols; therefore they present lower spectral dependence in the solar extinction, i. e., compared to aerosols and molecules. Thus a ratio between diffuse irradiance at 870 nm and 415 nm hereinafter diffuse ratio (DR) can be a good indicator of the presence of clouds.

This ratio is based on the method applied by (Min et al., 2008) using the diffuse transmittance to compute cloud fraction. Furthermore, LeBlanc et al. (2015) employed the spectral ratio of radiance at zenith at 870 nm and 600 nm measured at the surface. They showed the high sensitivity of the ratio at lower CODs.

In figure 6, the variation of DR with CSZA, COD for cloudy and AOD_{500} for clear sky is evaluated using 1-D *uvspec* model. AOD_{500} was varied between 0.08 and 0.8. Between 0.08 and 0.3 the step was 0.03, while above 0.3 it was equal to 0.1. COD for ice clouds spans from 0.03 up to 4, with steps of 0.5, and for liquid clouds, it varied between 3 and 100, with steps of 5.As it can be observed in the figure 6, DR varies between cloudy and clear skies. Below AOD_{500} of 0.3, clear sky can be distinguished from sub visual cirrus with COD of 0.03. When single scattering dominates over multiple scattering, the sensitivity with CSZA is observed. That can be noted for clear sky and for low COD of ice

clouds. When multiple scattering dominates DR is less sensitive to CSZA (low clouds and higher COD of ice clouds). From the behavior observed for low clouds is possible to clearly identify them over the clear sky cases. But differences between ice and liquid clouds are not so obvious for thick cirrus clouds.
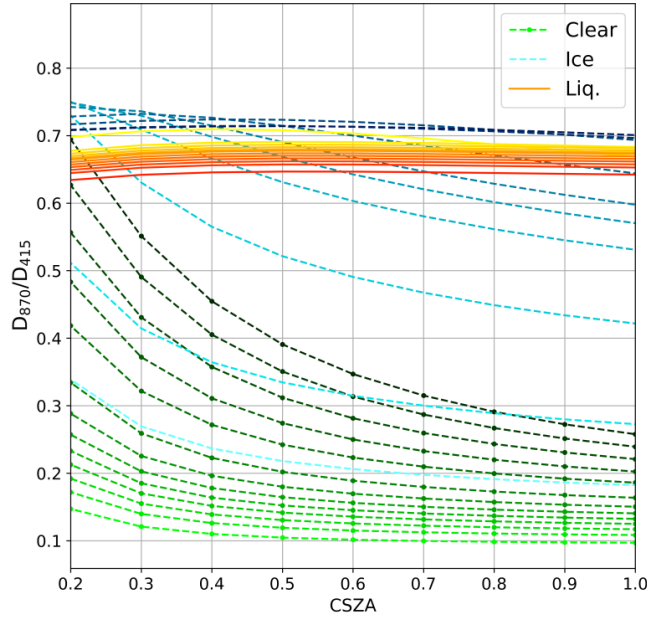
Figure 6: Variations of diffuse ratio, at channels 870 nm and 415 nm, at surface level, with CSZA and AOD for clear sky, and COD of ice and liquid clouds computed from 1-D uvspec model of LibRadtran. The darker the color the higher the value of AOD_{500} or COD. COD for ice clouds spans from 0.03 up to 4 and, for liquid clouds, it varies between 3 and 100. AOD_{500} is varied between 0.08 and 0.8. Between 0.08 and 0.3 the step is 0.03, while above 0.3 is 0.1.

From the aforementioned analysis of DR, it is possible to make a criterion to define clear and overcast sky, using spectral measurements of diffuse irradiance from MFRSR. Therefore, after validation using real measurements (section 4.3.4), the following criteria are used to define cloudy and clear sky:

- Clear sky (**clear**) is defined when AOD_{500} is below 0.30, because above 0.30 can be overlapped with subvisual cirrus. Therefore depending on CSZA for AOD below 0.3 clear sky cases can be defined by the expression given in the equation 38.

$$DR < 2.8 \cdot 10^{-2} \cdot CSZA^{-2} - 0.11 \cdot CSZA + 0.25 \qquad (38)$$

- Total overcast sky, with high/mid-level clouds (**mid or high overcast**), is defined by the equation 39, where coefficients a, b and c depend on AOD_{500}, to avoid overlap with possible clear sky.

$$DR > a \cdot CSZA^{-2} + b \cdot CSZA + c \qquad (39)$$

- Total overcast sky with low cloud, mid or high clouds (***low, mid or high overcast***) is classified if DR is above 0.6.

After the coincidence between the three methods (in the Sky definition), before September 2016, 110727 cases for MFRSR 368 were classified according to cloud scenarios shown in table 3. A total of 59592 of total overcast sky cases, including low and high clouds, were employed to retrieve ECOD. For pyranometer measurements, 26853 cases were classified.

In Table 3, a resume of sky definition algorithms to define cloud scenario are shown. For the ECOD retrieval, cloud scenarios LW_0 and H_0 were employed. For cloud radiative effects all the scenarios were used. Note, that after September of 2016 only definition of visual observation from sky camera pictures and direct sun criterion are employed.

Table 3: Sky definition algorithm for the clouds scenarios defined in this research.

Sky definition			Cloud scenario
Visual	**Direct sun**	**DR**	
Low clouds total overcast	obstructed	Low overcast	LW_0
Low clouds partially overcast	obstructed	Not clear	LWBK_0
Low clouds partially overcast	clear	Not clear	LWBK_1
High clouds total overcast	obstructed	High overcast	H_0
High clouds partially overcast	obstructed	Not clear	HBK_0
High clouds partially overcast	clear	Not clear	HBK_1
Mid clouds total overcast	obstructed	Mid overcast	MID_0
Mid clouds partially overcast	clear	Not clear	MIDBK_1

3.5.2. Calibration of MFRSR 368

Transmittance from MFRSR 368 at 415 nm is the main input variable to be used for retrieving the effective cloud optical depth. This instrument was calibrated using indirect calibration (Holben et al., 1998). The idea is to transfer the calibration of MFRSR 345 to MFRSR 368 using coincident measurements under clear sky conditions. Cases of clear sky were selected from sky camera after September of 2016. An inverse method from Lambert-Beer equation was

applied, using the AOD at 415 nm computed from MFRSR 345. Retrieval of AOD_{415} from MFRSR was carried out by the same method applied by Sayão, (2008).

The aim of the calibration procedure is to obtain the equivalent solar irradiance at 1 astronomical unit (AU) (SS_0) at TOA (equation 40). Where SS_s is the direct sun irradiance measured at surface, k is the correction factor of Earth-Sun distance, m is the relative optical air mass for Rayleigh scattering, MOD and NOD are the molecular optical depth due to Rayleigh scattering and nitrogen dioxide, respectively. $AOD_{415}{}^{345}$ is the aerosol optical depth at 415 nm retrieved from MFRSR 345.

$$SS_0 = k^{-1} SS_s \exp\left[m\left(AOD_{415}{}^{345} + MOD + NOD\right)\right] \quad\quad (40)$$

For every 1 min of clear sky data, SS_0 was retrieved and time interpolations were made for measurements with no clear sky conditions. For cases when time interpolation was impossible to make, the nearest neighbor interpolation was carried out. After calibration, T was computed using equation 18.

3.5.3. The retrieval of effective cloud optical depth

Since cloud optical depth was obtained from hemispherical measurements under total overcast conditions, the term Effective Cloud Optical Depth (ECOD) can be adopted. The retrieval of ECOD was carried out by inversion method using T_t at 415 nm computed from measurements of MFRSR 368. Transmittance was selected because errors associated to the calibration accuracy were reduced. At around 415 nm, surface albedo is low, thus multiple scattering between surface and cloud base is minimized. In addition, at this wavelength there is only weak NO_2 absorption and O_3 absorption is negligible. Furthermore, there is no spectral variability of COD at these wavelengths (Min and Harrison, 1996). As the retrieval was applied for total overcast conditions, and the model did not allow the inclusion of clouds with mixed phase, the retrieval method was applied for either low (warm phase) or high clouds (ice phase).

Visual observation with sky camera helped classifying total overcast cases after September of 2016. Before this date, the sky definition criterion (section 3.5.1) was applied. Cases under precipitation were discarded using the report of precipitation made at the meteorological station.

Based on the method applied by Salgueiro et al. (2016), but including the aerosol effect, lookup-tables (LT) for each cloud type (ice or liquid) were built using the 1-D *uvspec* where output is T_{415}. The input variables of each LT are: CSZA, AOD_{415}, COD and aerosol profile. The aerosol profile (figure 4.b) was selected depending on season and time of the day. The sensitive study is carried out in section 4.3.1, and the selection of input variables is discussed.

The procedure to retrieve COD is discussed as follows:

First, the aerosol profile is selected, afterward 2D cubic interpolation of T_{415} depending on CSZA and AOD_{415} for each COD step is carried out, i.e. T_{415} =f(AOD_{415}, CSZA). Therefore, T_{415} is estimated from the measured AOD_{415} and CSZA for every COD step. Subsequently, linear interpolation of estimated T_{415} as function of COD is computed. Using the linear interpolation, ECOD is retrieved as the minimum difference between T_{415} estimated and T_{415} measured by iteration along the COD values.

In the configurations of each LT, AOD_{415} varied between 0 and 1.5 and CSZA between 0.1 and 1 with steps of 0.05. For liquid clouds, COD varied from 0 up to 400 with step of 1. In the case of ice clouds, COD varied from 0 up to 40, with steps between 0 and 4 of 0.25 and 1 above 4.

3.5.3.1. Error in COD retrieval

The error propagation for COD retrieval is expressed in equation 41, as the root square of the sum of error squared of each variable *i*. The relative error is computed as the ratio of each error and the COD value retrieved.

$$\delta COD = \left[\Sigma_i \left(\frac{\partial COD}{\partial i} \delta i \right)^2 \right]^{\frac{1}{2}} \tag{41}$$

Applying the methodology proposed by Serrano et al. (2014) (equations 42-44) the contribution of each variable to the COD error is retrieved. The

variation of *T* due to the error of variable *i* assuming the other variables constant is δT_i. In addition, the variation of *T* due to the possible error induced in COD (δCOD_i) is δT_{cod}. Differences between δT_i and δT_{cod} are computed by iteration of δCOD_i. When the difference between δT_i and δT_{cod} is the minimum, δCOD_i is obtained. The computation of *T* is carried out using the *uvspec* considering CSZA equal 0.86.

$$\frac{\partial COD}{\partial i} \delta i \approx \delta COD_i \tag{42}$$

$$\delta T_i = \frac{1}{2} |T(i + \delta i, COD) - T(i - \delta i, COD)| \tag{43}$$

$$\delta T_{cod} = \frac{1}{2} |T(i, COD + \delta COD_i) - T(i, COD - \delta COD_i)| \tag{44}$$

Because of the transmittance error is directly related to the error associated to the calibration procedure, 2 % of error is assumed. For single scattering albedo, the error of retrieval from sun-photometer is about 0.05 (Dubovik et al., 2000), since the error decreases to 0.03 for AOD_{440} above 0.20 and around 0.05-0.07 for AOD below 0.20. SSA mean values of 0.85 and 0.90 were assumed (de Almeida Castanho et al., 2008), for local conditions and during spring time, when biomass burning plumes are transported to the city, respectively. The error of assuming mean value of SSA is the standard deviation of SSA obtained from sun-photometer at the site. Therefore the total error of SSA (δSSA), including the error of the retrieval is 0.19.

For AOD, the error assumed is the sum of error of AOD measurement (0.02) (Serrano et al., 2014) and the maximum error of inferring AOD, from mean monthly diurnal cycle at 415 nm (0.11) (Table 6). The standard deviation of samples of cloud properties was assumed as the cloud properties errors. For ice clouds error of r_e (δr_e) is about 40 μm and for low clouds, 2 μm. For cloud base error (δCB) it is computed as 2.8 km and 2.7 km for ice and liquid clouds, respectively. The results of error propagation are presented in section 4.3.2.

3.5.4. Instantaneous cloud effects on solar radiation

The instantaneous cloud effect on solar radiation was evaluated by CRE and NCRE (equations 26 and 29 of chapter 2). Irradiances measured every 1

min from pyranometer were selected as cloudy conditions, while irradiance for clear sky was estimated using *uvspec* model.

Default configuration, explained in the topic 3.4, was used to calculate irradiance under clear sky conditions. As will be discussed in the next chapter (Results), in general, the model overestimated clear sky irradiances compared to the measurements. The maximum relative difference of 15% and 5 % was observed for overestimation and underestimation, respectively. To avoid erroneous estimation of the cloud effect on solar radiation, when the relative difference between modeled and measured irradiance was higher than – 5 % and less than 15 %, the case was discarded.

For solar disk blocked by clouds, the following cases (according to table 3) were analyzed: completely or total overcast sky with low clouds (*LW_0*), partially overcast with low clouds (*LWBK_0*), total overcast sky due to high clouds (*H_0*), partially overcast sky with high clouds (*HBK_0*) and total overcast sky due to mid clouds (*MID_0*). When the solar disk was clear, the following cases were computed: low clouds (*LWBK_1*), high clouds (*HBK_1)* and mid clouds (*MIDBK_1*).

4. Results

4.1. Cloud characteristics from CALIPSO-CloudSat

Seasonal profiles of frequency of occurrence of clouds for nighttime (01:00 LT) and afternoon (14:00 LT) overpasses are shown in figure 7. There were more than of 2000 profiles measured at night and more than 7000 measured in daytime for each season. Seasonal and day/night differences are clearly observed.
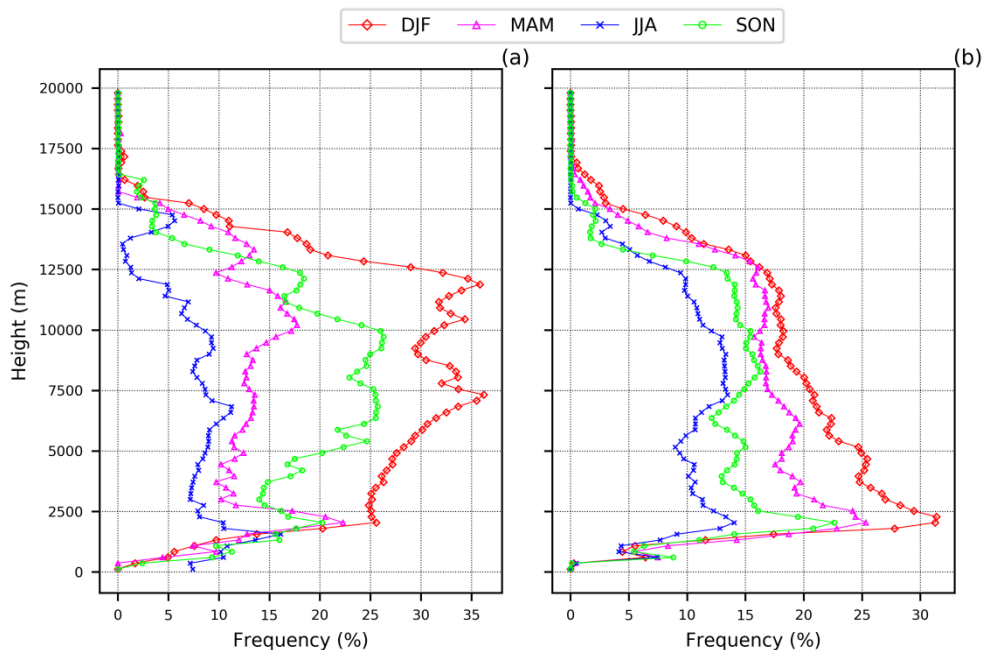
Figure 7: Profiles of frequency of occurrence of clouds per season at nighttime (a) and daytime (b), computed from cloud mask generated by merged CALIPSO-CloudSat data.

Higher frequencies of clouds were observed in summer, whose vertical development could reach 17 km. In winter, lower frequencies were found and clouds could reach 15 km. The contrast between daytime and nighttime profiles is observed. In daytime profiles the maximum frequency, around 30 %, takes place near 2500 m in summer. As a consequence of the diurnal heating, cloud frequency increased at lower layers during daytime. At night, cloud frequency decreased a little below 2 km, and increased at mid (7.5 km) and high layers (12 km) with 35 % of frequency in summer, as a consequence of the remaining convective activity in the afternoon. At night, convection tends to disappear and the water vapor supply from surface decreases, low clouds begin to evaporate until radiative cooling starts the formation of stratiform low clouds (Wood, 2012).

In mid and high layers, clouds remain due to the weak circulation and the radiative cooling which maintains or increases the clouds.

At daytime, from summer to winter, the decrease of cloud frequency is observed more pronounced at lower layers from about 32 % to 14 %. At nighttime higher differences are found in higher layers from 35 % to 5 %. In winter, the maximum frequency is observed in lower layers with 15 % at nighttime and minimum in higher layers. This maximum in lower layers at nighttime is a consequence of the increase of radiative cooling.

In the figure 8, profiles of cloud frequency as function of the distance from the coast are presented. In the computations, measurements at nighttime and daytime were used together. Variability is also observed as the distance from the coast line increases.
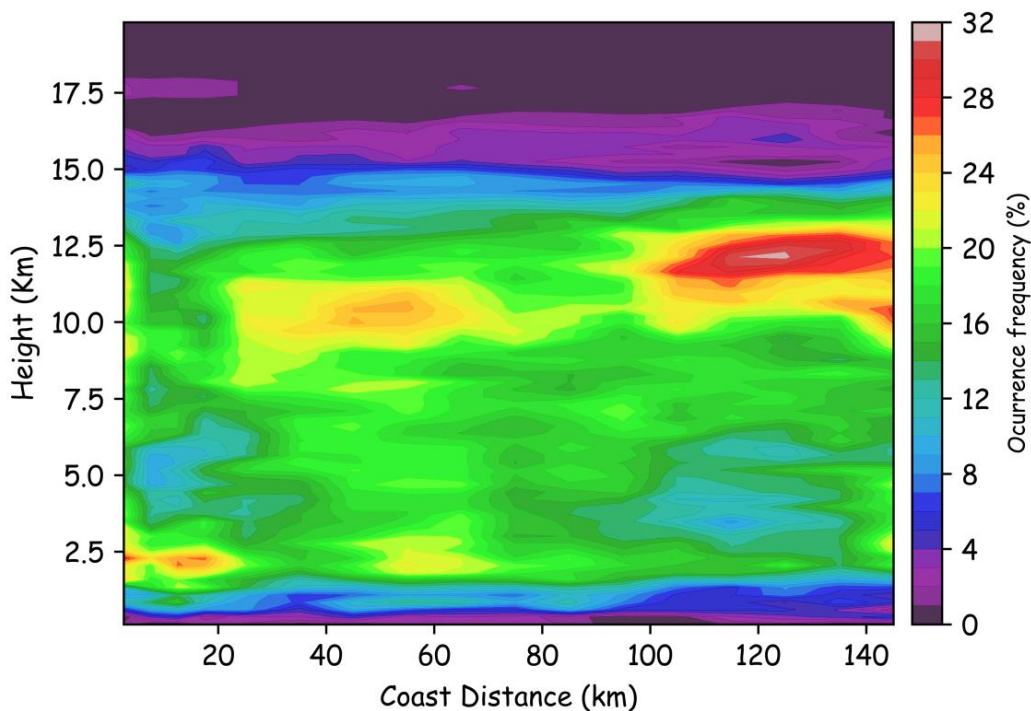
Figure 8: Frequency of presence of clouds relative to the distance from the coast line.

Note near the coast up to 20 km the convection activity is expected to be less strong compared to inland. With a distance below 20 km far from the coast line, the maximum frequency at lower layers (2.5 km a.s.l) with 26 % is observed. From the edge of Serra do Mar mountain barrier (from 20 km) an increase of cloudiness in mid and high layers is observed with maximum

frequency near 50 km from the coast, with 24 % frequency of occurrence near 10 km of height.

While the distance to the coast increased, low clouds frequency begin to decrease and an increase of the height of clouds and frequency is observed. Maximum of cloud frequency was found 100 km away from the coast and near 12 km height with 32 %. Undoubtedly, this behavior illustrates that convective clouds are more frequent inland.

Geometrical properties, cloud base height and cloud thickness for ice and liquid clouds for each season are shown in figure 9. Moreover, the number of identified clouds is also shown above of each boxplots. In the case of cloud base of warm clouds a slight variability is observed, with similar values for the median in all seasons, but, in winter, heights of cloud base are more concentrated around the median with the smallest interquartile range. However, hypothesis test of *Kruskal-Wallis* (Kruskal and Wallis, 1952) does not show differences between seasonal samples. Cloud base of liquid clouds at the region presents the median value of 860 m.
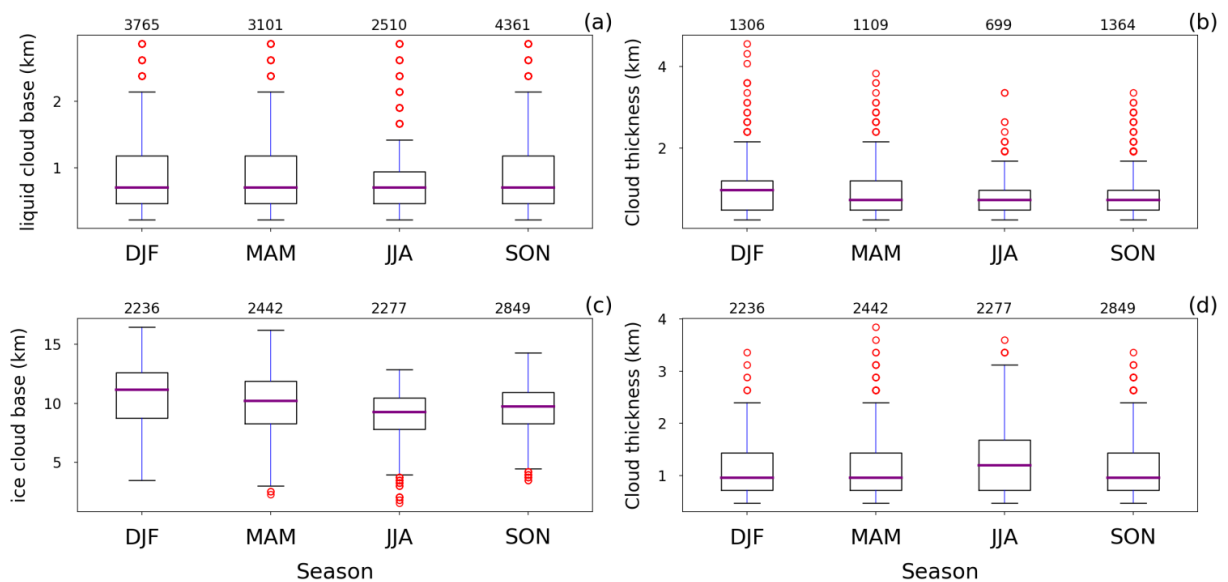
Figure 9: Seasonal variations of geometrical properties of clouds: the height of base and thickness of liquid clouds (a, b) and ice clouds (c, d). The number of clouds identified is also shown in the upper border of each figure.

As expected, in summer, warm clouds are deeper with median of 900 m. In winter and spring, the median of cloud thickness is around 600 m. For ice clouds differences are larger, cloud base is higher in summer with a median of

11 km, and lower in winter (9.5 km). According to *Kruskal-Wallis H-test*, differences are statistically significant. The thicker of ice clouds in winter, probably has to do with the lower cloud base.

The seasonal variability of microphysical properties for ice and liquid clouds is shown in figure 10. Liquid clouds show small sizes as compared to ice clouds. Seasonal differences with statistical significance between r_e of liquid clouds r_e confirmed by the *Kruskal-Wallis H-test*. The highest value of the median occurs in winter with 11.8 µm, because in this season clouds are more frequently originated from interaction of cold air mass outbreaks and sea, as a result of cold migratory anticyclone systems.
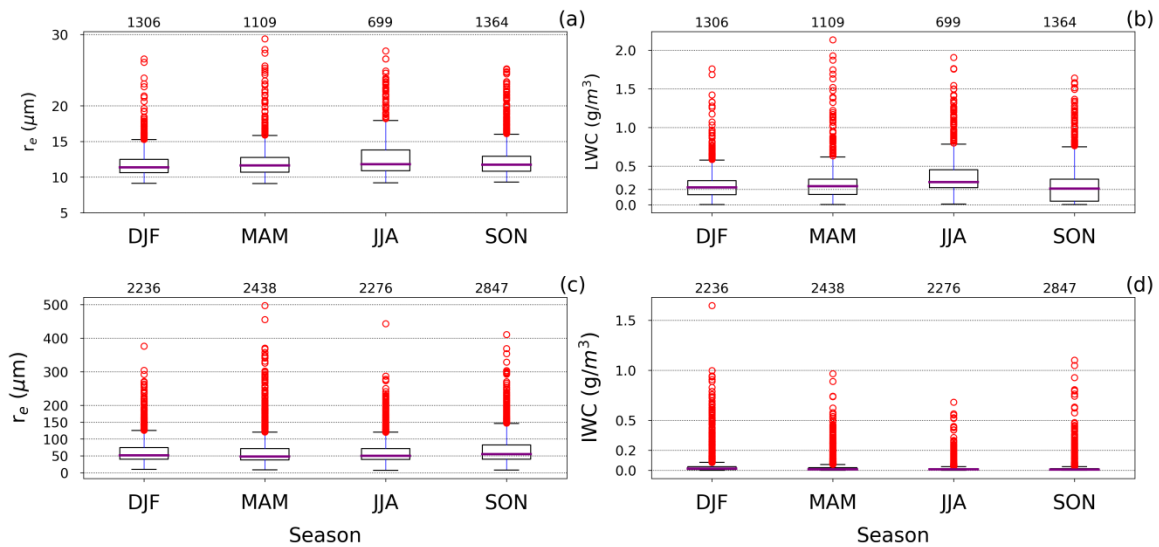
Figure 10: Microphysics properties re and LWC or IWC for liquid (a, b) and ice clouds (c, d). For liquid clouds, the products of CloudSat are employed and for ice cloud, CSCA-Micro product was considered. The number of cases is placed in the upper border of each figure.

Similar to r_e, *LWC* has differences with the highest median in winter, but with the minimum observed in spring. For ice clouds, the seasonal differences are smaller with many outliers for effective radius, above 200 µm, while the median values are around 51 µm. The general median value, considering all data available, is equal 51.23 µm. IWC also presented many outliers with values higher than 0.5 g /m^3, with some values comparable to the maximum LWC observed for low clouds, although the median presented little seasonal differences with values around 0.01 g /m^3.

To try to know the more frequent particle habit in the region, the product of JAXA *CA-Ctype* for cloud particles was used. The frequency of occurrence of cloud particle habit per height level for each season is presented in figure 11.

Three types of habit were analyzed: 3D-ice (3dic), 2D-plate (2dpl) and mixture of 3D-ice and 2D-plate (mx3i2p). The predominance of three dimensional ices is observed specially above 10 km where almost 100 % of ice cloud layers are composed of it. In addition, 2D-plate habit is more frequent in mid-levels particularly between 6 and 8 km with higher frequency in autumn and winter probably due to the weaker updrafts (Heymsfield et al., 2017) as compared to summer and spring. At 4 km to 8 km there is higher variability of *habit* being impossible to define a fixed classification.
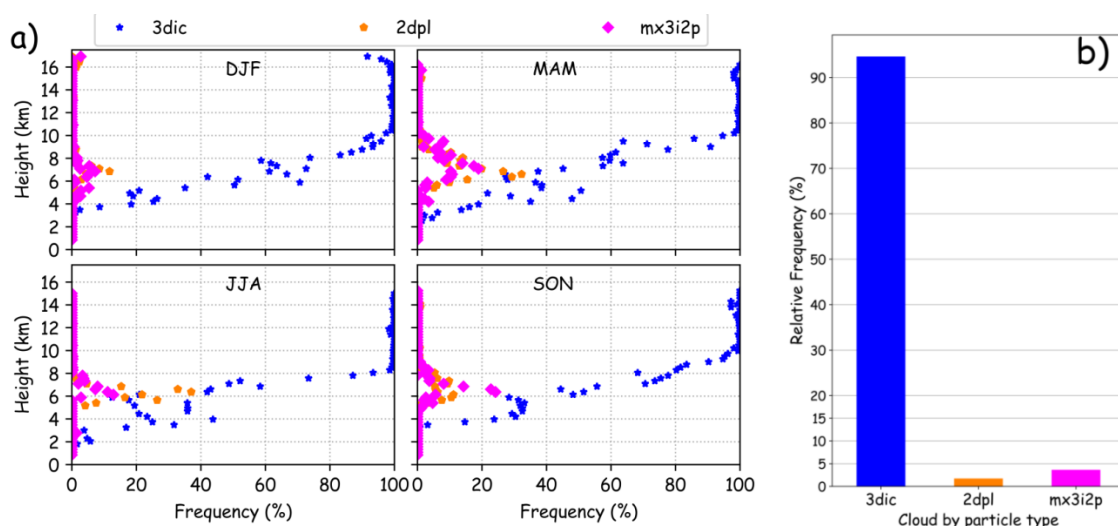
Figure 11: Profiles of frequency of occurrence of ice cloud habit for each season (a) and frequency of occurrence of cloud layer totally composed by a given cloud particle habit.

The frequency of occurrence of cloud habit is presented in figure 11 b. In the region, clouds are predominantly composed by 3D ice particles with 95 % of frequency, followed by the mixture of 3D with 2D plates with 4 % frequency and, in the case of only 2D plates; they were identified in 1 % of data only. After this analysis, the type of habit chosen as input in the *uvspec* of *LibRadtran* code for ice clouds was the one with 3D geometry (as example 'Rough Aggregated').

Variations of microphysics properties inside the ice clouds respect to the height above the cloud base are shown in figure 12.a-b. Median values and interquartile ranges are presented. As it can be seen, ice clouds are far from and idealized homogenous cloud. The decrease of cloud particle sizes and ice

water content is observed with the height above cloud base. The r_e can decrease from 60 μm up to 40 μm near cloud top. But for IWC the reduction is higher from near 10 mg m^{-3} until 2 mg m^{-3} near the top of cloud. This pattern is a response to the decrease of water vapor availability as the temperature decreases with the height.

Variations of mean microphysical properties of all cases of clouds respect the height of cloud base are shown in figures 12 c-d. Mean r_e decreases as cloud base is higher from 6 km (102 μm) up to 12 km (40 μm). However, near 13.5 km a slight increase is observed. For IWC this behavior is also observed with a higher increase near 13.5 km which can be attributed to cirrus from remaining storms.
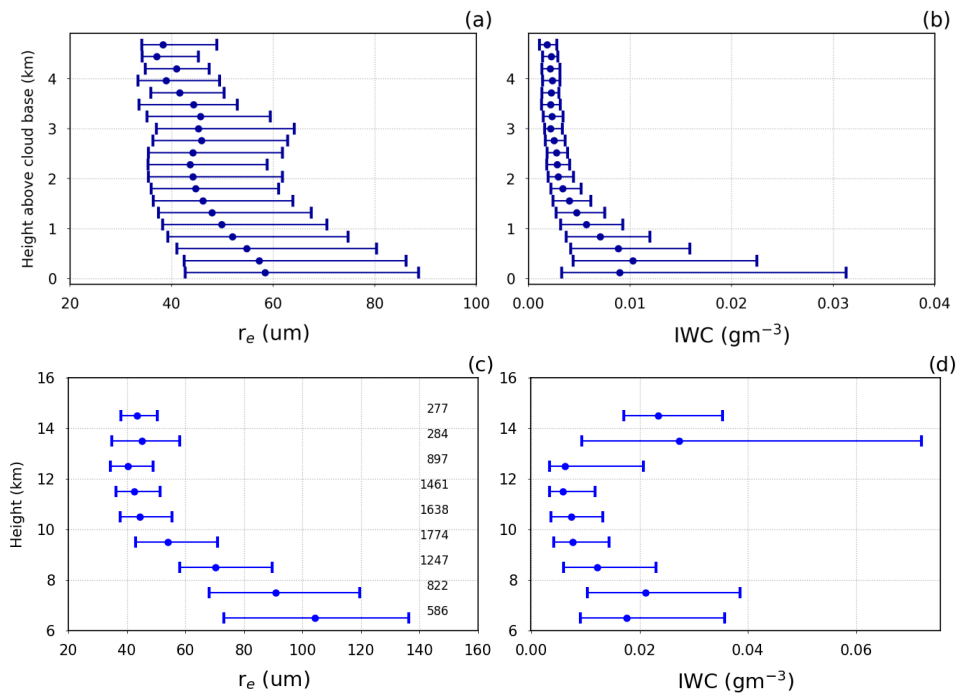
Figure 12: Variations of re and IWC with height above cloud base (a, b) and variations of mean re and IWC of the cloud layer according to the height of cloud base (c,d).

4.2. Cloud climatology from visual observations[3]

4.2.1. Diurnal and annual cycles of cloud amount

---

[3] *This section is part of Results of the paper submitted to the International Journal of Climatology, ID=JOC-18-0083, for possible publication.*

Figure 13.a shows the mean diurnal cycle and respective variability of clouds amount from visual observations. Figure 13.b-c gives indication of the associated annual variability, i.e. how the hour of maximum and amplitude of diurnal cycle vary along the year.
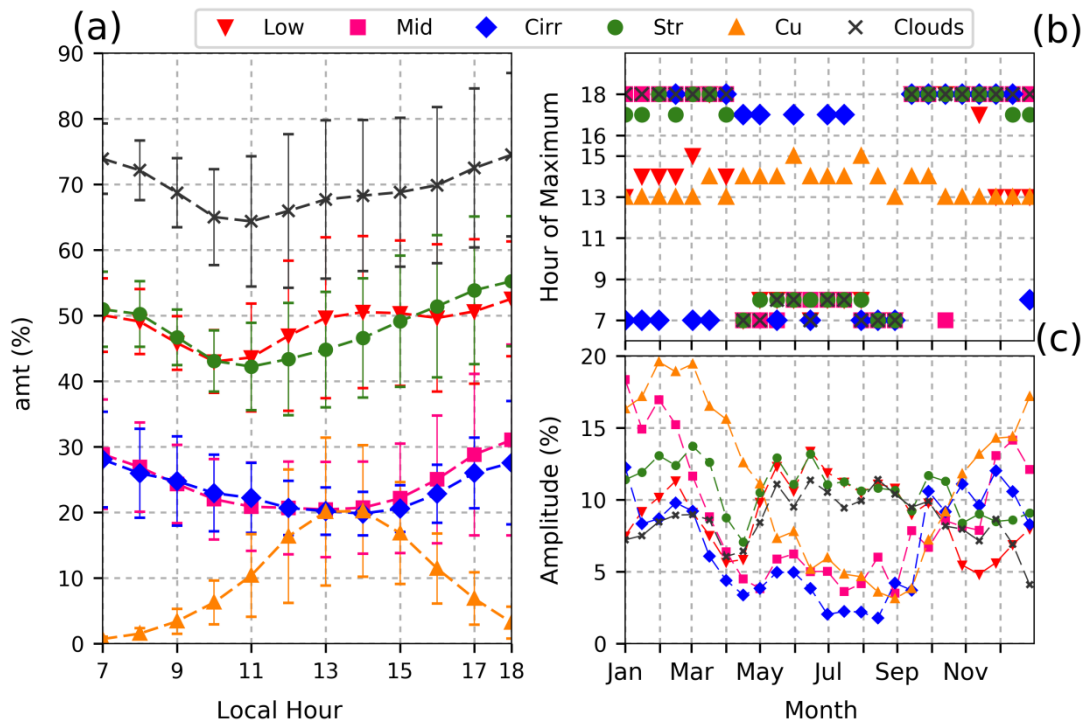
Figure 13: Mean diurnal cycle and standard deviation (a) computed from mean diurnal cycles calculated for every 15 days. Variability of the diurnal cycle for every 15 days computed as hour of maximum (b) and Amplitude (c).

The mean total cloud amount (**clouds**) decreases after sunrise until about 11:00 LT (63 %), with a monotonically increase with the advance of the day up to a maximum at sunset (74 %). This behavior is initially associated with the possible increase of cloud amount in the end of the night, due to radiative cooling. After sunrise, the radiative cooling is surpassed by solar heating, breaking the inversion layer above cloud, and dissipating the cloud layer. The posterior increase after 11:00 LT is due to convective development caused by the solar heating, influence of the sea breeze or a synoptic system. If convection is deep, formation of high and mid-level clouds are possible. High or mid-level clouds, formed by convection, remain or increase in cloud amount at night driven by radiative cooling (Heymsfield et al., 2017). Hence, mid and high clouds present an inverse diurnal cycle of cloud amount as compared to solar heating diurnal cycle (figure 13.a.).

This diurnal cycle of clouds is variable along the year (Figure 13.b-c), with the maximum observed at sunset from September to March and around sunrise from April to August. The decrease observed near sunrise (Figure 13.a) takes longer in wintertime and lasts two hours more (until about noon) compared to summer (not shown in figure). Undoubtedly, differences along the year were due to differences of driven mechanism of cloud formation. In winter, radiative cooling dominates, there is less deep convection and air humidity is reduced, whereas in summer, deep convection is more frequent.

Low clouds drive the diurnal cycle of ***clouds*** as can be observed by the similarity in their cycles. Low clouds has a significant influence of low stratiform clouds, since they are the more abundant type of clouds in the location, and only a pronounced increase in the diurnal cycle at noon and a slightly decrease near 16:00 LT are due to cumuliform clouds.

Note the differences between low stratiform and cumulus clouds. *Stratiform* clouds are less influenced by the solar cycle, rather the radiative cooling effect is responsible for the formation at night and sunrise (Wood, 2012). When isolating *low stratiform* clouds (not shown), it is possible to observe that the maximum cloud amount occurs for stratus clouds at sunrise and for stratocumulus at sunset, thus, from Figure 13.b, maximum of diurnal cycle probably can be influenced because stratus prevails in winter, while stratocumulus dominates during the summer season. It is important to observe that other mechanisms can lead to the formation of stratiform clouds, not only radiative cooling, particularly in summer and spring, as will be discussed later. This behavior was not observed when analyzing the synoptic reports (Eastman and Warren, 2014) because of the underestimation of Sc when they are present with Cb. Moreover in the region, there can be an important contribution of cumulonimbus clouds by the possible influence of the sea breeze circulation, synoptic systems as SACZ and cold fronts. The amplitude of *stratiform* clouds was less variable along the year with maximum in autumn-winter (Figure 13.c), and minimum in April. In this month, the increase of cloud amount at sunset is less pronounced and the radiative cooling at sunrise is negligible, producing lower amplitude in the diurnal cycle. In addition, in this month, cold fronts are highly frequent (Morais et al., 2010).

61

Cumulus clouds, by contrast, present high dependence on the solar heating diurnal cycle, with maximum near noon, throughout the year (Figure 13.b). Furthermore, this maximum occurs two hours later in winter compared to summer. That is because, in winter, the maximum of cloud cover is found at sunrise leading to delaying of surface heating by solar radiation, thus, the increase of cloud amount by convection can start only in the afternoon. Note the differences in amplitude of cumulus along the year, with the highest amplitude in summer of about 15 % and minimum in winter, near 5 %.

The maximum amplitude, above 15 %, is also observed in summer for *mid-level* clouds. *Mid* and *cirriform* clouds show comparable characteristics with maximum in spring-summer at sunset, except on the first 15 days of October when the maximum is observed at 7:00 LT. In autumn-winter, one observes a maximum of *mid clouds* at sunrise but, for cirrus, the maximum can take place near sunset. Note that, for cirrus, from January to March, the maximum is observed in the morning.
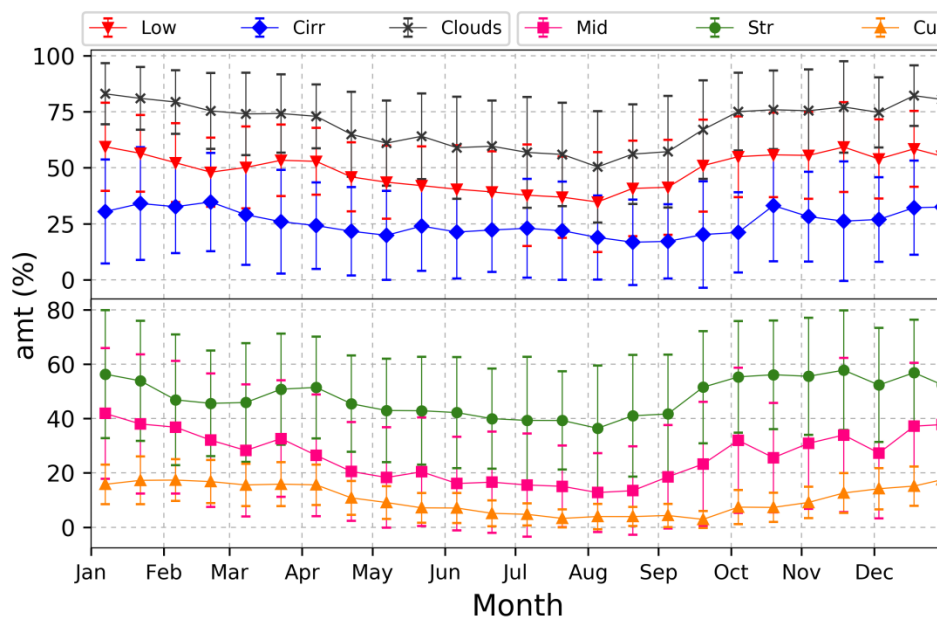
Figure 14: Mean annual cycle computed for every 15 days. The vertical bars represent the inter-annual variability.

The annual cycle, computed every 15 days, is shown in Figure 14. Mean values and standard deviation are presented. Observe the seasonal variability for total cloud cover (**clouds**) with a minimum in early August. Maximum takes place in summertime, between December and January. Low clouds show

minimum in the first part of August but, in contrast to total cloud cover, an increase is observed between March and April due to the same increase detected in this period for *stratiform* clouds. As mentioned before, the peak of cold front systems crossing the region, as diagnosed by Morais et al. (2010), can contribute to this increase.

Cirriform clouds presented less contrast between winter and summer, with differences of about 15 %, with the maximum observed in spring, in late October of 35 %. *Mid-level* clouds have a maximum of *amt* in the beginning of January (40 %) and minimum on the first 15 days of August with 17 %. Cumuliform clouds have an observable seasonal behavior with differences between winter and summer of 18 %. The maximum is observed in the end of December with 20 % and the minimum on the last 15 days of September (2%).

4.2.2. Inter-annual variability of cloud amount

The inter-annual variability of cloud amount is analyzed in this section. Seasonal mean values are shown in Figure 15 for the six main cloud categories. Seasonal variability and trends are observable especially for low *stratiform* and mid-level clouds. Low clouds have an increasing trend due to the *stratiform* variability. This increase is observable from the second half of 1980's.

Total cloud amount (**Clouds**) has not a clear trend in any season, with maxima of annual means occurring in summer. Absolute maximum and minimum of total cloud amount is perceived in summer of 1975 (87.7 %) and winter of 1963 (42.7 %), respectively. For mid-level clouds, a decrease after 1990 in all the seasons is evidently observed. The maximum occurred in summer of 1965 (53.2 %) and minimum in winter of 2010 (1.9 %). Conversely, *cirriform* clouds presented a slight increase especially in summer with maximum observed in summer of 2010 (41.4 %) and minimum in winter of 1964 (7.4 %). Furthermore, low clouds presented a maximum in spring of 2005 (70.1 %) and minimum in winter of 1972 (25.2 %). In the same years, the maximum and minimum of stratiform clouds were observed, with 71.7 % and 24 %, respectively.
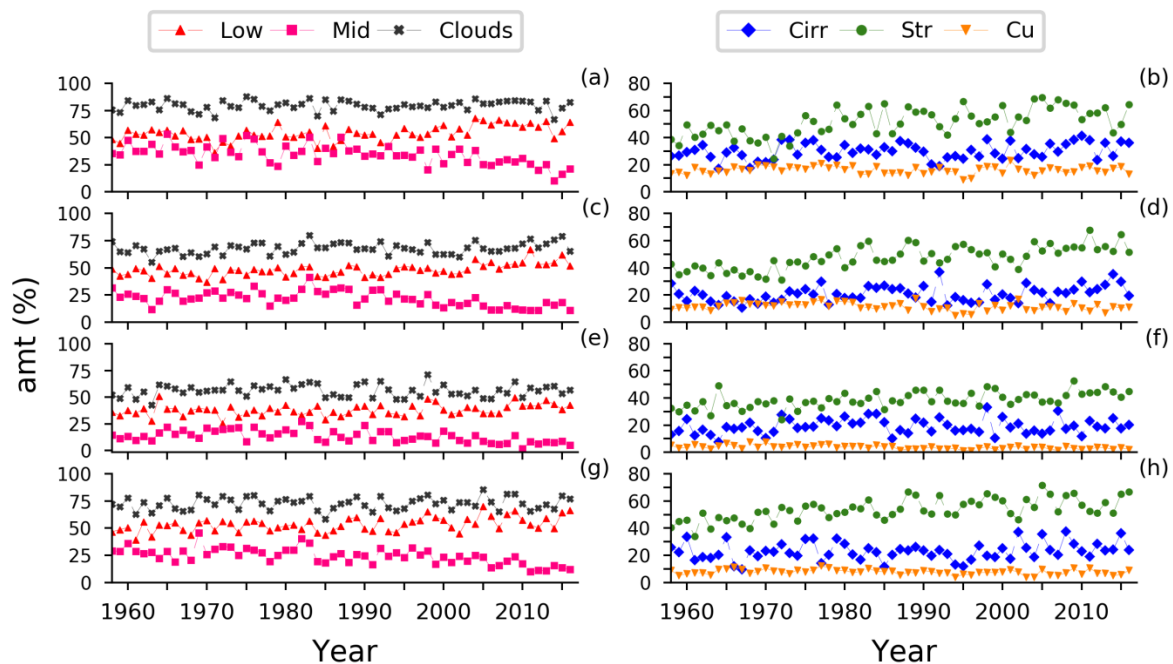
Figure 15: Mean values of cloud cover (amt) per year computed for every cloud type in summer (a,b), autumn (c,d), winter (e,f), spring (g,h).

Cumuliform clouds presented the maximum in summer of 2001 with an absolute value of 24 % and minimum in winter of 1995 with 0.5 %.

Trend values computed as the slope of linear regression are shown in Table 4. We estimated annual trends and for each season separately. Bold values indicate trends that are statistically significant at 5 % confidence level. These values were computed for the total time interval and for the first and last 30 years.

Table 4: Seasonal and annual trends (%/decade) computed for each cloud type, in three different time intervals. Statistical significance was computed by the modified Mann-Kendall Test at 5 % of confidence level and they are highlighted in bold.

| Cloud Type | PERIOD TIME | | | | | | | | | | | | | | |
| | 1958-2016 | | | | | 1958-1988 | | | | | 1987-2016 | | | | |
	DEF	MAM	JJA	SON	Total	DEF	MAM	JJA	SON	Total	DEF	MAM	JJA	SON	Total
Low	**2.0**	**1.8**	**1.0**	**1.8**	**1,6**	-0,1	0,5	-0,6	1,0	0,2	**4,4**	**4,1**	**2,3**	2,3	**3,2**
Mid	**-3.1**	**-2.2**	**-1.6**	**-2.7**	**-2,4**	-0,3	2,2	0,5	-1,3	0,3	**-7,3**	**-5,3**	**-3,1**	**-4,8**	**-5,2**
Cirr	1.0	**1.1**	0.4	0.7	**0,8**	2,3	1,9	**2,1**	0,0	**1,6**	**2,2**	2,2	0,2	2,4	**1,7**
Str	**3.7**	**3.5**	**2.0**	**3.0**	**3,1**	**5,9**	**5,7**	**2,1**	**5,0**	**4,8**	1,5	2,2	1,3	0,8	1,3
Cu	-0.1	**-0.5**	**-0.5**	**-0.3**	**-0,3**	0,1	0,3	-0,4	0,2	0,1	**0,7**	0,0	0,2	0,2	0,2
Clouds	0.2	**0.8**	0.1	0.4	0,4	0,8	**2,3**	1,2	0,3	1,1	0,1	1,2	0,3	0,4	0,6

From 1958 to 1988 an increasing trend is observed, but only with statistical significance in all seasons for *stratiform* low clouds. For *cirriform* clouds, statistical significance is observed in winter (2.1 %/decade) and for all

the year with 1.6 %/decade. For total cloud cover only in autumn an increase was observed (2.3 %/decade).

After 1987 the increasing trend is higher for low clouds (3.2 %/decade) due to a little increase with no statistical significance of *Cu* and *stratiform* low clouds. In addition, it is noteworthy the decrease observed for mid-level clouds in all seasons, with trend with annual mean values of about -5.2 %/decade. In addition the increase of *cirriform* clouds of 1.7 % was noted in this period time.

For the total period of study, from 1958 to 2016 the decrease in *mid-level* clouds amount in all the seasons with statistical significance is observed. The maximum decrease of about -3 %/decade was found in summer. *Cirriform* clouds showed a positive trend with significance in an annual basis (0.8 %/decade) and in autumn (1.1 %/decade). *Cumuliform* clouds presented a decreasing trend with statistical significance, except for summer. But low clouds increased in all seasons (above 1 %/decade) as a consequence of the highest increasing trend observed for low stratiform clouds (above 2 %/decade) in all seasons.

Comparing trends computed for a grid near the region for daytime data by Eastman and Warren (2013) for the period 1971-2009, differences in low cloud cover were found. While they reported a decreasing trend, it is clearly noted an increasing trend of low clouds in this study. These differences are due to stratiform clouds, because in this study a significant increasing trend was observed for all season, whereas for Eastman and Warren (2013) a minor increase was only observed in summer and autumn. Moreover, low cumuliform cloud trends showed the best agreement between both studies, with reduction in all seasons.

Trends of *high* and *mid-level* cloud almost agreed, presenting higher decrease in our study. Differences in trends were only observed in summer for mid-level clouds and spring for high clouds. For the total cloud cover trends, similar results were found, except for spring and summer when positive trends were observed in this study, but with no statistical significance.

Seasonal trends at distinct local time are shown in Table 5. It is clearly observed a decrease for *mid-level* clouds during daytime hours in all seasons with maximum decrease at sunrise. The absolute maximum occurred in spring during sunrise (-3.8 %/decade). Low and stratiform cloud amounts were increasing in the afternoon with maximum at sunset, except in winter, when maximum trends occurred around noon, while cumuliform clouds showed decreasing trend near noon, except during summer. *Cirriform* cloud amount increased in sunrise and midday, but with statistical significance around noon for autumn, spring and in the annual basis, and around sunrise in summer. For total cloud cover, an increasing trend of 0.8 %/decade around noon and a decreasing trend of -0.5 %/decade at sunrise were observed on an annual basis. In autumn, cloud cover showed increase after midday and decrease at sunrise.

Table 5: Trends (%/decade) of 6 six clouds types computed for sunrise (7 SLH), noon (13 SLH) and sunset (18 SLH). Statistical significance was computed by Mann- Kendall Test in 5 % and they are in bold.

Cloud Type	DJF			MAM			JJA			SON			Total		
	7 SLH	13 SLH	18 SLH	7 SLH	13 SLH	18 SLH	7 SLH	13 SLH	18 SLH	7 SLH	13 SLH	18 SLH	7 SLH	13 SLH	18 SLH
Low	0,4	**2,6**	3,4	-0,1	**2,8**	3,5	0,6	**1,2**	1,0	0,6	**2,2**	2,6	0,4	**2,2**	2,6
Mid	**-3,5**	**-3,1**	**-3,3**	**-3,3**	**-1,8**	**-3,1**	**-2,5**	**-1,4**	**-2,1**	**-3,8**	**-2,2**	**-2,7**	**-3,2**	**-2,2**	**-3,0**
Cirr	**1,3**	0,7	-1,0	1,2	**1,4**	0,1	0,9	0,2	-0,2	0,6	**1,1**	0,6	1,1	**0,8**	-0,2
Str	0,6	**6,2**	4,2	0,0	**6,5**	3,7	0,7	**2,8**	1,3	0,7	**4,6**	2,9	0,5	**4,9**	3,0
Cu	0,1	0,4	0,2	0,1	**-1,1**	0,2	0,1	**-1,0**	0,0	0,2	**-0,7**	0,2	0,1	**-0,6**	0,1
Clouds	-0,4	0,6	0,2	**-0,7**	**1,7**	**1,2**	-0,2	0,1	-0,4	-0,5	0,9	0,6	**-0,5**	**0,8**	0,4

4.2.3. Simultaneous occurrence and combinations of clouds

Following the methodology applied by Warren et al. (1985), in this section, the simultaneous occurrence of cloud types is analyzed. Table 6 shows cloud frequency of occurrence and cloud frequency of co-occurrence (cloud type occurrence given another cloud type) for each season. In this case, *Cu, Sc, St, Cb, Ac, Ns* and *Cirriform* clouds were employed. As can be seen, almost all cloud types presented maximum frequency in summer except for *stratus* clouds, whose maximum was observed in spring. In this season, the frequency of cold front passage in the region is high, with 27 % of events of the year (Morais et al., 2010).

Table 6: Frequency of occurrence and co-occurrence for clouds types for each season

Given cloud	season	Fq	Frequency of occurrence due to given cloud type							
			Cu	Sc	St	Cb	Ac	As	Ns	Ci
Cu	DJF	40.7	-	56.8	0.9	4.4	32.3	14.5	0.0	46.8
	MAM	33.2	-	58.3	1.2	1.8	21.5	6.1	0.0	31.8
	JJA	13.9	-	54.1	0.9	0.3	14.9	2.9	0.0	25.9
	SON	22.7	-	55.9	0.9	1.6	21.4	7.7	0.0	34.9
Sc	DJF	57.4	23.1		16.2	3.4	43.5	33.8	0.1	48.3
	MAM	51.9	19.4		16.3	1.4	32.5	18.7	0.0	33.9
	JJA	33.8	7.5		23.7	0.2	25.4	14.3	0.0	28.6
	SON	49.2	12.7		24.5	1.0	32.8	25.0	0.0	36.1
St	DJF	16.1	0.3	57.7		2.0	34.8	67.1	0.0	52.5
	MAM	17.2	0.4	49.4		0.9	29.4	39.8	0.1	35.4
	JJA	20.6	0.1	39.0		0.2	23.3	32.4	0.0	28.9
	SON	25.4	0.2	47.6		0.6	30.3	54.8	0.1	40.3
Cb	DJF	3.2	1.8	59.6	9.7		54.1	48.1	0.5	61.6
	MAM	1.2	0.6	61.1	12.8		46.3	44.7	0.0	62.1
	JJA	0.1	0.0	58.8	35.3		54.8	45.2	0.0	
	SON	0.9	0.4	52.9	15.3		48.4	42.4	0.5	67.2
Ac	DJF	40.1	10.0	46.8	2.5	2.8		41.0	0.0	69.6
	MAM	28.2	5.8	45.6	3.1	1.2		31.2	0.0	57.0
	JJA	18.6	1.8	28.4	2.7	0.2		28.6	0.0	51.1
	SON	27.6	3.9	38.7	3.4	1.1		41.2	0.0	61.8
As	DJF	24.8	4.5	58.8	7.9	4.0	66.2		0.1	89.4
	MAM	13.2	1.6	55.9	8.9	2.4	66.6		0.0	88.3
	JJA	7.9	0.3	38.1	9.0	0.4	67.8		0.0	86.9
	SON	17.2	1.4	47.2	9.8	1.5	65.9		0.1	89.6
Ns	DJF	0.1	0.0	30.3	0.0	12.1	12.1	39.4		
	MAM	0.0	0.0							
	JJA	0.0	0.0							
	SON	0.0	0.0							
Ci	DJF	51.7	11.5	33.1	1.1	1.8	31.0	8.1	0.0	
	MAM	36.8	7.5	32.7	1.8	0.9	24.5	5.1	0.0	
	JJA	32.8	2.9	16.1	1.3	0.1	16.7	3.4	0.0	
	SON	38.3	5.6	26.4	1.5	0.8	21.9	5.5	0.0	

Likewise, it is noticeable the *Sc* maximum in summer in contrast with the global studies of Warren et al. (2007) and Wood (2012). However, it is important to keep in mind that the Metropolitan Area of São Paulo (MASP) is located over a plateau of 800m above sea level and close to the coast (about 50 km in straight line).

Due to the parallel orientation of the mountain range to the coast line, mountain-valley circulation contributes to the advance of sea breeze inland. In addition, circulation generated by the urban heat island effect makes the sea front to be stationary at MASP. This phenomenon influences the local circulation and, acting isolated or with other systems, contributes to many cases of floods in the region (Freitas et al., 2009). From the analysis of wind direction, Perez and Silva Dias (2017) found that the sea breeze reaches the city earlier in summer and spring (around 14:00 LT), compared to the other seasons.

In summer and spring the early arrival of the breeze is associated to the higher contrast between the ocean and land surface temperatures. The conditions are most favorable due to the increase of the land temperature and the position of the South Atlantic high pressure. The breeze front can contribute to the formation of convective clouds along with a composite of clouds such as stratocumulus. Besides, possible advection of low *stratiform* clouds formed near the coast and in the edge of the mountain barrier can occur. Note that more than 50 % of *Cb* cases were in the presence of stratocumulus in all seasons. Conversely, cumuliform clouds frequency, when *Cb* was present, was near null. Dynamic processes associated with *Cb* can be another forcing mechanism for stratocumulus development in the area. Downdraft outflow from *Cb* can lead to the formation of other low cloud types, by means of formation of gust front (Mahoney, 1988). This was not reported in previous studies using synoptic reports, probably because of the constraint mentioned before related to the presence of *Cb* and the way of synoptic observations were carried out.

It is also significant the higher dependence of *mid-level* and *cirriform* clouds on *cumulonimbus*. Observe that *cirrus* is present with almost all cloud types, with especially higher frequency with presence of *As*, *Ac* and *Cb*. Likewise, note how *Sc* and *Ac* are related especially in summer, once *Ac* can form from ascending layers of stratocumulus clouds.

For the analyzed period, 536 combinations of clouds were found; the top 10 by frequency of occurrence for each season are shown in the Figure 16. As can be observed, there is an evident predominance of *stratiform* cloud combinations except for *Cu-Ci*, Ci and *Cu*. The highest frequency was found for

Sc with maximum of about 16 % in spring. Maxima frequency are also observed in spring for combinations with *stratiform* clouds; in summer for the combination with *cumuliform* clouds; and, in winter, for *Ci* and *Ac*. Mean cloud cover when the combination is present (awp) is shown in Figure 15.b. Observe the higher values for *St*, *Sc-St*, *Sc-Ac* and *Sc-Ac-St*. Minima of *awp* were observed for *Ci* and *Cu* with 50 % and 45 %, respectively.

The diurnal cycle of the first 8 combinations is shown in Figure 17. Combinations of stratiform clouds show an inverse diurnal cycle compared to combination with cumuliform clouds. At sunrise, the highest frequency for stratus combination is observed. Also, Sc showed increase in the morning with maximum near 9:00 LT. Observe the maximum frequency of cirrus-only at 10:00 LT, following the decrease observed for low cloud cover. Around noon Sc, Sc-Cu and Cu were predominant. At sunset Sc has the highest frequency followed by stratus clouds. Observe, in the figure 17.b, that cloud cover, when combinations are present, is higher throughout the day for low stratiform combinations, and the influence of the solar heating cycle on cloud cover of cumuliform combinations is also noted.
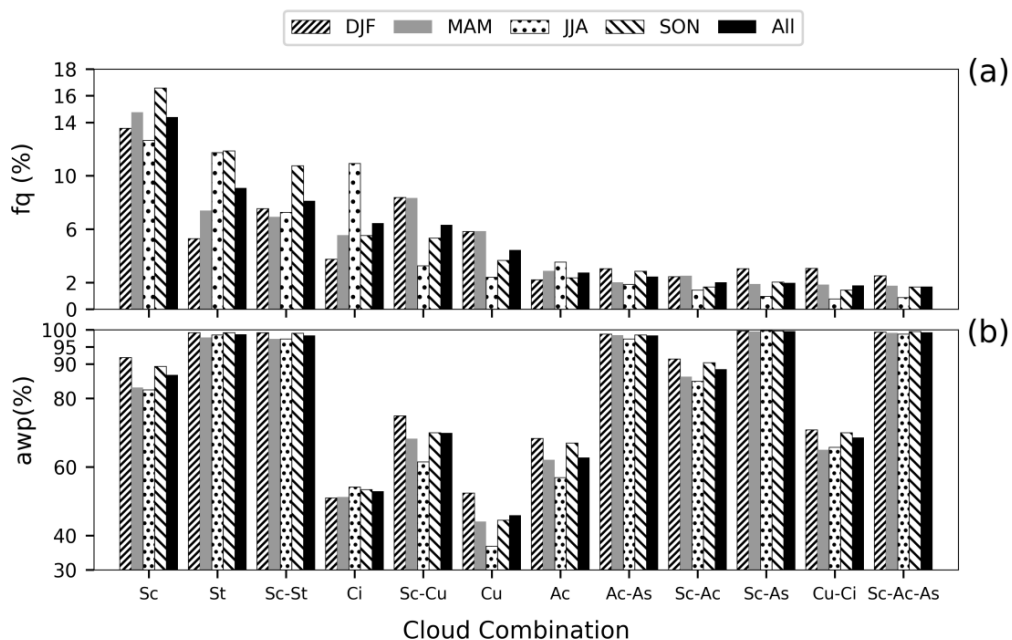

Figure 16: Mean frequency of occurrence (fq) and sky cover when present (awp) for the12 main cloud combinations observed at each season.
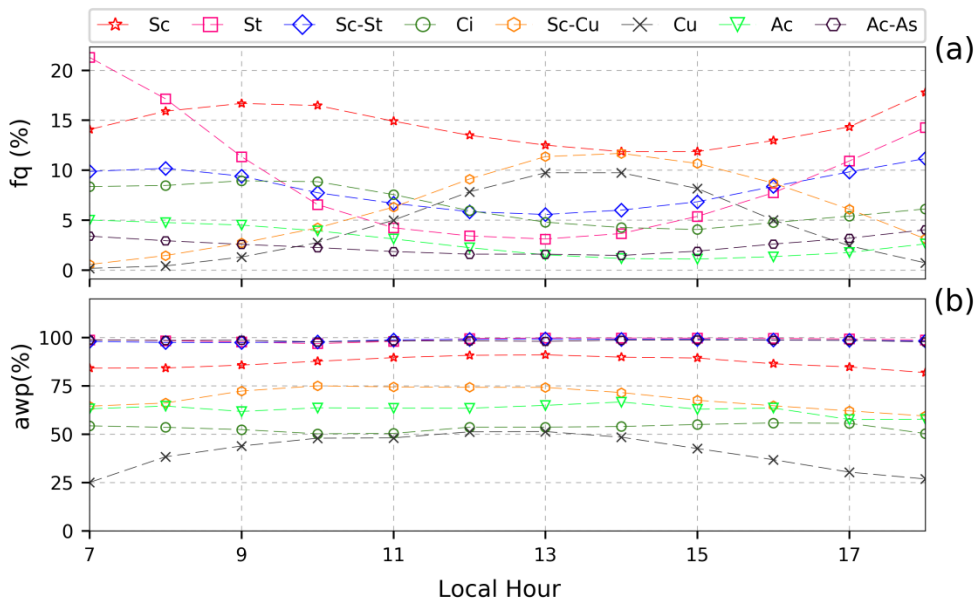
Figure 17: Diurnal cycles of the 8 main combinations of clouds for frequency of occurrence (a) and amount when present (b).

4.3. Sensitive study for COD retrievals

4.3.1. Sensitive of properties at 415 nm

To build the lookup tables for COD retrievals using T, a sensitivity analysis of T to changes in some variables was needed. Variations of T at 415 nm modeled by uvspec to variations of surface albedo, aerosol vertical profile, SSA, g, AOD, gas concentrations and cloud properties are analyzed in this section. The sensitivity of each variable was carried out by changing the variable between percentiles 5 and 95 % according to measured data, while keeping the others constant. Values of COD were assumed constant equal 2 for ice clouds and 10 for low clouds. Default model configuration (section 3.4) is used with CSZA of 0.86, AOD_{415} with 0.3, SSA_{415} assumed from SSA_{440} with 0.81 and g_{415} assumed from g_{440} with 0.7.

Variations of T_{415} with respect to aerosol properties are presented in Figure 18. The effect of the four aerosol profiles, retrieved from ground-based measurement of Lidar and sun-photometer at the site, is compared with the two profiles given by the *LibRadtran* library, labeled summer-spring and winter-autumn (Mayer et al., 2015). It is clearly observed the little sensitivity of T to the

different aerosol profiles (Figure 18.a). But differences about 1.5 % were found between the typical profile and the profile for spring.
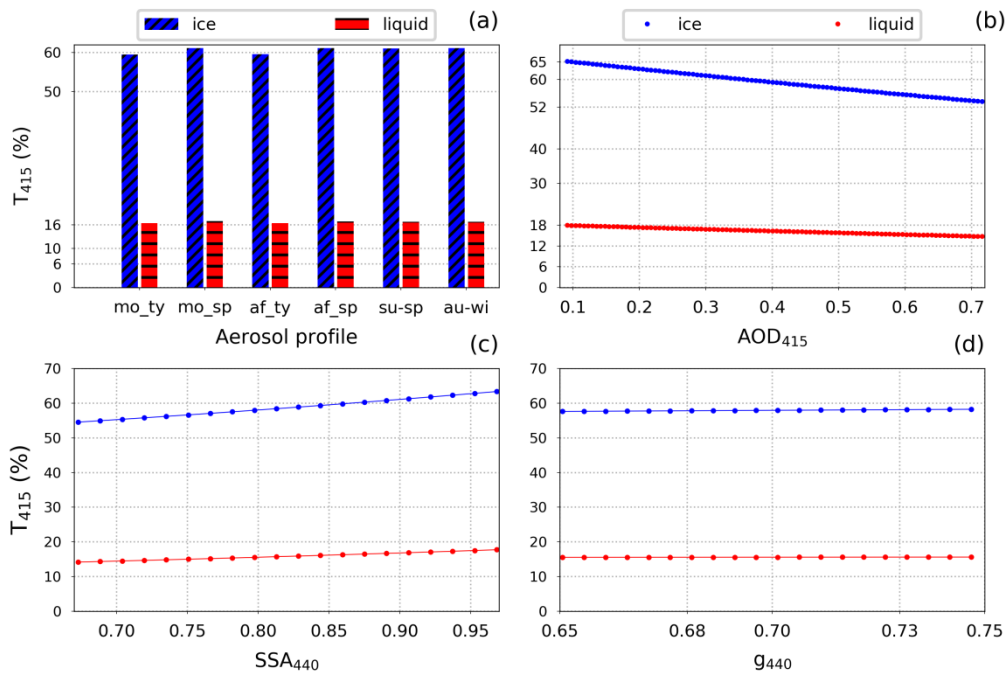
Figure 18: Sensitivity of transmittance at 415 nm for liquid and ice clouds to variations of aerosol vertical profile [mo_ty= morning typical, mo_sp= morning in spring, af_ty=afternoon typical, af_sp=afternoon in spring, su-sp=summer-spring and au-wi=autumn-winter given by LibRadtran (Mayer et al., 2015) (a), variations of AOD415 (b), variations of SSA440 (c) and g440 (d).

In the case of variations of AOD_{415} (Figure 18.b) changes were observed, especially for ice clouds, for which T_{415} decreased linearly with slope of about 21.5 % per AOD_{415} unit. For low clouds, there is less sensitivity to aerosol load of about 8.3 % per AOD unit.

The SSA_{440} also influenced the T_{415} (Figure 18.c), the increase of SSA_{440} contributed to the increase of scattering and hence T_{415} was higher. Between percentile 95 and 5, the differences of T were about 7 % for liquid and ice clouds. The variation of T between 5 % and 95 % of g_{440} obtained from AERONET products was almost imperceptible (Figure 18.d). Differences between the extreme values of g_{440} were 0.6 % and 0.1 % for ice and low clouds, respectively.

The sensitivity of T_{415} to CSZA was higher (Figure 19 a), especially for ice clouds, between 95 % and 5 % percentiles, the difference can reach more

than 100 %. For surface albedo, NO_2 and O_3 there is no perceptible variation (Figure 19).
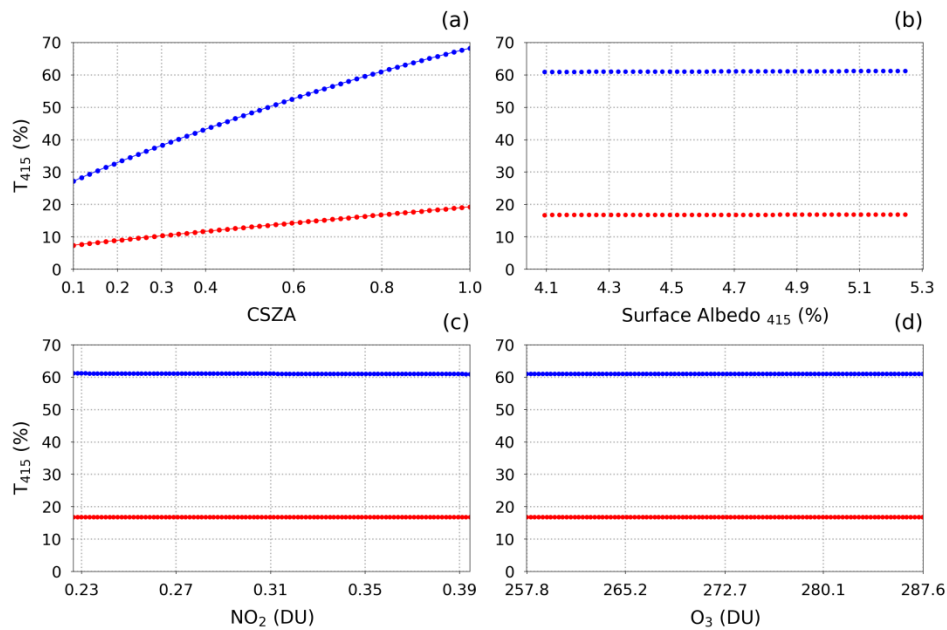
Figure 19. As in the Figure 16 but for CSZA (a), surface albedo at 415 nm (b), dioxide of nitrogen (NO2) (c) and ozone (O3) (d).
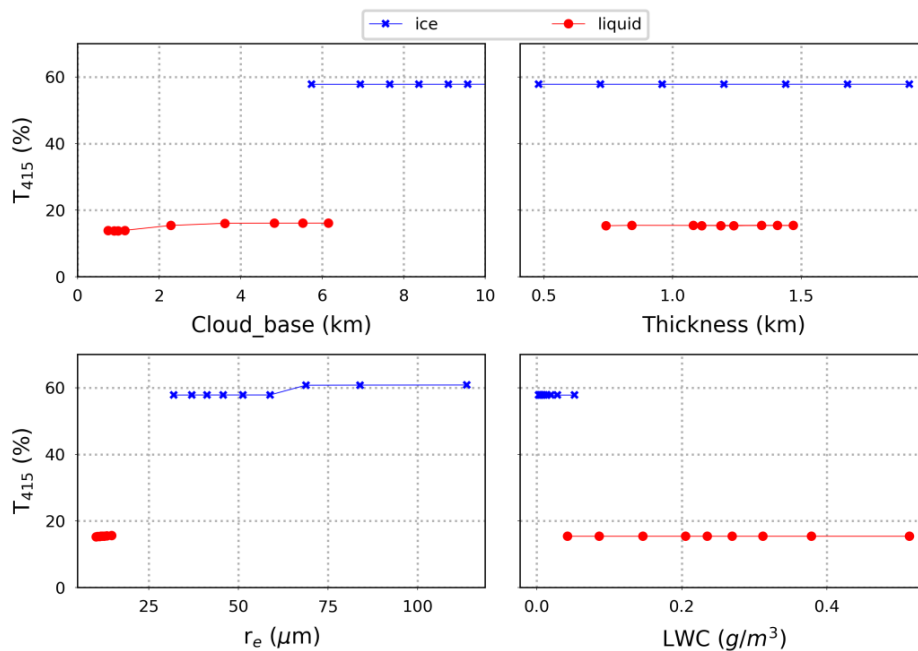
Figure 20. Variations of total transmittance at 415 nm to cloud base, thickness, r_e and LWC for ice and liquid clouds with a constant value of COD.

Sensitivity of T_{415} to cloud properties is shown in Figure 20. For liquid clouds, T_{415} varied around 2 % with the height of cloud base between percentiles 5 and 95 %. Note the lower variability to r_e of ice and liquid clouds. For high clouds, and r_e larger than 60 μm the shift, of about 1.3 % in T, is due to

72

the change of habit. For cloud thickness and IWC/LWC no sensitivity was observed, as COD was assumed constant.

4.3.2. Errors affecting COD retrieval

From the previous analysis, the main variables to take into account for retrieving COD are T_{415}, AOD_{415}, SSA, cloud properties such as cloud base height (CB) and r_e as median values. In this section, the contribution of error of each variable to COD retrieval is investigated.

In Figure 21, the relative error of each variable in the COD retrieval for low and ice clouds is shown. For ice clouds errors are higher than low clouds. Smaller errors below 1 % for low clouds properties are observed, but for ice clouds the error of assuming a median of r_e can be 10 %

Note the high influence of aerosol optical properties for the error for COD below 20. For COD below 5, errors are higher than 50 %. However for COD above 50, the errors are lower than 10 % for low clouds. Comparing to the error of the retrieval method of COD for low clouds using sun-photometry (17 %) (Chiu et al., 2010), the current method has better accuracy considering total overcast conditions for lower clouds, when COD is higher than 20.

Figure 21. Relative error of COD retrieval due to errors in each variable: AOD, SSA, T, r_e and CB and the total error for each COD value. For low clouds (a) and high clouds (b).
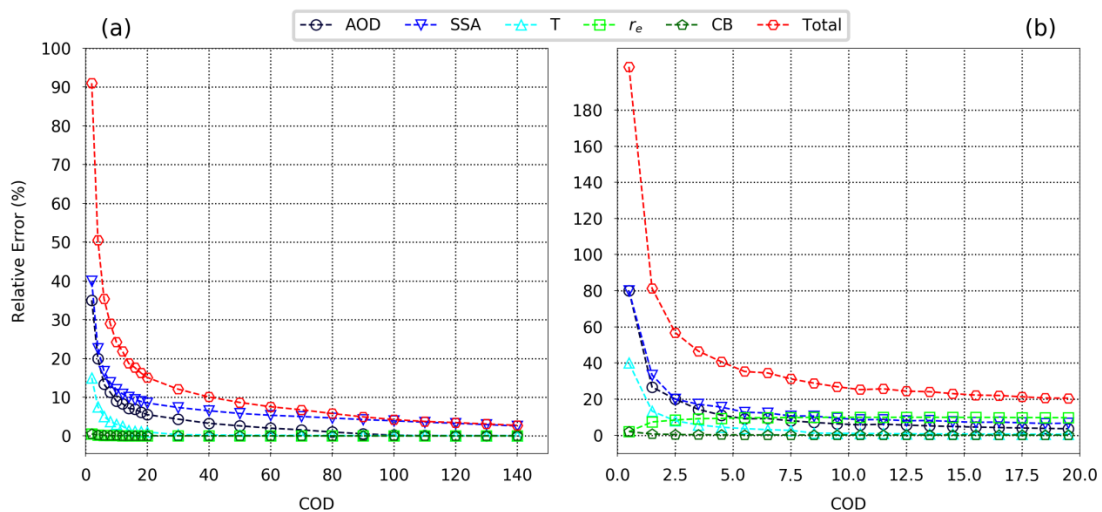
The current method does not include an estimation of instantaneous values of spectral SSA. Therefore, for future works, consideration of SSA estimation in the instantaneous measurements is advised. SSA can be retrieved using

measurements of spectral diffuse irradiance from the MFRSR for clear sky conditions (Serrano et al., 2014) or can be obtained from sun-photometer measurements (Dubovik et al., 2000).

4.3.2.1. Error of AOD estimation into COD retrieval

As pointed out previously, AOD_{415} is the second component that most affects COD retrievals. Therefore, the validation of methods employed to infer AOD_{415} in cloudy conditions and the contribution of the error to COD retrievals are needed.

The accuracy of the method for inferring AOD is validated using coincident AOD_{440} retrieved from sun-photometer. Note that methods do not include the possible influenced of cloudiness on the AOD profile, as usually is carried out in previous works (Guerrero-Rascado et al., 2013; Mateos et al., 2013; Salgueiro et al., 2016), that is a topic where more studies will be needed in the next years. For each method, some AOD_{440} cases in the sample are assumed as not measured. These cases were estimated by the method and differences with real AOD_{440} were calculated. Afterward, errors were computed in reference to the real value.

The errors of each method are presented and resumed in Table 7. The best accuracy was observed by time interpolation method on the same day (error of 0.03). When AOD values on the day were not available, for instance a value near sunrise or sunset, the estimation was performed using the nearest value and adjusted using the mean monthly diurnal cycle. These estimations resulted in errors between 0.07 and 0.08 (*inter 3 and 4*).

The worst accuracy was obtained using the monthly mean diurnal cycles of AOD (error of 0.11). The method was applied only for cases when there were no AOD measurements as close as two days, otherwise the monthly diurnal cycle was adjusted using diurnal mean AOD of the nearest day. Note that the accuracy improved using adjusted diurnal cycles, with errors of 0.08 (*Inter 5*).

The contribution of these errors to total error of COD is shown in Figure 22. From the figure, an improved of accuracy in the retrieval is observed specially by the time interpolation throughout the day. Despite this improved in

estimating AOD for cloudy conditions, error of retrieval for lower CODs is higher.

Table 7: Error of estimating AOD_{440} for cloudy conditions of each method: time interpolation throughout the day (*Inter 1*), monthly mean diurnal cycle of AOD (*Inter 2*), adjusted monthly mean diurnal cycle from the AOD measured in the previous time (*Inter 3*) and later time (*Inter 4*), adjustment of the climatological monthly diurnal cycle of AOD from mean diurnal AOD value computed as close as at least 2 days (*Inter 5*).

Method	RMSE	MAE	Error	R. Error	Number
Inter 1	0.22	0.13	0.03	0.15	19979
Inter 2	0.60	0.46	0.12	0.62	20203
Inter 3	0.47	0.32	0.08	0.34	16034
Inter 4	0.41	0.28	0.07	0.32	16163
Inter 5	0.48	0.36	0.08	0.41	4328
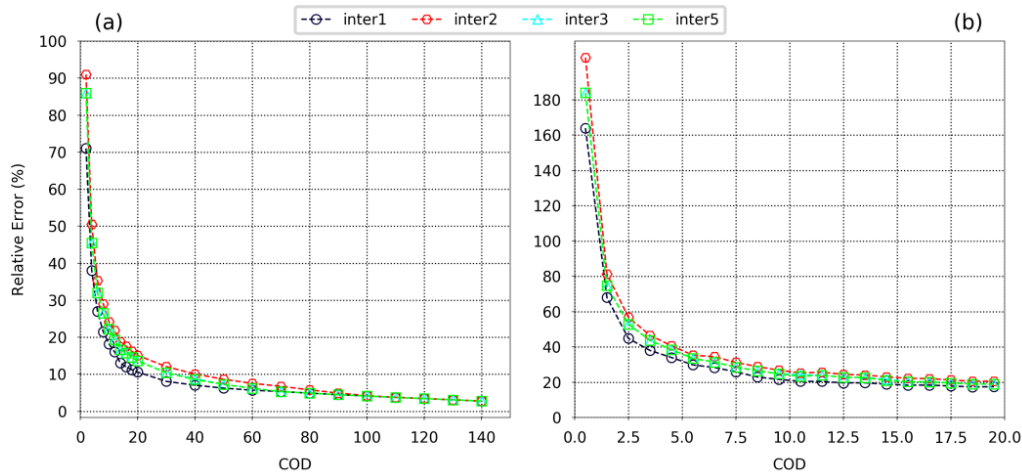
Figure 22: Total relative error of COD retrieval, for different methods of assuming AOD in cloudy cases, for low clouds (a) and ice clouds (b).

4.3.3. Model response to clear sky global irradiance

As explained previously, pyranometer measurements were performed every minute, while AOD retrievals from AERONET were available in intervals of 15 minutes or longer. Thus, in this section, we compare measured irradiance with the pyranometer with modeled by *LibRadtran* in clear sky conditions. Two scenarios were analyzed: cases when there was temporal coincidence of AOD_{500} and irradiance measurement (no interpolation) and cases when AOD_{500} was interpolated to pyranometer measurement time.

In Figure 23, the ability of the model to simulate global irradiance as measured by the pyranometer for clear sky condition is shown initially

determined by all sky-camera. In order find out cases with presence of sub visual cirrus in clear sky cases, from AOD level 1.0 to 1.5 cloud contaminated cases are selected. Therefore the selected cases coincident in time with pyranometer clear sky measurements were considered as cloud contaminated and not taking into account in the comparison. A total of 14472 cases of clear sky were analyzed.

The good agreement is observed between modeled and measured clear sky G, with NRMSE of about 4 % and the overestimation of G of about 3 %. Around 98 % of cases an absolute difference was below 10 % and 80 % of them were lower than 5 % (Figure 22 b). Overestimation can be a consequence of including a mean value of SSA, especially in spring with 0.9, because not always in this season, biomass burning aerosols reach the region. Differences were into the range of errors of pyranometer of about 5 %.
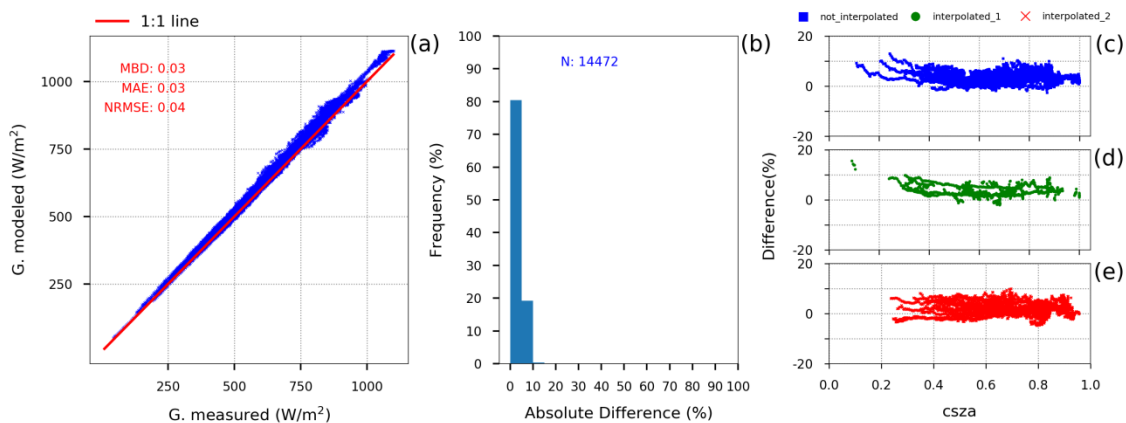
Figure 23: Instantaneous global irradiance modeled by 1-D *uvspec* and measured by pyranometer (a), frequency distribution of absolute differences between modeled and measured values (b), and relative differences using no interpolated AOD and water vapor (not interpolated) (c), interpolated on the day or adjusted from monthly diurnal cycle (interpolated_1) (d) and AOD and water vapor computed from mean monthly diurnal cycles (interpolated_2) (e).

Relative differences were computed for different AOD_{500} and water vapor interpolation schemes and shown in Figures 23 c-e. Observe how there is no significant differences between interpolation schemes. When no interpolation was applied, the modeled result could reach a maximum of 12 % difference, but more than 97 % of cases were below 10 %. Observe that only 1 % of cases were underestimated by the model. Using interpolation on the same day, the differences were similar to not interpolated cases, but there was a little increase for CSZA below 0.2 with maximum of 15 %. It is noteworthy the increase in

underestimation of model for cases when interpolation was made using monthly mean diurnal cycles, but differences remained between -5 % and 10 %.

Relative differences of T_{dir} and T at 415 nm of coincident modeled and measured by reference MFRSR (numbered 345) are shown in Figure 24. A total of 1105 clear sky cases observed by the sky camera were analyzed. The difference was higher for lower CSZA with extremes observed near 0.4 with 18 % of relative differences for T and 12 % for T_{dir}.

Differences computed for direct sun transmittance allow having an estimate of model error for computing direct sun transmittance at 415 nm. This error will be employed for direct sun criterion for defining solar disk conditions. The direct sun criterion assumed an error up to 15 %.
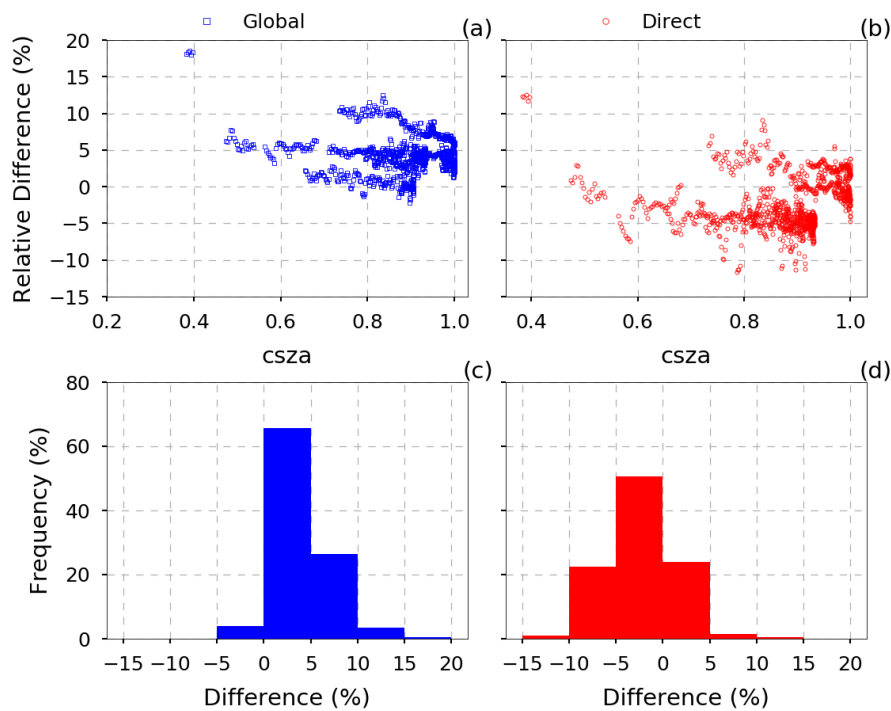
Figure 24: Relative differences of T at 415 nm modeled versus T at 415 nm measured by MFRSR 345 (a,c) and of T_{dir} modeled and measured at 415 nm (b,d).

4.3.4. Spectral diffuse ratio validation.

Validation of DR is assessed in the following. In Figure 25 the DR for cases of clear sky, low clouds with total overcast and high clouds with total overcast conditions, carefully retrieved from camera observations, are shown. In addition, the curve that limits clear sky conditions and cirrus clouds computed by *uvspec* with AOD 0.3 is presented. Note the differences between cloudy and

clear sky conditions. Clear sky values were around the definition computed by the model (green line), with lower ratio values, as the diffuse component under clear sky is higher for shorter wavelengths, due to the influence of radiation scattering by air molecules. When clouds are present, the component of Rayleigh scattering becomes less important, with an increase of multiple scattering due to clouds and Mie scattering, decreasing the spectral dependence.
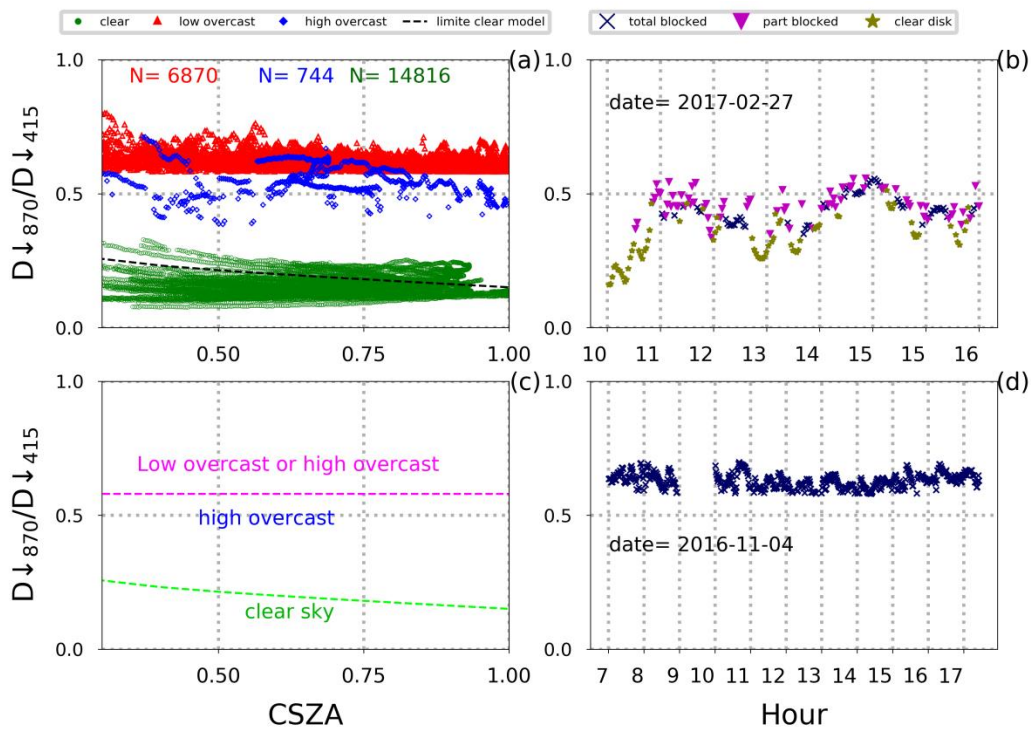
Figure 25: Validation of ratio of downwelling diffuse irradiance (D↓) at 870 nm and 415 nm (DR) for cases discriminated by the all-sky camera (a), the classification defined from model and observed values (c), for a specific day with low broken clouds (b) and for a specific day of low clouds with total overcast condition (d).

High clouds showed intermediate values, i. e., above clear sky threshold and below low cloud values, but some overlaps can be observed. It is important to note that only visual cirrus clouds are shown, leading to higher differences with clear sky. It is remarkable how low cloud ratios are systematically above 0.58 and no sensitive to CSZA. In the case of low clouds, besides the little spectral dependence, the contribution of surface albedo favors to increase the differences with clear sky. Under these considerations, it is possible to classify as clear sky or cloudy atmosphere. In the figure 25 c definitions are shown based on the former figure and Figure 5.

Specific days of study with low cloud overcast conditions and low broken clouds are shown in Figures 25 b-d. Observe the differences between the cases, for low broken clouds the spectral ratio never reached 0.58 compared to total overcast where about 99 % of the cases are above 0.58. That can be a good indicator of cloud cover as reported by Min et al. (2008). Then, based on the analyses just shown, it is possible to use the spectral ratio of diffuse irradiance, at 870 nm and 415 nm, to define conditions of cloudiness. These conditions were used especially for observations when the sky camera was not available, i.e. before September of 2016.

4.4. Effective cloud optical depth (ECOD)

4.4.1. Validation with pyranometer ground-based measurements

A total of 6870 cases of ECOD retrieved coincident in time with pyranometer measurements were used as input for computations of G. The irradiance calculated by the *uvspec* model was compared with pyranometer measurements. For this analysis, ECOD values were modeled with different effective radius of values from percentiles 5 and 95% of r_e retrieved from CloudSat-CALIPSO products. For low clouds the relation between modeled and measured is shown in Figure 26.

Lower differences are observed with the increase of CSZA, as expected. For CSZA near 0.2 higher differences up to 100 % are observed. Differences with maximum of 10 % of absolute value are observed for CSZA higher than 0.95. A good agreement between modeled and measured results is observed with NRMSE of 9 % for the three r_e used; more than 60 % of cases are below 10 % of absolute difference. But using percentile 5 of r_e, there is a slightly underestimation of the model, and for the 95 % percentile, little overestimation is observed with MBD equal 0.03.
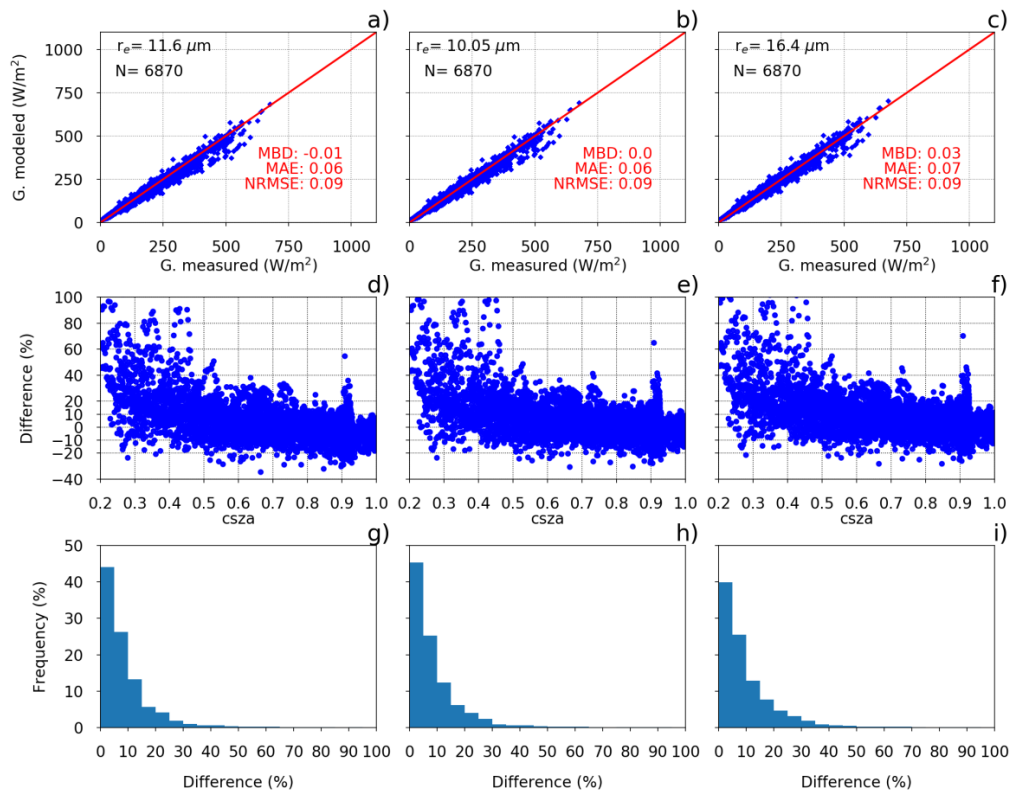
Figure 26: Comparison of modeled global irradiances using percentile 50 (a,d,g), percentile 5 (b,e,h) and percentile 95 of r_e for ECOD values retrieved for low clouds with total overcast condition.

For cirriform clouds (Figure 27), 744 cases were analyzed. Despite the error retrieving ECOD for high clouds is higher than low clouds, differences observed for high clouds are lower as compared to low clouds. That can be due to the fact that, for high clouds, D↓ has less weight in G because SS is not totaling extinct and 1-D model computes SS with higher accuracy as compared to D↓. No significant difference is observed with r_e variation, with the best agreement for data corresponding to percentile of 95 %.

4.4.2. Comparison with COD retrieved from sun-photometer

The sun-photometer (AERONET) method to estimate COD is based on zenith radiance measurements and not from hemispheric measurements as for MFRSR. The AERONET method is more sensitive to the low scale variation of cloudiness (Chiu et al., 2010) and even narrow interstices at zenith can contribute to differences. The method is more accurate in the presence of low broken clouds, due to the higher dependence on surface albedo, but for low

clouds, in overcast conditions, the contribution of surface albedo can be reduced, resulting in larger differences.
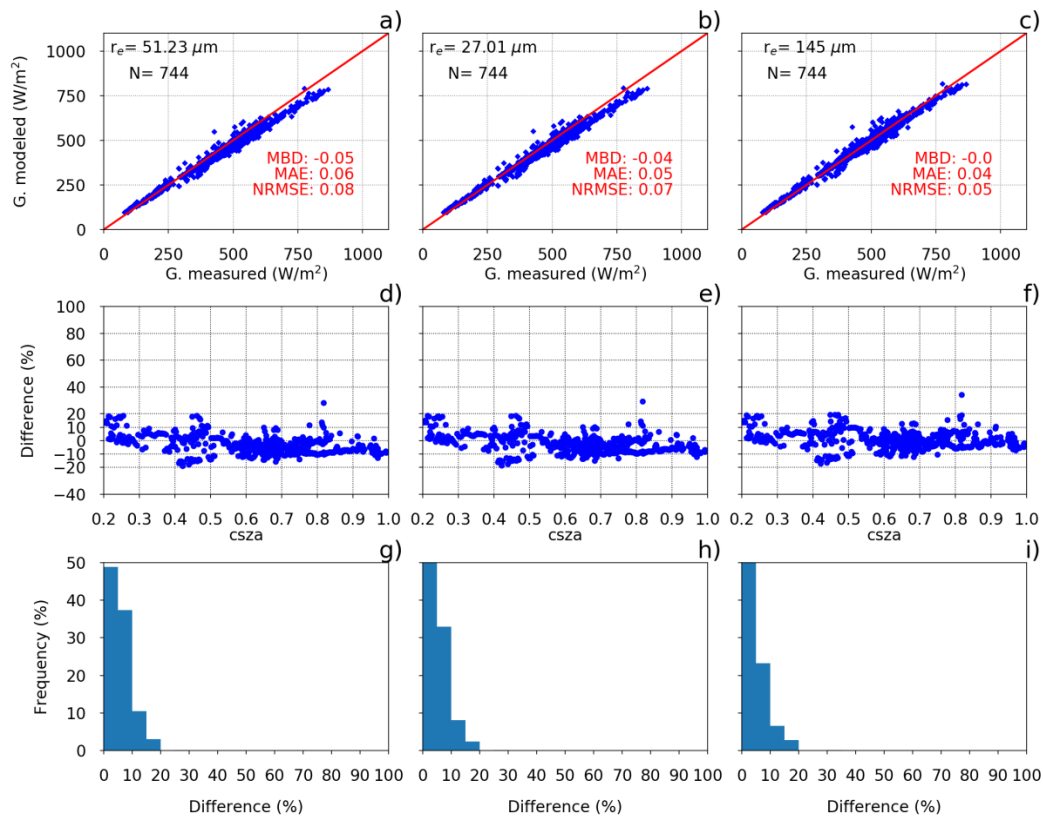
Figure 27: As Figure 25 but for cirrus clouds with total overcast.

In Figure 28, a comparison of COD retrieved from MFRSR every 1 min and AERONET, with each measurement taking about 1.5 min, every 15 minutes, at the site, is shown. For a specific day, with low clouds and total overcast conditions, coincident retrievals are presented (Figure 27 a). Note the CODs agreement between the two datasets and the variability observed for 1 min resolution from MFRSR with COD peaks every 10 or more minutes.

A total of 190 cases of low clouds with total overcast conditions were carefully selected from the sky camera and conditions of obstruction of direct solar radiation. For this 190 time coincident COD cases, shown in Figure 28 b, differences were observed with mean averaged error of 23 % and underestimations of MFRSR COD of 18 %. The discrepancy was higher for COD values above 40, where underestimation of MFRSR respect to AERONET is clearly observed. Those differences have to do with the different procedures

of each method. COD from AERONET is more sensitive to local variations of cloud properties while ECOD from MFRSR depends on cloud cover of the sky.
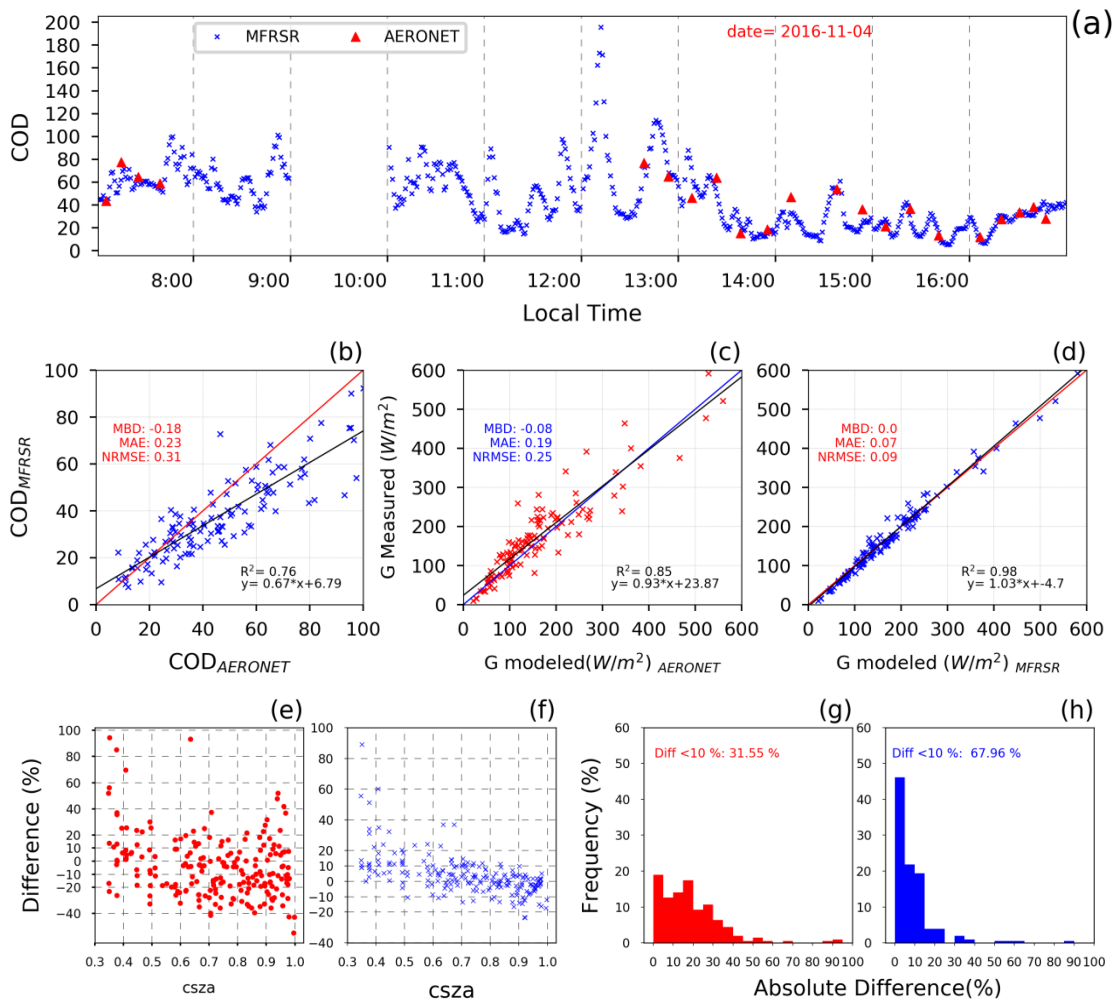
Figure 28: Comparison between COD retrieved from AERONET and the COD retrieved by MFRSR under the presence of low clouds in total overcast condition. Time series for one specific day (a), COD of AERONET vs COD of MFRSR for coincident cases (b). G modeled using COD AERONET vs G measured by pyranometer (c). G modeled using COD from MFRSR vs G measured by pyranometer (d). Differences with respect to CSZA for AERONET (e) and MFSRSR (f). Frequency distribution of absolute error for AERONET (g) and MFRSR (h).

The coincident CODs were included as input in the *uvspec* model and solar global irradiances at the surface were calculated and compared with values measured by the pyranometer (G).

Better agreement between modeled and measured G was observed when using COD estimated from MFRSR (this work) (Figure 28 d). For *MFRSR*, the differences were lower for higher values of CSZA. For AERONET, no dependence with CSZA was observed. Differences under 10 % for MFRSR represented about 70 % of cases, however only 32 % for AERONET. In

resume, it was observed that COD retrieved by MFRSR under total overcast conditions allowed computations of G at surface that agreed better with measured G than AERONET COD in the same conditions.

4.4.3. Effective cloud optical depth, seasonal and diurnal variability.

The seasonal and diurnal COD distribution for low clouds in total overcast condition is shown in Figure 29. Furthermore, histogram of frequency, some statistical values and number of cases are also shown. Statistic differences between season and hours data are observed and checked with the Kruskal-Wallis hypothesis-test (Kruskal and Wallis, 1952) .

Total overcast scenarios due to low clouds were more (less) frequent in spring (autumn). In winter (Figure 29.c), lower values of COD were observed, with the lowest median of 21.2, with 20 % of the distribution with COD values above 40. In spring, there was an increase of COD above 40, with 32 % of the cases. The median value for this season was 28.6 being the maximum of all seasons. Between summer and autumn there was no remarkable differences, with median around 24, but, for autumn, percentile 95 was the largest, equal to 86.5.

Also, the diurnal variability of COD was observed (Figure 29.e-h). Near sunrise, values of COD were smaller with the lowest median of 19.0. The median value increased until the time interval between 12:00 and 14:00 LH (28.3) with 30 % of data with COD above 40. Near sunset the median decreased to 25.9, but still almost 30% of the data presented COD above 40.

The analysis was also applied for visible cirrus cloud (Figure 30) COD. The number of cases decreased as compared with low clouds. As for low clouds, the differences were observed for diurnal and seasonal time intervals, and checked the statistical significance by *The Kruskal-Wallis* hypothesis test.

Cirrus clouds presented COD values above 5, especially in summer, with 23.6 % of the cases. Higher values were observed in spring with median of 3.11 followed by summer with median of 2.88. In autumn, the lowest median was observed and with only 2.5 % of the cases above 5, for the 400 available cases. Lower values of COD were also observed for sunrise with median of 1.94.

Maximum median occurred near midday with 3.21 but after 14:00 LT, the highest amount of cases of COD above 5 was observed (19.6 % of cases).
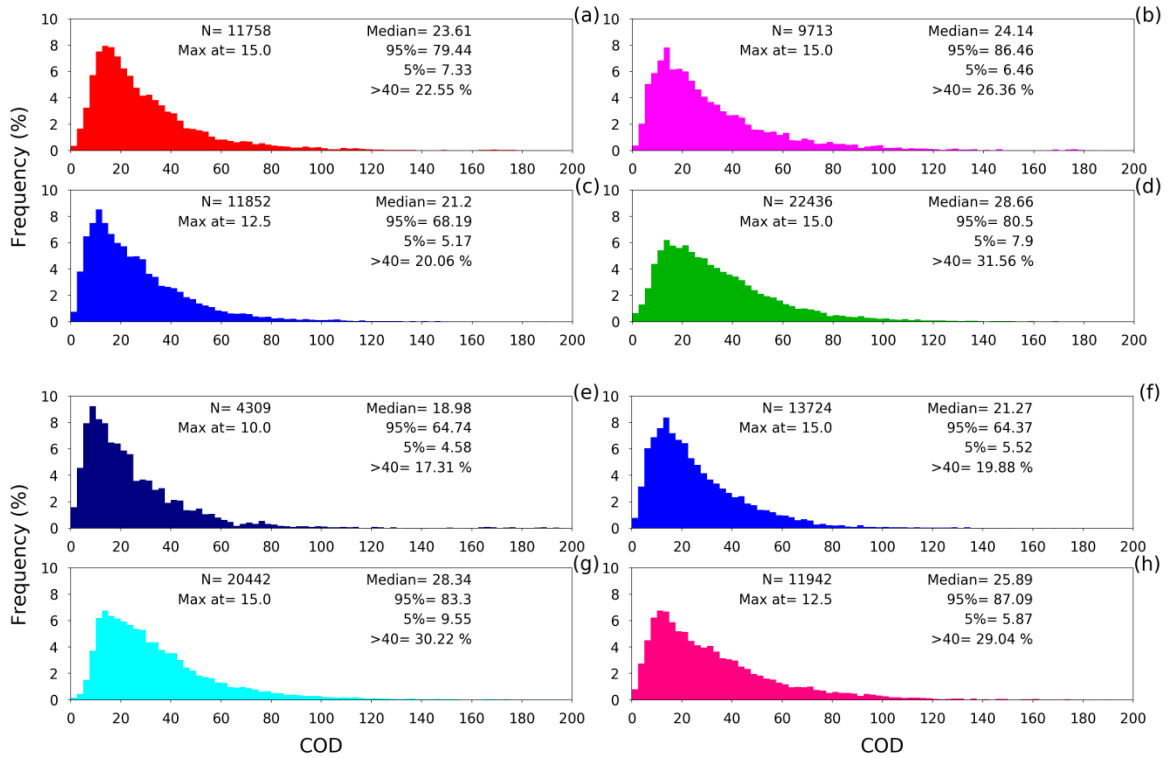

Figure 29. Seasonal and hourly COD distribution for low clouds. For summer (a), autumn (b), winter(c), spring (d). From sunrise up to 08:00 LT (e), between 08:00 and 10:00 LT (f), around noon (from 10:00 up to 14:00 LT) (g) and after 14:00 LT(h).
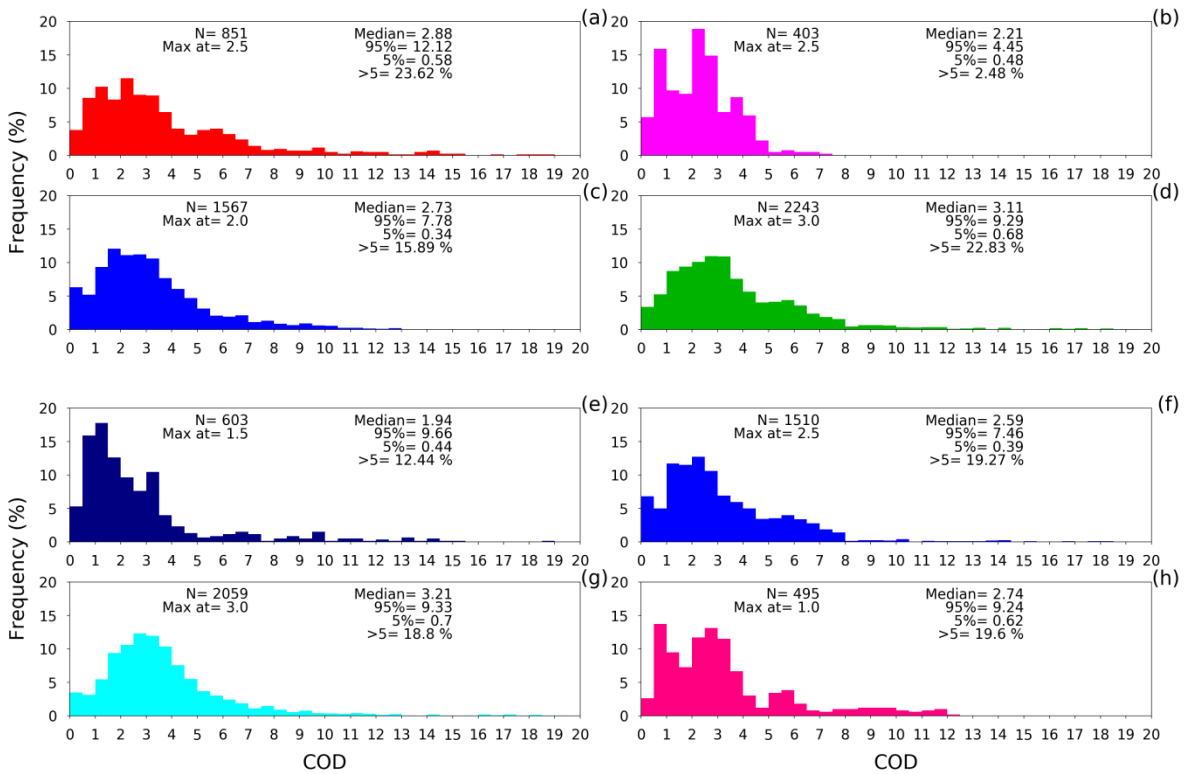

Figure 30. As Figure 28 but for cirrus clouds.

4.5. Cloud effects on solar radiation

4.5.1. Shortwave cloud radiative effects

The cloud effects on solar radiation (*CRE* and *NCRE*) are shown in the figure 31 for different cloud scenarios defined in the table 3. Considering that the model generally overestimated the global irradiance, *enhancement* effects were underestimated. The criterion applied to define enhancement was based on a threshold computed from relative error of the model to compute clear sky G (section 3.5.4). Also, cloud effects were classified depending on the solar disk, i.e. if it was clear or blocked by clouds (defined by 1 and 0, respectively).

When the solar disk was clear, *enhancement* effects were observed for the three cloud types analyzed, with the highest effect for low clouds with median of CRE (NCRE) of 79 W/m^2 (0.10). High clouds had the least enhancement effect with median of CRE (NCRE) of 49.8 W/m^2 (0.08). It is important to note that enhancement effect for mid clouds was comparable to lower clouds with CRE (NCRE) of 75.2 W/m^2 (0.12), but only 32 cases were found.

Extreme *enhancement* cases for CRE (NCRE) were found for low clouds reaching near 200 W/m^2 (0.3). The extremes of CRE were produced in isolated cases with 75 % observed between January and March with maximum in March with 30 % of cases. They were most prevalent (77 % of cases) between CSZA values of 0.85 and 1.

NCRE was less dependent on CSZA and NCRE cases above 0.3 were found throughout the year, with the higher number of cases in May (35 % of total of extreme cases). Near CSZA 0.3, the majority of cases were observed, with 28 % of total of cases. As Marín et al. (2017) reported, the enhancement effect does not depend on CSZA and the maximum of cases were observed between 40-50 % of cloud cover. They reported a median of NCRE of 0.18 and percentile 75 of 0.3.

An opposite cloud effect (shortwave radiation attenuation) was observed when clouds obstructed the solar disk. The maximum deficit was found for low

clouds in total overcast condition, with median for CRE (NCRE) of -400 W/m^2 (-0.72) and maximum of -880 W/m^2 (-0.99). For low clouds with no total overcast condition (LWBK_0), a less negative effect was found for NCRE, with median of -0.68. For low clouds, specially cases of broken clouds, an increase of diffuse irradiance is expected due to 3D effects related to conditions of low broken clouds (Tzoumanikas et al., 2016).
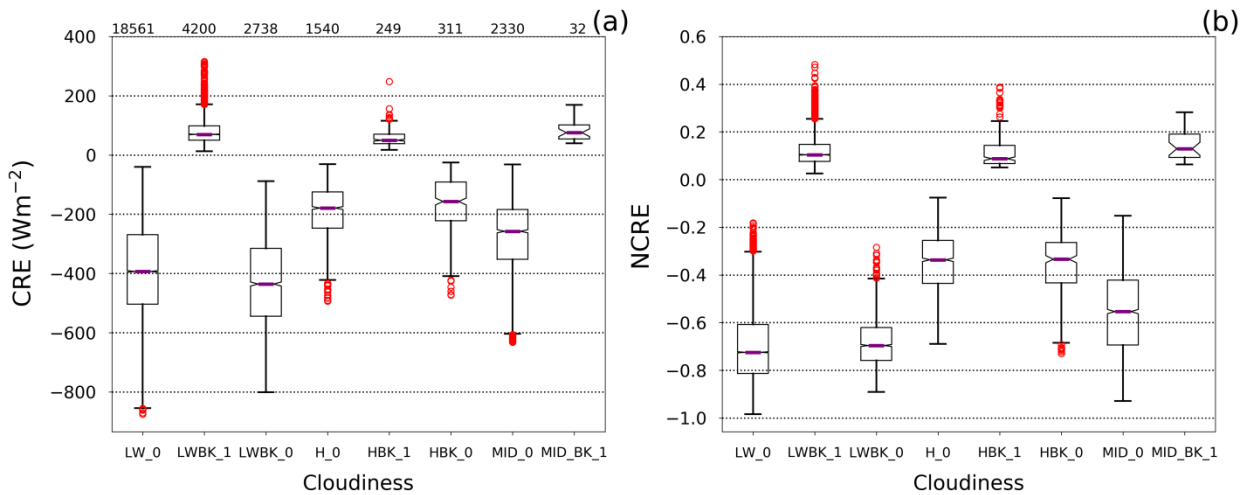
Figure 31: Cloud effects computed for cloudiness conditions and solar disk. Subscript 0 indicate obstructed solar disk and 1 not obstructed by clouds. Cloudiness are LW=low clouds, LWBK=low broken clouds, H=High clouds with total overcast, HBK=High broken clouds, MID=mid-level clouds with total overcast, MID_BK =mid-level broken clouds.

Mid-level clouds with total overcast had less attenuation effects compared to low clouds but the maximum could reach similar values. The median for mid clouds, for CRE and NCRE, were -240 W/m^2 and -0.57, respectively. High clouds, as expected, had the lowest cooling effects with median -190 W/m^2 and -0.33 for CRE and NCRE, respectively. Note, extremes of cooling effects of high clouds with NCRE (CRE) around -0.7 (-450 W/m^2) comparable to median of low clouds (LW_0).

Four cases of days under low broken clouds (Figure 32.b, d), total overcast of low clouds (Figure 32 c) and clear sky (Figure 32 a) conditions were selected from visual inspection of sky camera pictures. G measured by pyranometer, G modeled under clear sky, upper threshold of G modeled (in Figure 32 a,b,d) and lower threshold of G modeled (in Figure 32 c) due to error of model (section 4.3.3) and broadband SS from MFRSR are shown. SS from

MFRSR was employed to visually discriminate when the sun was totally blocked or not by clouds.

For clear sky conditions, SSA_{440} mean value of 0.85 retrieved on the same day by sun-photometer was employed. The good response of the model and the systematic overestimation relative to measurements can be observed. The mean relative error observed is around 5 % with a maximum of 12 % observed for the lower G values near 16:00 LT.

Due to this overestimation, the instants with enhancement effects might be slightly underestimated. For the case of total overcast condition (Figure 32.c), G measured by the pyranometer is clearly below the lower limit of the modeled G for clear sky condition minus one standard deviation.

The behavior observed for low broken clouds in Figure 32.b and Figure 30 d shows peaks of enhancement of G lasting, at maximum, about 20 minutes (Figure 32.d between 15:30-15:50). These cases of *enhancement* were observed when direct-sun was not blocked and they occurred at any time along the day.
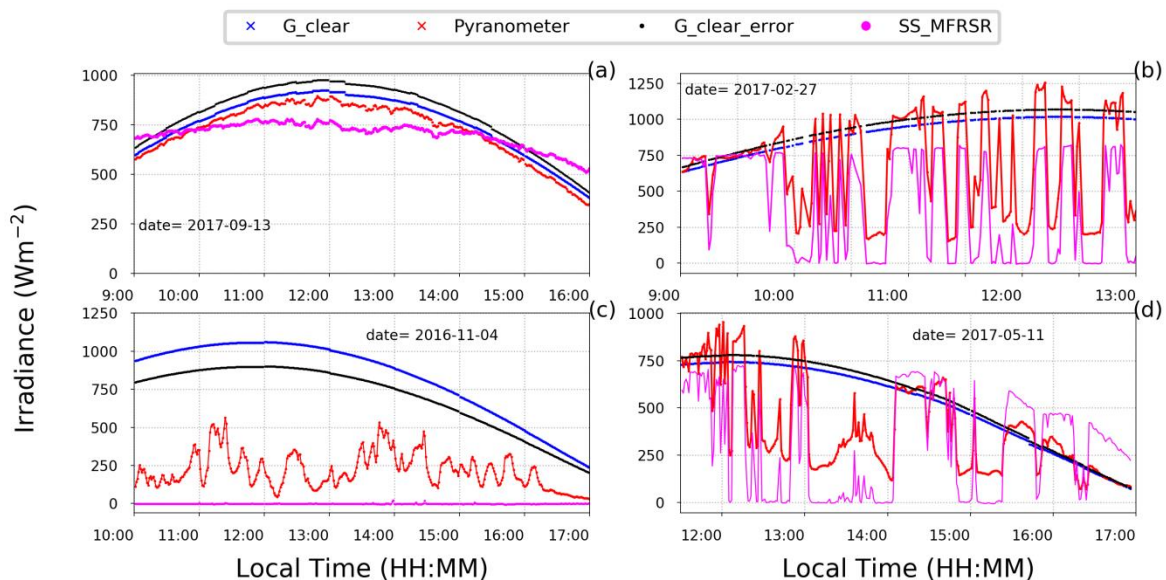

Figure 32: Specific day with clear sky conditions (a), low broken clouds (b,d) and total overcast (c).

4.5.2. Cloud efficiency

The dependence of the shortwave cloud radiative effect variables, CRE and NCRE, on COD and CSZA is presented in Figure 32 for liquid and ice clouds. The strong dependence of CRE on CSZA is observed, with lower CRE (higher negative effect or attenuation) for higher CSZA values.

The coefficient values (m =linear slope and R^2) of linear fit between CRE /NCRE and ln (COD) for CSZA centered at 0.32 to 0.97 with a range of ±0.025 were computed. One observes the good fit of CRE/NCRE with ln (COD), being less scattered as CSZA increases, especially for liquid clouds (Mateos et al., 2014). In addition, the slope became more negative for higher CSZA. A better accuracy was found when NCRE was used instead of CRE for liquid clouds. Furthermore, the NCRE vs ln (COD) was less dependent on CSZA (m less variable to changes on CSZA).

For ice clouds, the linear fit could be applied for lower COD (below 3), but with the increase of COD the relationship with ln (COD) was better observed. Therefore, to avoid discrepancies between ice and liquid clouds the same linear fit was applied, even though the relationship was not as robust as for liquid clouds. In addition, using NCRE for ice clouds the dependence with CSZA was not minimized.

The linear fit computed for liquid clouds was not as good as obtained by Mateos et al. (2014), because they computed COD from pyranometer measurements with less accuracy that the current work. But the relationship was still strong in this work, which allowed computing the radiative cloud efficiency from CRE. On the other hand, cloud efficiency could be computed from NCRE (Salgueiro et al., 2016) for liquid clouds with better accuracy. Due to the lower precision observed for ice clouds, CEF will be computed only for CSZA equal 0.85, in order to make a comparison with liquid clouds. CEF was computed using the slope of the linear fit for each CSZA interval (equation 30) and the correspondent value of COD. CEF computed from CRE (Figure 33 a) presented sensitivity to CSZA and COD. For any value of COD, the lower CSZA the lower CEF (in absolute units). Note the strong dependence on COD. For lower COD direct sun irradiance was not completely extinguished, and the

radiative effect included direct sun irradiance at the surface. But with the increase of COD, direct sun irradiance became less important until it was totally extinct (around COD 20). For higher COD, only the diffuse irradiance was observed at the surface. Because of that, the lower decrease of CEF for COD above 40 is observed.
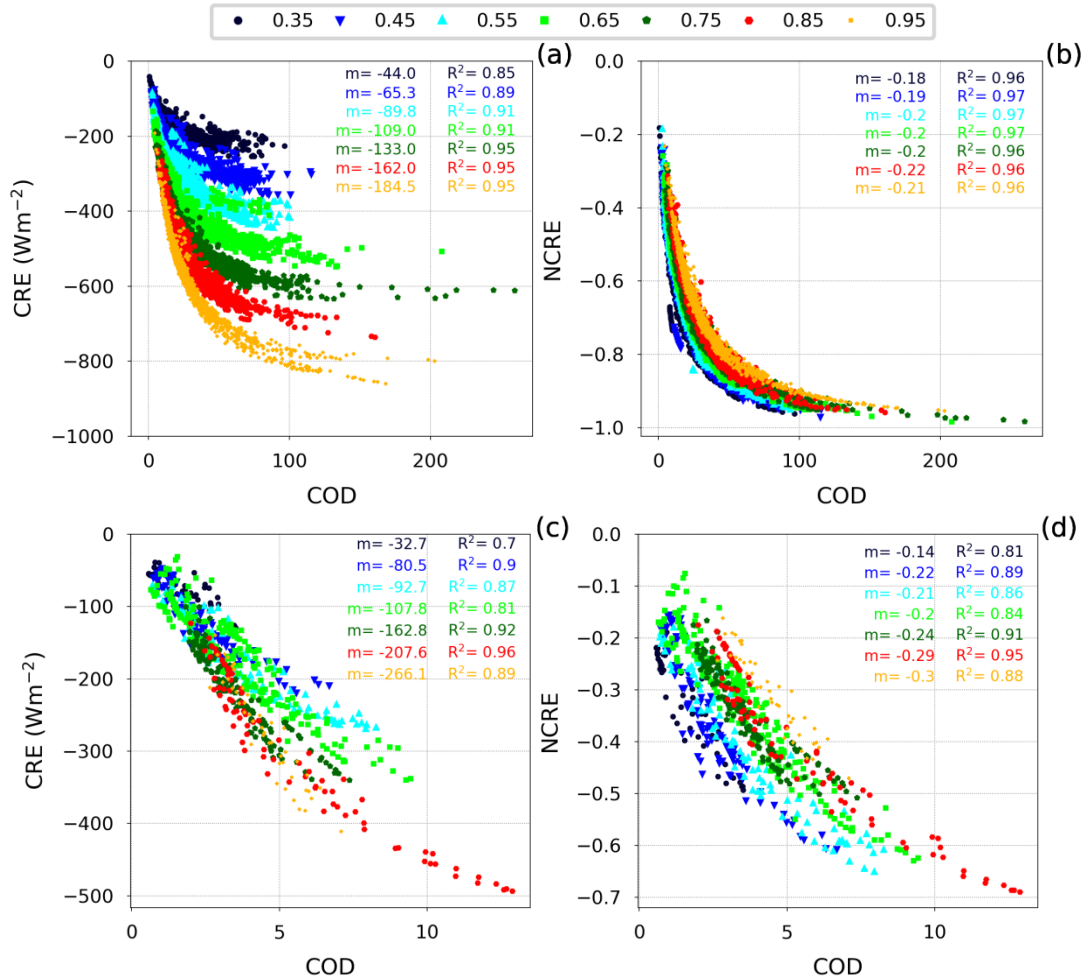
Figure 33. Relationship between CRE vs COD for liquid clouds (a) and ice clouds (c). Relationship between NCRE and COD for liquid clouds (b) and ice clouds (d). Colors are related to central values of CSZA. Value of m is the slope and R^2 the determination coefficient of the curve $Y = m \ln COD + n$.

Maximum of CEF computed from CRE was of -65 Wm^{-2} per COD-unit for values of CSZA near 0.35 and 0 COD, with the minimum CEF of almost 0 Wm^{-2} COD-unit^{-1} for the higher COD. For liquid clouds, the CEF computed from NCRE only depended on COD, the notable decrease observed until COD 40 is observed. After 40, it is almost invariable, with CEF near -0.01 COD unit^{-1}.

Differences can be observed between liquid and ice clouds for CEF computed from NCRE (Figure 33 c) in the COD interval between 0 and 12, for

CSZA around 0.85. Low clouds showed less efficiency as compared to ice clouds, with the maximum difference of 30 % around COD equal 2. Low clouds have higher values of asymmetry factor than ice clouds with 3D ice particle type (one example is Rough-aggregate used in the *uvspec* model) in the spectral range from 280 nm up to 1500 nm (see Figure 2). Thus, the forward scattering peak is stronger as compared to ice clouds.
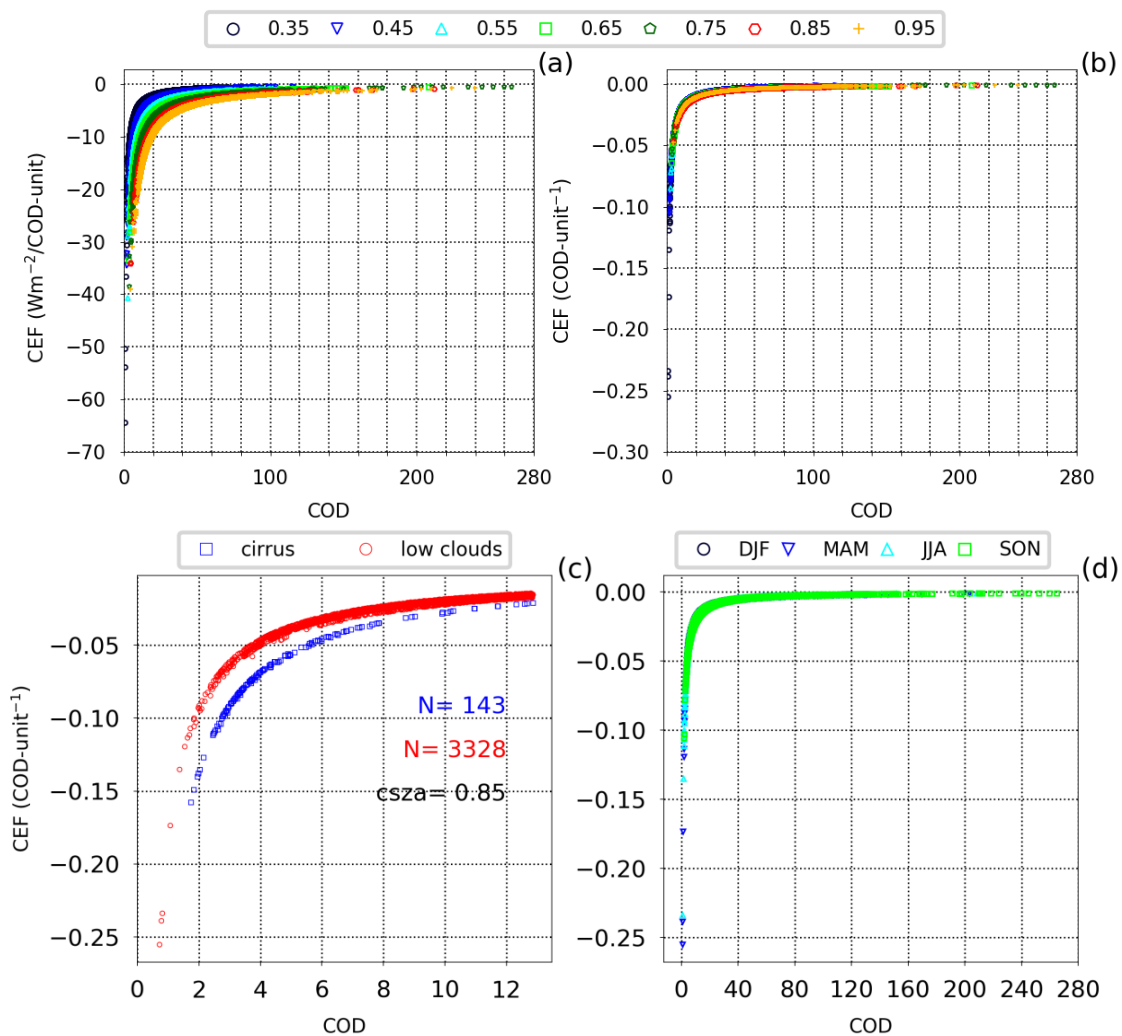
Figure 34. Cloud efficiency computed for CRE (a) and NCRE (b) for different CSZA values as function of COD for liquid clouds. Comparison between CEF (from NCRE) vs COD for liquid and ice clouds, for CSZA centered at 0.85 (c). Seasonal variation of CEF (from NCRE) for liquid clouds (d).

In addition, comparing the parametrization employed for retrieving COD for ice and low clouds around 415 nm, because there is no absorption of radiation by clouds (Figure 2), for the same T, lower COD is observed for ice clouds compared to low clouds. Moreover, ice clouds have higher absorption

efficiency in the spectral range between 1000 nm and 2000 nm, thus surface albedo can have a stronger impact on low clouds.

Those processes aforementioned can contribute to the lower efficiency of low clouds over ice clouds. There is no evidence of variation of CEF with respect to the season (Figure 33), but more detailed analysis is needed, for example the screening of cases with low aerosol loads versus polluted cases.

5. Conclusions

Variability of cloud profile at the region of MASP was observed by using a combined product from *CALIPSO-CloudSat*. Higher frequency was found in summer when clouds could reach 17 km, but, in winter, clouds could reach only 15 km. Differences between daytime and nighttime profiles were also detected. At daytime profile, the maximum frequency of around 30 % took place near 2500 m in summer. At night, only in winter the cloud frequency did not develop at higher layers. In addition, the increase of the height of clouds inland, as compared to the coast, was notable. Near the coast, clouds frequency had maximum around 2 km, and inland, as far as 100 km from the coast, the maxima were observed near 11 km altitude. The predominance of ice-3D cloud particle was found, especially for clouds above 10 km.

Cloud climatology for São Paulo, Brazil, for the period from 1958 to 2016 using hourly visual observations was performed. The diurnal cycle of cloud amount (cloud cover) was dominated by low clouds especially *stratiform* low clouds, with maximum at sunset and decreasing observed after sunrise until about 11:00 local standard time. Almost all cloud types showed an inverse diurnal cycle compared to the diurnal cycle of the solar heating, except low *cumuliform* clouds. Remarkable differences between *cumuliform* and *stratiform* clouds were also observed. The maximum presence of *Sc* in the afternoon, particularly in summer, can be related to complex dynamical mechanisms acting in the region. Its location near the coast where the sea breeze can interact with the heat island effect is an example, but further studies are necessary to a complete understanding of *Sc* formation and development in the region.

The diurnal cycle of clouds varied along the year. Larger differences were observed between April-August and the rest of the year. Between April and August the variation of the diurnal cycle amplitude was associated to the variation observed for stratiform clouds, whereas for summer-spring, the variation of the amplitude of cumuliform clouds, mid-level and high clouds was higher. The maximum cloud coverage was observed in the afternoon for summer-spring, but at sunrise in April-August for all cloud types. The annual

cycle showed the decrease of cloud amount of all cloud types in winter, our dry season, but maxima were variable and could be observed in spring or summer.

Seasonal and annual trends of cloud amount were computed considering the first 30 years, the last 30 and for the entire period (58 years). Significant trend for total cloud cover was only observed in autumn for the whole period (0.8 %/decade) and in the first 30 years (2.3 %/decade). Annual mean low cloud amount increased by 1.6 %/decade, due to the increase of 3.1 %/decade for stratiform low clouds, particularly in the first 30 years. Annual mean mid-level cloud amount decreased with a trend of -2.4 %/ decade. For the case of cirriform clouds, a statistically significant positive trend was observed only in autumn. In the annual basis, the trend was about 0.8 %/decade. For the entire period, the decrease of total cloud cover at sunrise (-0.5 %/ decade), and an increase of 0.8 %/ decade at midday were observed. Low cloud cover increased after midday (2.2 %/ decade), while cirriform clouds increased (0.8 %/ decade) only around midday. Mid-level clouds decreased in all the analyzed periods of the day.

Comparing with the global climatology, there was an agreement in trend for mid and high level clouds for the period of 1971-2009, but for low clouds, significant differences were observed, probably due to local effects influencing the characteristics of low stratiform clouds.

For retrieving COD and cloud effects for total overcast conditions, cloud scenarios were defined by the coincidence of three criteria: visual observation, the ratio of spectral diffuse irradiance between 870 nm and 415 nm channels and direct solar radiation blocked by clouds. Moreover, from September 2016, visual observations using the sky-camera were included.

The effective cloud optical depth (ECOD) was retrieved at the site using the total hemispheric transmittance at 415 nm estimated from the MFRSR. The method presented good accuracy for low clouds, with error below 15 % for COD above 20. But for ice clouds the error was higher, around 20 % for COD equal 20. For COD below 2, for both cloud types, errors were higher than 80 % associated to uncertainties in the optical properties of aerosols. Therefore the method was more efficient for low clouds. Consequently, methods for retrieving

COD with better estimation of aerosol single scattering albedo and using direct-sun measurements for lower COD can contribute to decreasing the error.

The values of ECOD presented seasonal variability, with the lowest for low clouds in winter with median of 21.2 and maximum in spring, equal 28.6. For cirrus clouds, the minimum was observed in autumn with median of 2.21 and maximum in spring with 3.11. In addition, for low clouds (cirrus) near sunrise the ECOD values were lower with median of 18.9 (1.94) as compared to the afternoon, with 28.3 (3.21). Values of ECOD for cirrus clouds could reach 10 in few cases.

Cloud effects on solar radiation at the surface were computed by the normalized shortwave cloud radiative effect (NCRE) and cloud radiative effect (CRE). Using the NCRE, the surface albedo was not taking into account and it was less sensitive to CSZA. Solar global irradiance at the surface under cloudy conditions was measured by a pyranometer and clear sky irradiance was computed by the RTM. Cloud radiative effects depended on the conditions of the solar disk, cloud type and cloud cover. When the solar disk was blocked by clouds, low cloud and total overcast conditions, NCRE presented a median value of -0.72, but when the sky was not totally overcast, the median was -0.68. For mid and high clouds the median of NCRE was -0.57 and -0.33, respectively. The *enhancement* effect was observed when the solar disk was clear for low (0.1), mid (0.12) and high clouds (0.07), with extreme values for low clouds (above 0.4). This *enhancement* effect could last up to 20 minutes.

The shortwave cloud efficiency (CEF) of low clouds was maximum for lower CSZA and COD. With higher values of COD no variation of CEF was observed with values near 0. The efficiency of low clouds was lower as compared to ice clouds. Differences up to 30 % for values of COD near 2 were estimated.

6. Future works

- Application of the method to retrieve COD of semitransparent clouds using direct sun transmittance (Min, 2004) is needed. The method could improve the accuracy of COD especially for lower values, and can contribute to better understand the radiative characteristics of cirrus clouds at the region.

- Effective radius (r_e) is one of the most important microphysical properties of clouds employed in the radiative transfer models. Variation of this parameter can lead to important variations of the impact of clouds in the radiation budget. Satellite derived products of r_e have limitations especially for low clouds. Specifically, under polluted conditions this variable can be affected particularly for low clouds. Therefore, continuous retrievals of this variable for the region are important.

- The use of 1-D RTM has some limitations when evaluating the cloud effects on the radiation budget e. g. cloud properties can only be retrieved under total overcast conditions or simple relationships with sky fraction for computing COD for partially overcast conditions. That is far from the actual configuration of cloud fields usually found. Therefore employing 3-D RTM in order to evaluate the 3D effects and, in synergy with sky camera, optical properties of clouds can be retrieved in partially overcast conditions, even when the sun disk is not blocked. Since computations using 3D RTM can be very costly, the development of parametrization of 3D for use in 1D-code can be an important step.

- Due to the subjective nature of visual observations of cloud cover, it would be important to test other long-term datasets of cloud cover from ground-based or satellites measurements with enough spatial resolution. Such measurements can be employed for comparison with results obtained from visual observations. One example is the method developed by Min et al. (2008), using ground-based measurements of MFRSR at spectral wavelengths centered at 870 nm and 415 nm.

7. References

Ackerman, S. A., and Stephens, G. L. (1987). The Absorption of Solar Radiation by Cloud Droplets: An Application of Anomalous Diffraction Theory. *Journal of the Atmospheric Sciences*, *44*(12), 1574–1588. https://doi.org/10.1175/1520-0469(1987)044<1574:TAOSRB>2.0.CO;2

Albrecht, B. A. (1989). Aerosols, Cloud Microphysics, and Fractional Cloudiness. *Science*, *245*(4923), 1227. https://doi.org/10.1126/science.245.4923.1227

Alizadeh-Choobari, O., and Gharaylou, M. (2017). Aerosol impacts on radiative and microphysical properties of clouds and precipitation formation. *Atmospheric Research*, *185*, 53–64. https://doi.org/10.1016/j.atmosres.2016.10.021

Almeida, M. P., Zilles, R., and Lorenzo, E. (2014). Extreme overirradiance events in São Paulo, Brazil. *Solar Energy*, *110*, 168–173. https://doi.org/10.1016/j.solener.2014.09.012

Anderson, G. P., Clough, S. A., Kneizys, F. X., Chetwynd, J. H., Shettle, E. P., U.S. Air Force Geophysics Laboratory., and Optical Physics Division. (1986). *AFGL atmospheric constituent profiles (0-120km)*.

Andrejczuk, M., Gadian, A., and Blyth, A. (2014). Numerical simulations of stratocumulus cloud response to aerosol perturbation. *Atmospheric Research*, *140–141*, 76–84. https://doi.org/10.1016/j.atmosres.2014.01.006

Austin, R. T. (2007). Level 2B radar-only cloud water content (2B-CWC-RO) process description document. *CloudSat Project Report*. Retrieved from ftp://ftp.cira.colostate.edu/ftp/CloudSat/Docs/2B-CWC-RO_PDICD.P_R04.20071021.pdf

Baldridge, A. M., Hook, S. J., Grove, C. I., and Rivera, G. (2009). The ASTER spectral library version 2.0. *Remote Sensing of Environment*, *113*(4), 711–715. https://doi.org/10.1016/j.rse.2008.11.007

Barnard, J. C., and Long, C. N. (2004). A simple empirical equation to calculate cloud optical thickness using shortwave broadband measurements. *Journal of Applied Meteorology*, *43*(7), 1057–1066.

Boersma, K. F., Eskes, H. J., and Brinksma, E. J. (2004). Error analysis for tropospheric NO$_2$ retrieval from space: ERROR ANALYSIS FOR TROPOSPHERIC NO$_2$. *Journal of Geophysical Research: Atmospheres*, *109*(D4), n/a-n/a. https://doi.org/10.1029/2003JD003962

Boucher, O., Randall, D., Artaxo, P., Bretherton, C., Feingold, G., Forster, P., Kerminen, V.-M., Kondo, Y., Liao, H., and Lohmann, U. (2013). Clouds and aerosols. In *Climate change 2013: the physical science basis. Contribution of Working Group I to the Fifth Assessment Report of the Intergovernmental Panel on Climate Change* (pp. 571–657). Cambridge University Press.

Brückner, M., Pospichal, B., Macke, A., and Wendisch, M. (2014). A new multispectral cloud retrieval method for ship-based solar transmissivity measurements. *Journal of Geophysical Research: Atmospheres*, *119*(19), 11,338-11,354. https://doi.org/10.1002/2014JD021775

Burleyson, C. D., Long, C. N., and Comstock, J. M. (2015). Quantifying Diurnal Cloud Radiative Effects by Cloud Type in the Tropical Western Pacific. *Journal of Applied Meteorology and Climatology*, *54*(6), 1297–1312. https://doi.org/10.1175/JAMC-D-14-0288.1

Carvalho, L. M., Jones, C., and Liebmann, B. (2004). The South Atlantic convergence zone: Intensity, form, persistence, and relationships with intraseasonal to interannual activity and extreme rainfall. *Journal of Climate*, *17*(1), 88–108.

Chiu, J. C., Huang, C.-H., Marshak, A., Slutsker, I., Giles, D. M., Holben, B. N., Knyazikhin, Y., and Wiscombe, W. J. (2010). Cloud optical depth retrievals from the Aerosol Robotic Network (AERONET) cloud mode observations. *Journal of Geophysical Research*, *115*(D14). https://doi.org/10.1029/2009JD013121

Christensen, M. W., Stephens, G. L., and Lebsock, M. D. (2013). Exposing biases in retrieved low cloud properties from CloudSat: A guide for evaluating observations and climate data. *Journal of Geophysical Research: Atmospheres*, *118*(21), 12,120-12,131. https://doi.org/10.1002/2013JD020224

da Silva, J. J., Lopes, F. J. S., and Landulfo, E. (2017). Cloud-Aerosols interactions by multiple scenarios approach. In A. Comerón, E. I. Kassianov, and K. Schäfer (Eds.) (p. 33). SPIE. https://doi.org/10.1117/12.2278588

de Almeida Castanho, A. D., Vanderlei Martins, J., and Artaxo, P. (2008). MODIS Aerosol Optical Depth Retrievals with high spatial resolution over an Urban Area using the Critical Reflectance. *Journal of Geophysical Research: Atmospheres*, *113*(D2), D02201. https://doi.org/10.1029/2007JD008751

de Miranda, R. M., Lopes, F., do Rosário, N. É., Yamasoe, M. A., Landulfo, E., and de Fatima Andrade, M. (2017). The relationship between aerosol particles chemical composition and optical properties to identify the biomass burning contribution to fine particles concentration: a case study for São Paulo city, Brazil. *Environmental Monitoring and Assessment*, *189*(1). https://doi.org/10.1007/s10661-016-5659-7

Dubovik, O., and King, M. D. (2000). A flexible inversion algorithm for retrieval of aerosol optical properties from Sun and sky radiance measurements. *Journal of Geophysical Research: Atmospheres*, *105*(D16), 20673–20696.

Dubovik, O., Smirnov A., Holben B. N., King M. D., Kaufman Y. J., Eck T. F., and Slutsker I. (2000). Accuracy assessments of aerosol optical properties retrieved from Aerosol Robotic Network (AERONET) Sun and sky radiance measurements. *Journal of Geophysical Research: Atmospheres*, *105*(D8), 9791–9806. https://doi.org/10.1029/2000JD900040

Eastman, R., and Warren, S. G. (2013). A 39-Yr Survey of Cloud Changes from Land Stations Worldwide 1971–2009: Long-Term Trends, Relation to Aerosols, and Expansion of the Tropical Belt. *Journal of Climate*, *26*(4), 1286–1303. https://doi.org/10.1175/JCLI-D-12-00280.1

Eastman, R., and Warren, S. G. (2014). Diurnal Cycles of Cumulus, Cumulonimbus, Stratus, Stratocumulus, and Fog from Surface

Observations over Land and Ocean. *Journal of Climate*, *27*(6), 2386–2404. https://doi.org/10.1175/JCLI-D-13-00352.1

Freitas, E. D. (2003). *Circulações Locales em São Paulo e sua influencia sobre disperção de poluentes* (Doctoral Thesis). University of São Paulo,Brazil.

Freitas, ED, Silva Dias, P., Carvalho, V., Rocha, C., Martins, L., Martins, J., and Andrade, M. (2009). Factors involved in the formation and development of severe weather conditions over the megacity of São Paulo. In 8th Symposium on the Urban Environment, Modeling and Forecasting in Urban Areas. Proceedings of the 89th AMS Annual Meeting.

Gasteiger, J., Emde, C., Mayer, B., Buras, R., Buehler, S. A., and Lemke, O. (2014). Representative wavelengths absorption parameterization applied to satellite channels and spectral bands. *Journal of Quantitative Spectroscopy and Radiative Transfer*, *148*, 99–115. https://doi.org/10.1016/j.jqsrt.2014.06.024

Guerrero-Rascado, J. L., Costa, M. J., Silva, A. M., and Olmo, F. J. (2013). Retrieval and variability analysis of optically thin cloud optical depths from a Cimel sun-photometer. *Atmospheric Research*, *127*, 210–220. https://doi.org/10.1016/j.atmosres.2012.10.025

Gueymard, C. A. (2004). The sun's total and spectral irradiance for solar energy applications and solar radiation models. *Solar Energy*, *76*(4), 423–453. https://doi.org/10.1016/j.solener.2003.08.039

Hagihara, Y., Okamoto, H., and Yoshida, R. (2010). Development of a combined CloudSat-CALIPSO cloud mask to show global cloud distribution. *Journal of Geophysical Research: Atmospheres*, *115*(D4), D00H33. https://doi.org/10.1029/2009JD012344

Hamed, K. H., and Rao, A. R. (1998). A modified Mann-Kendall trend test for autocorrelated data. *Journal of Hydrology*, *204*(1–4), 182–196.

Heymsfield, A. J., Krämer, M., Luebke, A., Brown, P., Cziczo, D. J., Franklin, C., Lawson, P., Lohmann, U., McFarquhar, G., Ulanowski, Z., and Van Tricht, K. (2017). Cirrus Clouds. *Meteorological Monographs*, *58*, 2.1-2.26. https://doi.org/10.1175/AMSMONOGRAPHS-D-16-0010.1

Holben, B. N., Eck, T. F., Slutsker, T. I., Tanre´, D., Buis, J. P., Setzer, K. A., Vermote, E., Reagan, J. A., Kaufman, Y. J., Nakajima, T., … Smirnov, A. (1998). *AERONET—A Federated Instrument Network and Data Archive for Aerosol Characterization*.

Holton, J. R., and Curry, J. A. (Eds.). (2003). *Encyclopedia of Atmospheric Sciences* (Edição: 1). Amsterdam ; Boston: Academic Press.

Houze, R. A., JR. (2014). *Cloud Dynamics: 104* (Edição: 2). Amsterdam ; New York: Academic Press.

Hu, Y. X., and Stamnes, K. (1993). An Accurate Parameterization of the Radiative Properties of Water Clouds Suitable for Use in Climate Models. *Journal of Climate*, *6*(4), 728–742. https://doi.org/10.1175/1520-0442(1993)006<0728:AAPOTR>2.0.CO;2

Hui, W. J., Cook, B. I., Ravi, S., Fuentes, J. D., and D'Odorico, P. (2008). Dust-rainfall feedbacks in the West African Sahel: DUST-RAINFALL FEEDBACKS. *Water Resources Research*, *44*(5). https://doi.org/10.1029/2008WR006885

Joiner, J., Vasilkov, A. P., Bhartia, P. K., Wind, G., Platnick, S., and Menzel, W. P. (2010). Detection of multi-layer and vertically-extended clouds using

A-train sensors. Retrieved from http://ntrs.nasa.gov/search.jsp?R=20110014293

Key, J. R., Yang, P., Baum, B. A., and Nasiri, S. L. (2002). Parameterization of shortwave ice cloud optical properties for various particle habits. *Journal of Geophysical Research: Atmospheres*, *107*(D13), AAC 7-1. https://doi.org/10.1029/2001JD000742

Kruskal, W. H., and Wallis, W. A. (1952). Use of Ranks in One-Criterion Variance Analysis. *Journal of the American Statistical Association*, *47*(260), 583–621. https://doi.org/10.2307/2280779

Kurucz, R. L. (1994). Synthetic Infrared Spectra (pp. 523–531). Dordrecht: Springer Netherlands.

Landulfo, E., Larroza, E. G., Lopes, F. J. S., and Hoareau, C. (2009). A preliminary classification of cirrus clouds over Sao Paulo city by systematic lidar observations and comparison with CALIPSO and AERONET data. In R. H. Picard, K. Schäfer, A. Comeron, and M. van Weele (Eds.) (p. 747506). https://doi.org/10.1117/12.829923

LeBlanc, S. E., Pilewskie, P., Schmidt, K. S., and Coddington, O. (2015). A spectral method for discriminating thermodynamic phase and retrieving cloud optical thickness and effective radius using transmitted solar radiance spectra. *Atmospheric Measurement Techniques*, *8*(3), 1361–1383. https://doi.org/10.5194/amt-8-1361-2015

Lee, H. (2016). Analysis of Carbon Dioxide and Cloud Effects on Temperature in Northeast China. *Procedia Computer Science*, *91*, 690–699. https://doi.org/10.1016/j.procs.2016.07.172

Leontyeva, E., and Stamnes, K. (1994). Estimations of Cloud Optical Thickness from Ground-Based Measurements of Incoming Solar Radiation in the Arctic. *Journal of Climate - J CLIMATE*, *7*(4), 566–578. https://doi.org/10.1175/1520-0442(1994)007<0566:EOCOTF>2.0.CO;2

Liou, K. N. (2002). *An Introduction to Atmospheric Radiation* (Edición: 2). Amsterdam ; Boston: Academic Press.

Mace, G. (2007). Level 2 GEOPROF product process description and interface control document algorithm version 5.3. *NASA Jet Propulsion Laboratory*.

Mahoney, W. P. (1988). Gust Front Characteristics and the Kinematics Associated with Interacting Thunderstorm Outflows. *Monthly Weather Review*, *116*(7), 1474–1492. https://doi.org/10.1175/1520-0493(1988)116<1474:GFCATK>2.0.CO;2

Manton, M. J. (1980). Computations of the effect of cloud properties on solar radiation. *Journal de Recherches Atmosphériques*, *14*, 1–16.

Marchand, R., Mace, G. G., Ackerman, T., and Stephens, G. (2008). Hydrometeor Detection Using Cloudsat—An Earth-Orbiting 94-GHz Cloud Radar. *Journal of Atmospheric and Oceanic Technology*, *25*(4), 519–533. https://doi.org/10.1175/2007JTECHA1006.1

Marín, M. J., Serrano, D., Utrillas, M. P., Núñez, M., and Martínez-Lozano, J. A. (2017). Effective cloud optical depth and enhancement effects for broken liquid water clouds in Valencia (Spain). *Atmospheric Research*, *195*, 1–8. https://doi.org/10.1016/j.atmosres.2017.05.008

Marshak, A., Knyazikhin, Y., Davis, A. B., Wiscombe, W. J., and Pilewskie, P. (2000). Cloud-vegetation interaction: Use of normalized difference cloud

index for estimation of cloud optical thickness. *Geophysical Research Letters*, *27*(12), 1695–1698.

Marshak, A., Knyazikhin, Y., Evans, K. D., and Wiscombe, W. J. (2004). The "RED versus NIR" plane to retrieve broken-cloud optical depth from ground-based measurements. *Journal of the Atmospheric Sciences*, *61*(15), 1911–1925.

Mateos, D., Antón, M., Valenzuela, A., Cazorla, A., Olmo, F. J., and Alados-Arboledas, L. (2013). Short-wave radiative forcing at the surface for cloudy systems at a midlatitude site. *Tellus B: Chemical and Physical Meteorology*, *65*(1), 21069. https://doi.org/10.3402/tellusb.v65i0.21069

Mateos, D., Antón, M., Valenzuela, A., Cazorla, A., Olmo, F. J., and Alados-Arboledas, L. (2014). Efficiency of clouds on shortwave radiation using experimental data. *Applied Energy*, *113*, 1216–1219. https://doi.org/10.1016/j.apenergy.2013.08.060

Mayer, B., Kylling, A., Emde, C., Hamann, U., and Buras, R. (2015). libRadtran user's guide. *Edition for LibRadtran Version*, *1*.

McBride, P. J., Schmidt, K. S., Pilewskie, P., Kittelman, A. S., and Wolfe, D. E. (2011). A spectral method for retrieving cloud optical thickness and effective radius from surface-based transmittance measurements. *Atmospheric Chemistry and Physics*, *11*(14), 7235–7252. https://doi.org/10.5194/acp-11-7235-2011

McPeters, R. D., Bhartia, P. K., Krueger, A. J., Herman, J. R., Wellemeyer, C. G., Seftor, C. J., Jaross, G., Torres, O., Moy, L., and Labow, G. (1998). Earth probe total ozone mapping spectrometer (TOMS): data products user's guide.

Min, Q. (2004). Retrievals of thin cloud optical depth from a multifilter rotating shadowband radiometer. *Journal of Geophysical Research*, *109*(D2). https://doi.org/10.1029/2003JD003964

Min, Q., and Harrison, L. C. (1996). Cloud properties derived from surface MFRSR measurements and comparison with GOES results at the ARM SGP Site. *Geophysical Research Letters*, *23*(13), 1641–1644. https://doi.org/10.1029/96GL01488

Min, Q., Wang, T., Long, C. N., and Duan, M. (2008). Estimating fractional sky cover from spectral measurements. *Journal of Geophysical Research: Atmospheres*, *113*(D20). https://doi.org/10.1029/2008JD010278

Morais, M. A., Castro, W. A. C., and Tundisi, josé G. (2010). Climatologia de frentes frias sobre a Região Metropolitana de São Paulo (RMSP), e sua influência na climatologia dos reservatórios de abastecimento de água. *Revista Brasileira de Meteorologia*, *25*(2), 205–217.

Moura, L. M. de, Martins, F. R., and Assireu, A. T. (2016). Clouds cover variability in São Paulo. *Revista Ambiente & Água*, *11*(4), 903–914.

Neiburger, M. (1949). Reflection, absorption, and transmission of insolation by stratus cloud. *Journal of Meteorology*, *6*(2), 98–104. https://doi.org/10.1175/1520-0469(1949)006<0098:RAATOI>2.0.CO;2

Norris, J. R., Allen, R. J., Evan, A. T., Zelinka, M. D., O'Dell, C. W., and Klein, S. A. (2016). Evidence for climate change in the satellite cloud record. *Nature*, *536*(7614), 72–75. https://doi.org/10.1038/nature18273

Obregón, G., Marengo, J., and Nobre, C. (2014). Rainfall and climate variability: long-term trends in the Metropolitan Area of São Paulo in the 20th

century. *Climate Research*, *61*(2), 93–107. https://doi.org/10.3354/cr01241

Okamoto, H., Sato, K., and Hagihara, Y. (2010). Global analysis of ice microphysics from CloudSat and CALIPSO: Incorporation of specular reflection in lidar signals. *Journal of Geophysical Research*, *115*(D22). https://doi.org/10.1029/2009JD013383

Paltridge, G. W. (1974). Infrared emissivity, short-wave albedo, and the microphysics of stratiform water clouds. *Journal of Geophysical Research*, *79*(27), 4053–4058. https://doi.org/10.1029/JC079i027p04053

Perlwitz, J., and Miller, R. L. (2010). Cloud cover increase with increasing aerosol absorptivity: A counterexample to the conventional semidirect aerosol effect. *Journal of Geophysical Research: Atmospheres*, *115*(D8). https://doi.org/10.1029/2009JD012637

Pincus, R., and Baker, M. B. (1994). Effect of precipitation on the albedo susceptibility of clouds in the marine boundary layer. *Nature*, *372*(6503), 250–252. https://doi.org/10.1038/372250a0

Rawlins, F., and Foot, J. S. (1989). Remotely Sensed Measurements of Stratocumulus Properties during FIRE Using the C130 Aircraft Multi-channel Radiometer. *Journal of the Atmospheric Sciences*, *47*(21), 2488–2504. https://doi.org/10.1175/1520-0469(1990)047<2488:RSMOSP>2.0.CO;2

Salgueiro, V., Costa, M. J., Silva, A. M., and Bortoli, D. (2016). Effects of clouds on the surface shortwave radiation at a rural inland mid-latitude site. *Atmospheric Research*, *178–179*, 95–101. https://doi.org/10.1016/j.atmosres.2016.03.020

Sayão, A. C. (2008). *Estudo da variabilidade zonal da profundidade optica do aerossol em São Paulo a partir de radiômetros MFRSR* (Dissertação de Mestrado). Universidade de São Paulo, São Paulo.

Serrano, D., Núñez, M., Utrillas, M. P., Marín, M. J., Marcos, C., and Martínez-Lozano, J. A. (2014). Effective cloud optical depth for overcast conditions determined with a UV radiometers: CLOUD OPTICAL DEPTH IN THE ERYTHEMAL BAND. *International Journal of Climatology*, *34*(15), 3939–3952. https://doi.org/10.1002/joc.3953

Silva Dias, M. A. F., Dias, J., Carvalho, L. M. V., Freitas, E. D., and Silva Dias, P. L. (2013). Changes in extreme daily rainfall for São Paulo, Brazil. *Climatic Change*, *116*(3–4), 705–722. https://doi.org/10.1007/s10584-012-0504-7

Sinyuk, A., Dubovik, O., Holben, B., Eck, T. F., Breon, F.-M., Martonchik, J., Kahn, R., Diner, D. J., Vermote, E. F., Roger, J.-C., … Slutsker, I. (2007). Simultaneous retrieval of aerosol and surface properties from a combination of AERONET and satellite data. *Remote Sensing of Environment*, *107*(1–2), 90–108. https://doi.org/10.1016/j.rse.2006.07.022

Stamnes, K., Tsay, S.-C., Wiscombe, W., and Jayaweera, K. (1988). Numerically stable algorithm for discrete-ordinate-method radiative transfer in multiple scattering and emitting layered media. *Applied Optics*, *27*(12), 2502–2509. https://doi.org/10.1364/AO.27.002502

Stephens, G. L. (2005). Cloud feedbacks in the climate system: A critical review. *Journal of Climate*, *18*(2), 237–273.

Stith, J. L., Dye, J. E., Bansemer, A., Heymsfield, A. J., Grainger, C. A., Petersen, W. A., and Cifelli, R. (2002). Microphysical observations of tropical clouds. *Journal of Applied Meteorology, 41*(2), 97–117.

Tian, L., and Curry, J. A. (1989). Cloud overlap statistics. *Journal of Geophysical Research: Atmospheres, 94*(D7), 9925–9935. https://doi.org/10.1029/JD094iD07p09925

Twomey, S. (1977). The Influence of Pollution on the Shortwave Albedo of Clouds. *Journal of the Atmospheric Sciences, 34*(7), 1149–1152. https://doi.org/10.1175/1520-0469(1977)034<1149:TIOPOT>2.0.CO;2

Tzoumanikas, P., Nikitidou, E., Bais, A. F., and Kazantzidis, A. (2016). The effect of clouds on surface solar irradiance, based on data from an all-sky imaging system. *Renewable Energy, 95*, 314–322. https://doi.org/10.1016/j.renene.2016.04.026

Vernier, J.-P., Thomason, L. W., Pommereau, J.-P., Bourassa, A., Pelon, J., Garnier, A., Hauchecorne, A., Blanot, L., Trepte, C., Degenstein, D., and Vargas, F. (2011). Major influence of tropical volcanic eruptions on the stratospheric aerosol layer during the last decade. *Geophysical Research Letters, 38*(12), L12807. https://doi.org/10.1029/2011GL047563

Warren, S. G., Eastman, R. M., and Hahn, C. J. (2007). A Survey of Changes in Cloud Cover and Cloud Types over Land from Surface Observations, 1971–96. *Journal of Climate, 20*(4), 717–738. https://doi.org/10.1175/JCLI4031.1

Warren, S. G., Hahn, C. J., and London, J. (1985). Simultaneous Occurrence of Different Cloud Types. *Journal of Climate and Applied Meteorology, 24*(7), 658–667. https://doi.org/10.1175/1520-0450(1985)024<0658:SOODCT>2.0.CO;2

Winker, D. M., Vaughan, M. A., Omar, A., Hu, Y., Powell, K. A., Liu, Z., Hunt, W. H., and Young, S. A. (2009). Overview of the CALIPSO Mission and CALIOP Data Processing Algorithms. *Journal of Atmospheric and Oceanic Technology, 26*(11), 2310–2323. https://doi.org/10.1175/2009JTECHA1281.1

Wood, R. (2012). Stratocumulus Clouds. *Monthly Weather Review, 140*(8), 2373–2423. https://doi.org/10.1175/MWR-D-11-00121.1

Yamasoe, M. A., and Corrêa, M. de P. (2016). *Processos Radiativos na Atmosfera. Fundamentos* (Edição: 1). Oficina de Textos.

Yamasoe, M. A., do Rosário, N. M. E., and Barros, K. M. (2017). Downward solar global irradiance at the surface in São Paulo city-The climatological effects of aerosol and clouds: SW Aerosol and Cloud Radiative Effect. *Journal of Geophysical Research: Atmospheres*. https://doi.org/10.1002/2016JD025585

Yang, P., Liou K. N., Wyser Klaus, and Mitchell David. (2000). Parameterization of the scattering and absorption properties of individual ice crystals. *Journal of Geophysical Research: Atmospheres, 105*(D4), 4699–4718. https://doi.org/10.1029/1999JD900755

Yau, M. K., and Rogers, R. R. (1989). *Short Course in Cloud Physics* (Edición: 3). Oxford: Butterworth-Heinemann.

Yoshida, R., Okamoto, H., Hagihara, Y., and Ishimoto, H. (2010). Global analysis of cloud phase and ice crystal orientation from Cloud-Aerosol Lidar and Infrared Pathfinder Satellite Observation (CALIPSO) data using

attenuated backscattering and depolarization ratio. *Journal of Geophysical Research*, *115*. https://doi.org/10.1029/2009JD012334